YIP 12) Thermal Mechanisms for Aerodynamic Flow Control

Jesse Little
ARIZONA UNIV BOARD OF REGENTS TUCSON

04/15/2016
Final Report

REPORT DOCUMENTATION PAGE

1. REPORT DATE *(DD-MM-YYYY)*	2. REPORT TYPE	3. DATES COVERED *(From - To)*
04/14/2016	FINAL PERFORMANCE REPORT	01 May 2012 - 30 Apr 2015

4. TITLE AND SUBTITLE	5a. CONTRACT NUMBER
(YIP 12)-Thermal Mechanisms for High Amplitude Aerodynamic Flow Control	
	5b. GRANT NUMBER
	FA9550-12-1-0044
	5c. PROGRAM ELEMENT NUMBER

6. AUTHOR(S)	5d. PROJECT NUMBER
Little, Jesse, C	
	5e. TASK NUMBER
	5f. WORK UNIT NUMBER

7. PERFORMING ORGANIZATION NAME(S) AND ADDRESS(ES)	8. PERFORMING ORGANIZATION REPORT NUMBER
UNIVERSITY OF ARIZONA 888 N EUCLID AVE TUCSON AZ 85719-4824	3000720

9. SPONSORING/MONITORING AGENCY NAME(S) AND ADDRESS(ES)	10. SPONSOR/MONITOR'S ACRONYM(S)
USAF, AFRL DUNS 143574726 AF OFFICE OF SCIENTIFIC RESEARCH 875 N. RANDOLPH ST. ROOM 3112 ARLINGTON VA 22203	
	11. SPONSOR/MONITOR'S REPORT NUMBER(S)

12. DISTRIBUTION/AVAILABILITY STATEMENT
Approved for public release; distribution is unlimited.

13. SUPPLEMENTARY NOTES

14. ABSTRACT
The potential of thermal perturbations (i.e. energy deposition) and subsequent compression wave generation as a mechanism for high amplitude, high bandwidth actuation has been demonstrated, but the fundamental physics of how this influences the flow field remain poorly understood. The aim of this study is to establish knowledge of the fundamental mechanisms underpinning the success of energy deposition for active flow control. The basic nature of this problem requires examination of a canonical flow system and turbulent shear layers are employed due to their ubiquitous nature in active flow control. The effects of localized thermal perturbations, delivered by electrical discharges and pulsed lasers, on these flows are studied experimentally with strong consideration of the rapidly developing literature and established theory. Our most important finding is that the required energy deposition is related to an as yet to be determined measure of the initial shear layer thickness. The initial shear layer state and freestream velocity are of secondary importance in the flow regimes surveyed. This suggests that amplitude scaling ideas for thermal perturbations are fundamentally different from those accepted for momentum-based devices. It also provides guidance for moving forward with such a definition.

15. SUBJECT TERMS
active flow control, energy deposition, plasma actuation

16. SECURITY CLASSIFICATION OF:			17. LIMITATION OF ABSTRACT	18. NUMBER OF PAGES	19a. NAME OF RESPONSIBLE PERSON
a. REPORT	b. ABSTRACT	c. THIS PAGE			
					19b. TELEPHONE NUMBER *(Include area code)*

INSTRUCTIONS FOR COMPLETING SF 298

1. REPORT DATE. Full publication date, including day, month, if available. Must cite at least the year and be Year 2000 compliant, e.g. 30-06-1998; xx-06-1998; xx-xx-1998.

2. REPORT TYPE. State the type of report, such as final, technical, interim, memorandum, master's thesis, progress, quarterly, research, special, group study, etc.

3. DATES COVERED. Indicate the time during which the work was performed and the report was written, e.g., Jun 1997 - Jun 1998; 1-10 Jun 1996; May - Nov 1998; Nov 1998.

4. TITLE. Enter title and subtitle with volume number and part number, if applicable. On classified documents, enter the title classification in parentheses.

5a. CONTRACT NUMBER. Enter all contract numbers as they appear in the report, e.g. F33615-86-C-5169.

5b. GRANT NUMBER. Enter all grant numbers as they appear in the report, e.g. AFOSR-82-1234.

5c. PROGRAM ELEMENT NUMBER. Enter all program element numbers as they appear in the report, e.g. 61101A.

5d. PROJECT NUMBER. Enter all project numbers as they appear in the report, e.g. 1F665702D1257; ILIR.

5e. TASK NUMBER. Enter all task numbers as they appear in the report, e.g. 05; RF0330201; T4112.

5f. WORK UNIT NUMBER. Enter all work unit numbers as they appear in the report, e.g. 001; AFAPL30480105.

6. AUTHOR(S). Enter name(s) of person(s) responsible for writing the report, performing the research, or credited with the content of the report. The form of entry is the last name, first name, middle initial, and additional qualifiers separated by commas, e.g. Smith, Richard, J, Jr.

7. PERFORMING ORGANIZATION NAME(S) AND ADDRESS(ES). Self-explanatory.

8. PERFORMING ORGANIZATION REPORT NUMBER. Enter all unique alphanumeric report numbers assigned by the performing organization, e.g. BRL-1234; AFWL-TR-85-4017-Vol-21-PT-2.

9. SPONSORING/MONITORING AGENCY NAME(S) AND ADDRESS(ES). Enter the name and address of the organization(s) financially responsible for and monitoring the work.

10. SPONSOR/MONITOR'S ACRONYM(S). Enter, if available, e.g. BRL, ARDEC, NADC.

11. SPONSOR/MONITOR'S REPORT NUMBER(S). Enter report number as assigned by the sponsoring/ monitoring agency, if available, e.g. BRL-TR-829; -215.

12. DISTRIBUTION/AVAILABILITY STATEMENT. Use agency-mandated availability statements to indicate the public availability or distribution limitations of the report. If additional limitations/ restrictions or special markings are indicated, follow agency authorization procedures, e.g. RD/FRD, PROPIN, ITAR, etc. Include copyright information.

13. SUPPLEMENTARY NOTES. Enter information not included elsewhere such as: prepared in cooperation with; translation of; report supersedes; old edition number, etc.

14. ABSTRACT. A brief (approximately 200 words) factual summary of the most significant information.

15. SUBJECT TERMS. Key words or phrases identifying major concepts in the report.

16. SECURITY CLASSIFICATION. Enter security classification in accordance with security classification regulations, e.g. U, C, S, etc. If this form contains classified information, stamp classification level on the top and bottom of this page.

17. LIMITATION OF ABSTRACT. This block must be completed to assign a distribution limitation to the abstract. Enter UU (Unclassified Unlimited) or SAR (Same as Report). An entry in this block is necessary if the abstract is to be limited.

Final Report

Thermal Mechanisms for High Amplitude Aerodynamic Flow Control (YIP 2012)

Jesse Little
Assistant Professor
Department of Aerospace and Mechanical Engineering
University of Arizona

April 2016

I. Abstract

The potential of thermal perturbations (i.e. energy deposition) and subsequent compression wave generation as a mechanism for high amplitude, high bandwidth actuation has been demonstrated, but the fundamental physics of how this influences the flow field remain poorly understood. There is a vital difference in the flow receptivity to these perturbations in comparison to more traditional zero net mass flux momentum-based devices. The aim of this study is to establish knowledge of the fundamental mechanisms underpinning the success of energy deposition for active flow control. This report summarizes efforts over a three year period under the AFOSR Young Investigator Program which seek to first study the phenomena at low speeds. The basic nature of this problem requires examination of a canonical flow system and turbulent shear layers are employed due to their ubiquitous nature in active flow control. The effects of localized thermal perturbations, delivered by electrical discharges and pulsed lasers, on these flows are studied experimentally with strong consideration of the rapidly developing literature and established theory. Our most important finding is that the required energy deposition is related to an as yet to be determined measure of the initial shear layer thickness. The initial shear layer state and freestream velocity are of secondary importance in the flow regimes surveyed. This suggests that amplitude scaling ideas for thermal perturbations are fundamentally different from those accepted for momentum-based devices. It also provides guidance for moving forward with such a definition. This definition has not yet been established, but is a primary focus of suggested future work. The thermal disturbances may be provided by single frequency forcing or alternatively using a collective heating from many pulses in burst operation. The response of the controlled flow can resemble an impulse-like behavior (high energy single frequency forcing) or a more standard convective nature (high frequency burst at lower pulse energies). These differing responses offer new avenues for exploration. In both cases, high levels of energy deposition can result in stabilization of the flow suggesting a competing mechanism is at play. Such a scenario has been observed in reacting flows with heat release, but has received no attention with respect to active flow control. In summary, the foundations of thermal mechanisms for active flow control have been established at low speeds. Future efforts now require progression to higher speeds flows with thinner turbulent shear layers.

II.   Table of Contents

III.   Introduction

Periodic excitation has been widely successful for controlling separation, jets and cavity tones among others (Greenblatt and Wygnanski 2000; Reynolds et al. 2003; Cattafesta et al. 2008). This is usually accomplished by adding slots or orifices near receptive regions of the flow field, namely those regions subject to sharp discontinuities or separation locations. Periodic excitation, in the form of momentum, is delivered through the slots to manipulate natural flow instabilities in an effort to prevent/reattach separated flows or modify/eliminate the formation of coherent structures. The excitation can be nonzero or zero net mass flux (ZNMF), where the latter has some practical advantages in that a source is not required. Generation of ZNMF excitation is accomplished through a variety of mechanisms, but often the use of piezoelectric, electromagnetic or electrostatic devices are employed. In all of these cases, an electromechanical driver creates the oscillatory flow. These devices are controlled through electrical signals and, compared to passive control technology; offer a significant reduction in weight, mechanical complexity and parasitic drag. Unfortunately, they possess limited bandwidth and may be subject to mechanical failure because the driver is operated at resonance to produce the high amplitude perturbations necessary for flow control in many practical applications. Even when operated in this fashion, amplitude requirements are often not met especially for high speed conditions.

The quest for high amplitude high bandwidth actuators has resulted in limited success as there are few devices capable of reliably controlling high speed ($U_\infty > 100$ m/s, $M > 0.3$) high Reynolds number flows ($Re > 1 \times 10^6$). The cause of this is appears rooted in the nature of ZNMF actuators which function through momentum addition. Complete amplitude scaling laws for such devices remain elusive, but the community is generally in agreement that it is at best proportional to U_∞ and at worst to U_∞^2 (Seifert and Tilmann 2009). A more appropriate parameter is the velocity external to the boundary layer (U_e), but U_∞ is often retained for simplicity. The majority of ZNMF actuators produce exit velocities below 100 m/s and most demonstrations have been limited to low speed laboratory scale flows. For example, airfoil separation control via ZNMF periodic excitation is well documented, but only occasionally at even takeoff and landing conditions of most transport aircraft, much less cruise. The search for a perfect actuator continues, but progress has been limited by the often proprietary nature these studies (Cattafesta and Sheplak 2011).

The use of energy deposition or "thermal" flow control appears more robust to high speed flows, but the fundamental mechanism behind this success remains poorly understood. It should be noted that usage of the term "thermal" is intended to simplify the terminology in this report. The compression wave produced by such actuation may play a role in some cases. Consequently, authors have also employed the term "thermoacoustic" for description. Thermal flow control can be accomplished through a variety of devices including focused Nd:YAG lasers and plasmas. Its original use for bulk heating via large volume diffuse plasma discharges required power on a similar scale as flow enthalpy while also suffering from glow to arc transition. Recent work has shown that localized pulsed heating may have substantial application at various flow speeds while also remaining viable from a power budget perspective. Most importantly, localized pulsed thermal disturbances have demonstrated control authority in both subsonic and supersonic flow regimes across applications such as jet mixing enhancement/noise mitigation, airfoil separation control and cavity flow structure modification (Lazar et al. 2008; Roupassov et al. 2009; Samimy et al. 2010; Little et al. 2012).

The aim of this work is to establish knowledge of the fundamental mechanisms underpinning the success of energy deposition or thermal actuation techniques for active flow control (AFC). Initially, and through discussion with AFOSR, our plan is to investigate the phenomena in low-speed flows with a natural progression to higher speeds in future efforts. The following section gives some sample results, but by no means exhaustive evidence of energy deposition for AFC. Subsequently, our progress in the examination of low speeds is described in the context of two canonical turbulent shear flows: mixing layer and backward-facing step.

IV.   Background and Motivation

A.   Active Flow Control

Unsteady (periodic or pulsed) excitation has been used with great success for controlling turbulent shear flows. Actuation technologies are generally based on mass, momentum and/or energy addition where momentum is by far the most common. ZNMF devices offer some advantages in that a source or sink is not required, but recent studies using non-ZNMF devices (discrete steady or sweeping jets) seem to hold promise even after consideration of source requirements (Whalen et al. 2015). Regardless, ZNMF devices remain desirable. Unsteady ZNMF excitation nearly always leverages the inviscid shear layer instability (Kelvin-Helmholtz) near the actuation location and this instability often couples with others downstream depending on the application (e.g. jet column, wake, separation bubble, etc.). Regardless of the "downstream" instabilities, the initial excitation of the Kelvin-Helmholtz instability is paramount to establishing the flow control process.

Consider the classical flow control problem of controlling separation over an airfoil near stall (Figure 1). In this case, the nominally separated flow (Figure 1a) is perturbed by a vibrating ribbon near the airfoil leading edge. This excites large spanwise vortices which entrain freestream momentum as they propagate over the chord (Figure 1b) thus reattaching flow in the mean. The appropriate frequency of this actuation has been related to maximizing the shear layer growth over the length of the separation or airfoil chord in this case (Greenblatt and Wygnanski 2000). This direct relationship between separation control (and many other types of AFC) and the initial excitation of the Kelvin-Helmholtz instability renders canonical turbulent shear layers excellent systems for quantifying the mechanisms associated with new actuation techniques.
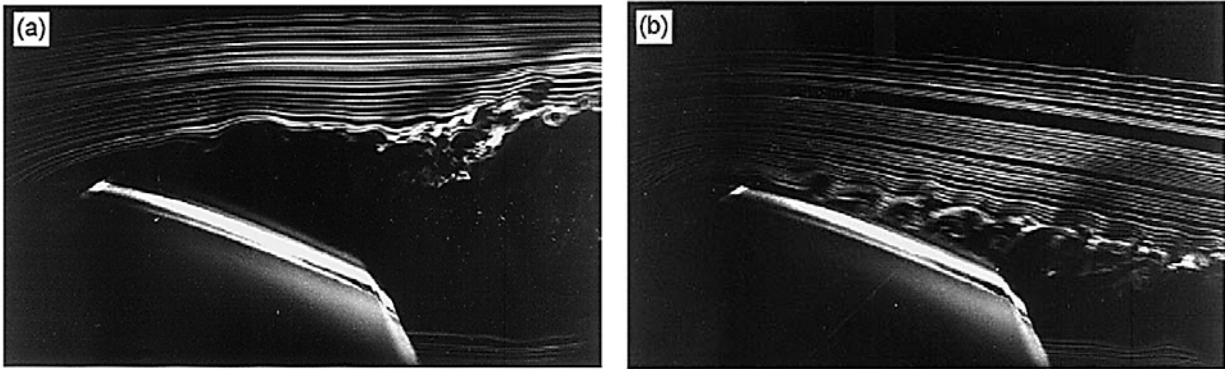

Figure 1: Smoke flow visualization over the top surface of a truncated NACA 0015 airfoil: baseline data (a), excitation by an oscillating ribbon near the leading edge at Re=40,000 (b) (Greenblatt and Wygnanski 2000).

As previously mentioned, ZNMF momentum-based devices are widely employed for AFC. The understanding of these actuation techniques has progressed over the years such that requirements for controlling a given flow are often known a priori. Figure 2a shows that the amplitude (cast as momentum coefficient, C_μ) required to control a given flow is minimized by the choice of an appropriate excitation frequency (F^+). Figure 2b suggests than some threshold value of C_μ is required to achieve said control objective at the appropriate frequency. In many systems, a reasonable requirement for C_μ and F^+ can be obtained, but this is not necessarily achievable especially in high speed flows. The challenge here lies in producing momentum based actuators with sufficient amplitude and bandwidth. As flow speeds increase the required actuation frequencies generally follow suit (e.g. $F^+ = fL/U_\infty$). Amplitude scaling is less established, but the community is generally in agreement that it is at best proportional to U_∞ and at worst to U_∞^2 (Seifert and Tilmann 2009). A more appropriate parameter is the velocity external to the boundary layer (U_e), but U_∞ is often retained for simplicity. The majority of ZNMF momentum-based actuators produce exit velocities below 100 m/s and operate in the range of a few kHz. Consequently, most demonstrations

5

have been limited to low speed laboratory scale flows save a few exceptions. Higher amplitude ZNMF momentum-based devices exist, but in many cases are not accessible to the general community because of proprietary status thus hindering the development of AFC. Regardless, the fundamental mechanism of ZNMF momentum-based actuation is a limiting factor in its adoption for high speed flows. Namely, with increasing flow speed comes increasing frequency and momentum requirements.
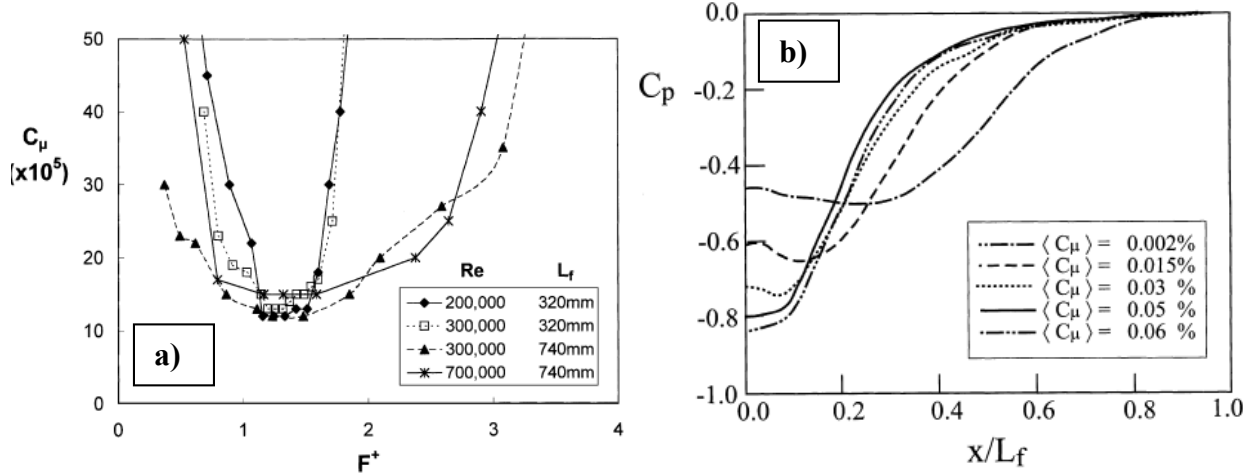

Figure 2: Minimum C_μ required to attach initially separated flow to a deflected flap as a function of F^+ for various conditions (a) and effect of excitation amplitude on the deflected flap bubble length at Re=450,000 and F^+=1.6 (b) (Greenblatt and Wygnanski 2000).

It is now apparent that the community must expand beyond momentum-based techniques for high-speed flow control to be a widespread possibility. Practical aspects aside, pulsed energy deposition (e.g. plasma or laser) appears to be a viable alternative. This actuation mechanism has demonstrated high amplitude and high bandwidth capability in a variety of turbulent shear flows. Samimy and co-authors have employed thermal mechanisms to control high speed, high Reynolds number jets (see Samimy et al. 2010 and references therein). In this case, localized arc filament plasma actuators (LAFPAs) are distributed around the nozzle exit. A single LAFPA consists of a pair of electrodes between which a high voltage is applied to generate a plasma discharge. The signature of this rapid localized heating is a compression wave shown in Figure 3a. Thermal excitation with LAFPAs has been used to excite a variety of instabilities in high speed, high Reynolds number, hot/cold, subsonic/supersonic jets. They remain the only high amplitude, high bandwidth device to do so. Figure 3b gives an example of the rich structure content excited by forcing a 1 inch Mach 1.3 jet with LAFPAs.
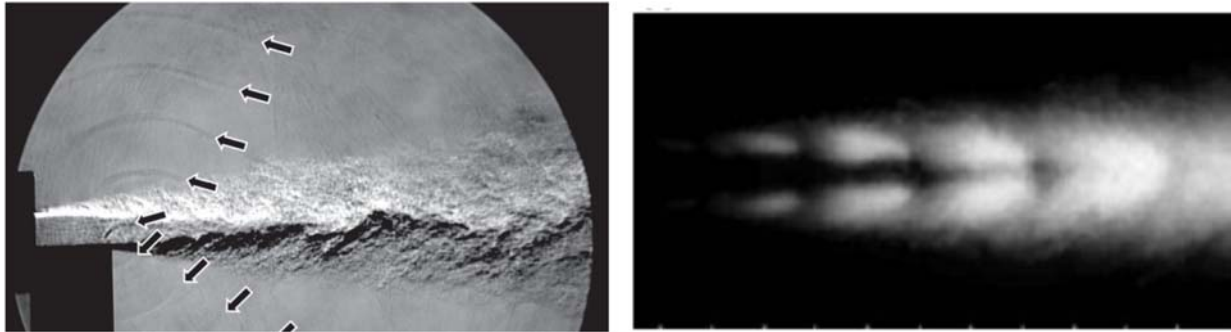

Figure 3: Instantaneous schlieren image of a rectangular Mach 0.9 jet showing LAFPA generated compression waves indicated by arrows (a) (Samimy et al. 2010) and phase-averaged flow visualization of LAFPA generated structures in a 1 inch Mach 1.3 jet (b) (Samimy et al. 2007).

6

Localized thermal perturbations via laser energy deposition have also been employed for flow control. Elliott and co-authors used a pulsed Nd:YAG laser to excite instabilities in supersonic jets and cavities (Adelgren et al. 2005; Lazar et al. 2008). In this case, the beam is focused to a spanwise line along the cavity leading edge (or point in the case of the jet). Similar to LAFPAs, the local heating of the focused beam generates a compression wave that is visible with standard schlieren techniques. This energy deposition excites flow instabilities thus modifying the structure of the shear layer formed between the freestream and low speed region. An example is shown Figure 4a where both the compression wave and large scale structure are visible. The phase-averaged transverse velocity component in Figure 4b demonstrates the propagation of laser induced structures along the cavity shear layer. While the high amplitude criterion is satisfied, the necessary bandwidth remains elusive due to limitations on laser repetition rate. As such, the behavior shown here is an impulse response and this may open new avenues for research. It should be noted that the excitation of similar instabilities has been consistently observed in subsonic flows using spanwise ZNMF actuation that relies on momentum production (Cattafesta et al. 2008). Numerous works on control of cavity tones have been produced using such devices yet they suffer from amplitude and bandwidth limitations as outlined previously.
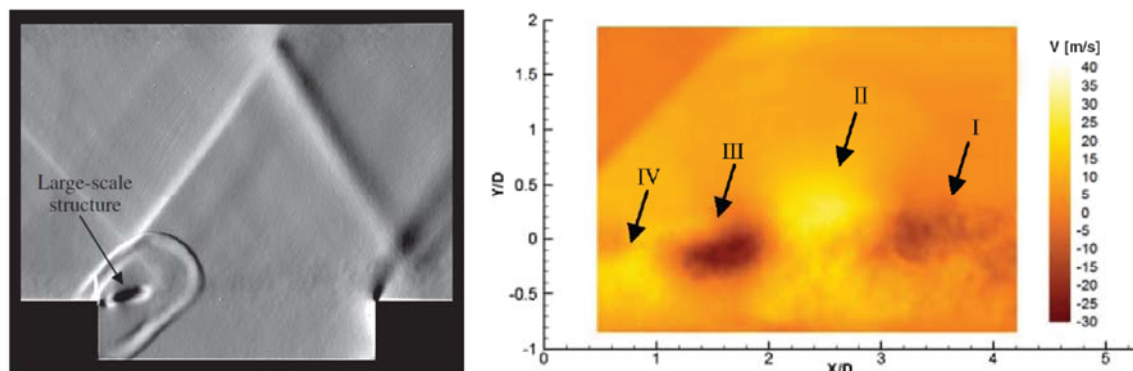

Figure 4: Schlieren images (a) and wall normal velocity fluctuations (b) of a supersonic cavity shear layer using pulsed laser energy deposition (Lazar et al. 2008).

Boundary layer separation control has also been demonstrated with thermal perturbations (Roupassov et al. 2009; Little et al. 2012). In this case, a dielectric barrier discharge (DBD) is employed on an airfoil leading edge. Application of short duration high voltage pulses (Figure 5a) to the DBD load generates rapid heating of the near surface gas giving rise to compression waves that bear some resemblance to those previously discussed in LAFPAs (Figure 5b). It is essential to note that this device is fundamentally different from the widely studied ac-DBD plasma actuator which functions through momentum transfer between ionized and neutral species (Corke et al. 2010) thus limiting control authority at high speeds very much like the ZNMF actuators previously discussed.
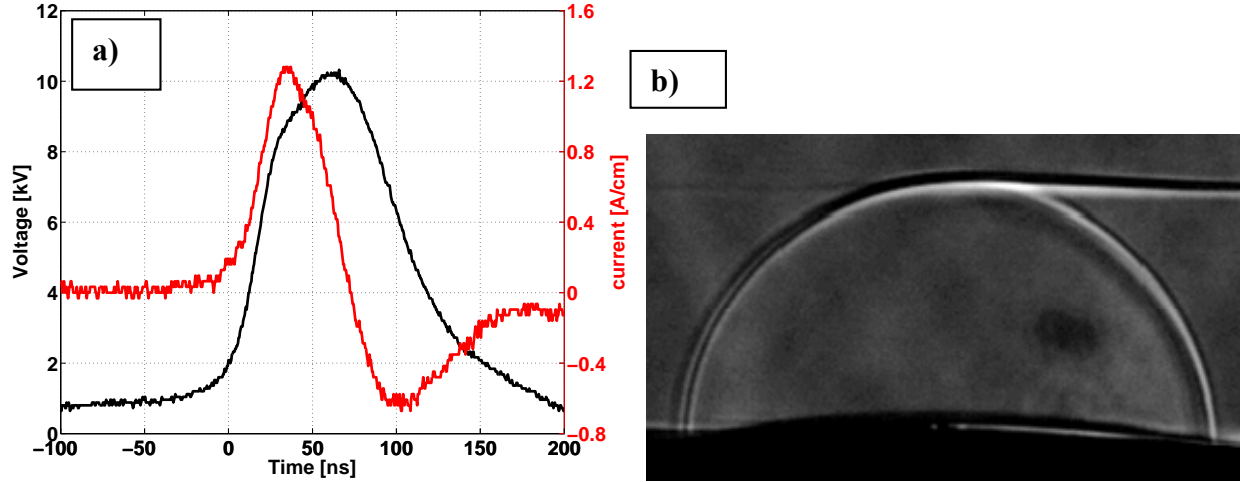
7

Figure 5: Sample voltage and current waveforms (a) and discharge induced compression wave (b) for an ns-DBD.

Spanwise forcing from an ns-DBD plasma actuator along an airfoil leading edge in stall produces large coherent vortices that reattach the nominally separated flow (Figure 6). The flow response is not unlike that shown in Figure 1, but in this case the control mechanism stems from rapid localized heating. It is also important to note that these structures can be identified for a wide range of frequencies at $0.25 \times 10^6 < Re < 1.15 \times 10^6$ corresponding to $0.05 < M < 0.25$, a limitation imposed only by the wind tunnel employed. Examples of successful ns-DBD flow control demonstrations and robust large scale structures (which are not necessarily optimal for control) can be found for various airfoils in the literature (Rethmel et al. 2011; Little et al. 2012; Ashcraft et al. 2016). The dynamic content confirms that separation control in this application is not due to laminar to turbulent transition at the airfoil leading edge, however this has been observed at lower incidence (Little et al. 2012). Some ns-DBD control authority using has been demonstrated to Mach 0.85 by Starikovskii and co-authors (Roupassov et al. 2009).
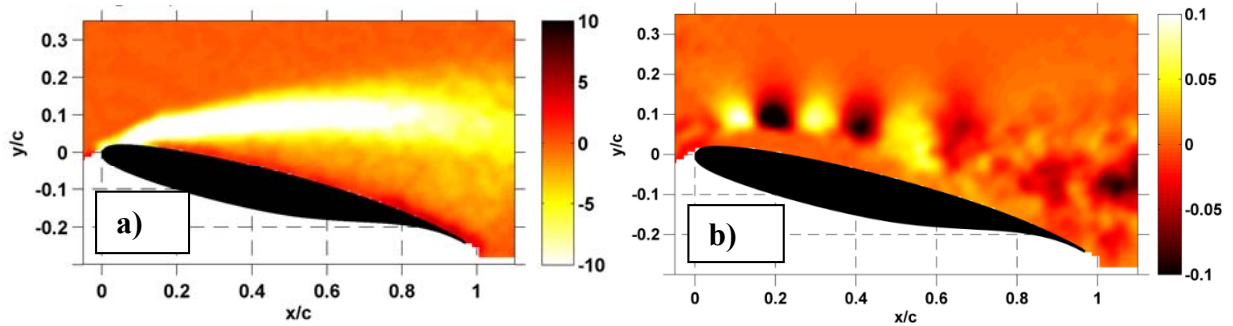

Figure 6: Baseline vorticity (a) and phase-averaged normal velocity fluctuations for spanwise ns-DBD plasma forcing along an airfoil leading edge at *Re*=750,000 (b) (Little et al. 2012).

Modeling and simulation efforts have complemented some of the experimental evidence discussed. Detailed information on the structure and evolution of an ideally expanded Mach 1.3 jet excited by LAFPAs has been revealed by modeling the discharge as pulsed surface heating (Gaitonde and Samimy 2011; Gaitonde 2012). Laser energy deposition in cavity flows has been modeled using a spherically symmetric Gaussian temperature distribution with total energy of 1 mJ (Aradag et al. 2004). The behavior of ns-DBD plasmas in quiescent air has modeled by simultaneous use of an electrohydrodynamic force in the momentum equation and a power density term due to heating in the energy equation (Unfer and Boeuf 2009). Additional studies on ns-DBDs for boundary layer separation control (airfoil leading edge) have

8

been performed with LES (Gaitonde et al. 2013). All of these efforts showed good agreement with experimental results, but none have determined the basic physics behind the thermal mechanism for AFC.

The potential of thermal perturbations (energy deposition) as a mechanism for high amplitude, high bandwidth actuation has been demonstrated, but the fundamental physics of how this process affects the flow field remains poorly understood. There is a vital difference in the flow receptivity to these perturbations in comparison to more traditional momentum-based ZNMF actuation. The report summarizes the findings of a three year research effort that directly addresses the fundamental aspects of this problem under the AFOSR Young Investigator Program. While jet mixing/noise, cavity tones and airfoil separation all have important applications of relevance to AFOSR directives, the basic nature of this problem requires examination of a more canonical system. Consequently, initial studies are performed on incompressible 2D turbulent shear layers, whose physics lay the basis for much of our understanding of flow control (Ho and Huerre 1984; Fiedler and Fernholz 1990; Greenblatt and Wygnanski 2000). This test bed also allows elimination or at least control of many of the complicating factors found in previously discussed applications such as pressure gradient, surface curvature, boundary layer state/thickness, separation location and velocity ratio. Some fundamental features of these canonical turbulent shear layers are provided below.

B. Turbulent Mixing Layers

Mixing layers occur in the velocity-gradient region between two streams. In practice, these streams are initially separated by means of a splitter plate. The size of the mixing layer, typically characterized by its momentum thickness, increases linearly downstream when not excited. The mixing layer is initially dominated by a linear instability mechanism and is highly susceptible to small perturbations (Michalke 1965; Ho and Huerre 1984; Greenblatt and Wygnanski 2000). The development of this knowledge led to explanations for large discrepancies in mixing layer growth rates between various experimental facilities (Oster and Wygnanski 1982). The momentum thickness of the excited mixing layer departs from the traditional linear growth and has historically been divided into three regions (Figure 7). The initial region (I) grows in a linear fashion due to amplification of quasi-two dimensional waves by the Kelvin-Helmholtz instability. At some location downstream (II) the growth of the mixing layer stops due to rollup of instability waves into discrete vortices before again resuming linear growth (III). The transition to region II is marked by a large reduction, or a sign change in the case of highly excited mixing layers, of the Reynolds shear stress and thus a decreased or negative turbulence production. The growth rate (I) and onset of neutral stability (II) are functions of the velocity ratio between the two streams, forcing frequency and forcing amplitude. Specifically, for a fixed frequency and velocity ratio, an increase in amplitude accelerates the growth process and moves the region of neutral stability closer to the mixing layer origin (Figure 8a). Similar behavior occurs when fixing the amplitude and velocity ratio while increasing the frequency (Figure 8b). For a general review of these regions of growth and their characteristics the reader is referred to the seminal papers of Oster and Wygnanski (1982), Weisbrot and Wygnanski (1988) and Greenblatt and Wygnanski (2000). The mixing layer growth rate is particularly sensitive to excitation frequency which scales with the momentum thickness. The most amplified frequency is found from linear stability theory and is expected near $St_\theta = f\theta/U_{avg} \approx 0.032$ where f is forcing frequency, θ is the local momentum thickness and U_{avg} is the average velocity of the two streams. However, the most amplified frequency shows some dependence on boundary layer state and initial conditions imposed by the experimental facility (Ho and Huerre 1984). Thorough reviews of excited shear flows have been published by Ho and Huerre (1984), Wygnanski and Petersen (1987) and Fiedler and Fernholz (1990). Note that in this work it is most appropriate to examine Region I and the onset of Region II since they are most applicable more general AFC scenarios.
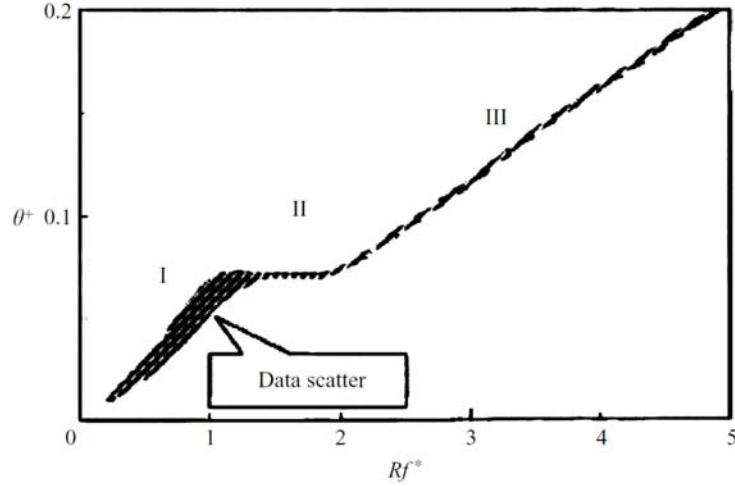
Figure 7: Dimensionless spreading rate of a mixing layer excited by periodic forcing (Wygnanski and Petersen 1987).
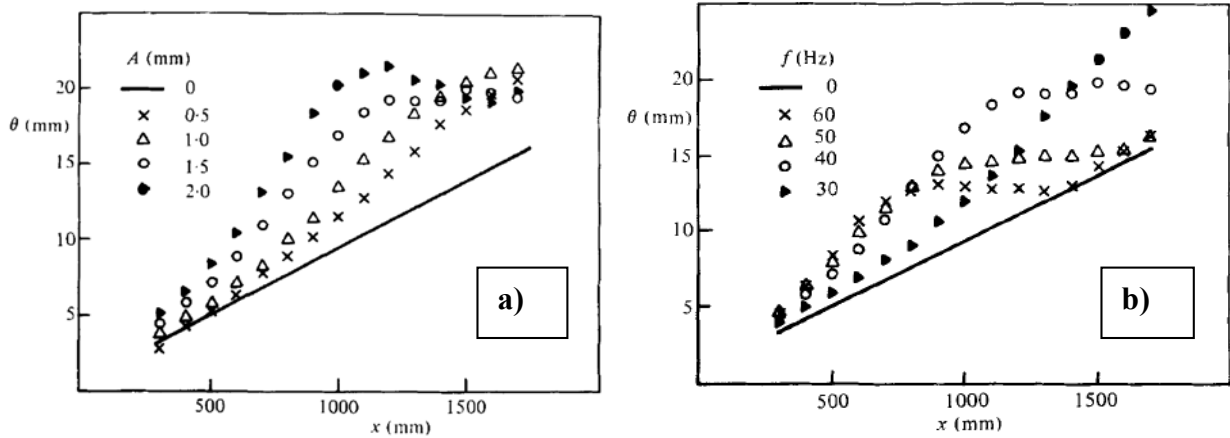

Figure 8: Effect of forcing amplitude (oscillating flap) on mixing layer momentum thickness at a fixed frequency (40 Hz) and velocity ratio (0.6) (a) and for variable frequency at a fixed amplitude (1.5 mm) and velocity ratio (0.6) (b). (Oster and Wygnanski 1982).

C. Backward-facing Step

Reattaching shear layers, such as those formed downstream of a backward-facing step (BFS), are initially governed by the same Kelvin-Helmholtz instability as mixing layers. However, the presence of and reattachment to the wall prevent the development of region II and III as described above. In the first half of the separated region, the behavior is most similar to the free shear layer with the important exception that the low-speed side is highly turbulent (Simpson 1989). The expected shear layer instability in BFS flows is near $St_{\theta o} \approx 0.012$ (Hasan 1992). As shear layer vortices convect downstream, their size increases and pairing occurs accompanied by a decrease in the characteristic frequency. The BFS flow eventually becomes locally absolutely unstable in the recirculating region due to a strong reverse flow and shear layer thickness of similar magnitude as the BFS height (Wee et al. 2004). This is in contrast to mixing layers which are locally convectively unstable throughout (Huerre and Monkewitz 1985). The reattachment behavior is strongly dependent on characteristics of the separating boundary layer (e.g. momentum thickness, state, ratio of thickness to step height, etc) (Eaton and Johnston 1981). Freestream turbulence, expansion ratio ((H+h)/h) and aspect ratio (W/H) are also influential. Various BFS AFC studies have been performed using all manner of actuators and control strategies (Hasan 1992; Chun and Sung 1996; Vukasinovic et al. 2010; Kapiris and

10

Mathioulakis 2014). Optimal forcing frequencies for reattachment are typically in the range of $St_H \approx 0.2$ and in many cases this is also very near the shear layer instability frequency ($St_{\theta o} \approx 0.012$) (Hasan 1992).
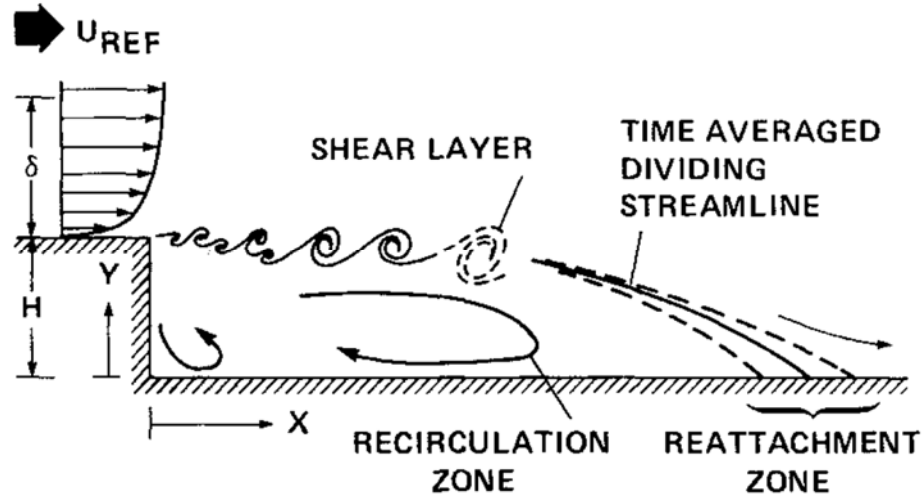

Figure 9: Main features of a backward-facing step flow (Driver et al. 1987).

In summary, turbulent shear layers provide an excellent test case for elucidating the fundamental mechanisms associated with flow control using thermal perturbations and their relatives. In particular, it allows the removal or control of many complicating factors such as surface curvature, pressure gradient, boundary layer state/thickness, etc. The established knowledge of these flows provides a standard for understanding novel actuation techniques. In the remaining sections of this report, a description of our experimental facilities is provided followed by a detailed summary of the results, their implications and requirements for future work.

V.   Experimental Facilities and Techniques

A. Mixing Layer Facility

The mixing layer facility consists of an open circuit suction wind tunnel with a 1ft x 1ft x 3ft closed test section. The test section is constructed of acrylic walls that are held together with an aluminum frame. A hinged door side wall allows for accessibility to the inside of the test section. In the hinged door and side wall directly opposite, 6in diameter circular plugs are installed to allow mounting of models and measurement devices. The top wall of the tunnel contains a static pressure tap at the contraction exit as well as multiple holes used to attach various probes. The wind tunnel inlet contraction ratio is 9:1 with a honeycomb and multiple screens for flow conditioning. The diffuser is 94in long with an equivalent conical angle of approximately 8 degrees. Maximum velocity in a clear test section is ~9m/s. A rubber connection is used between the fan and the diffuser to minimize vibration. A custom manufactured suction splitter plate is used to separate the two streams (Figure 10). The splitter plate is 1ft x 1ft with thickness of 0.375in and is constructed primarily of aluminum. The acrylic trailing edge of the splitter plate has a 2in long taper on the top and bottom surface of approximately 5 degrees. The taper on the top surface of the splitter plate trailing edge also contains a recess of 0.02in such that DBD actuators can be installed flush with the surface. The leading edge of the splitter plate employs a droop constructed of two pieces of sheet metal mounted to the bottom and top surface of the plate. A wooden dowel rod is used as a leading edge. The droop extends 3in upstream and 1.25in under the plate. The droop is required to eliminate boundary layer separation on the high speed side.
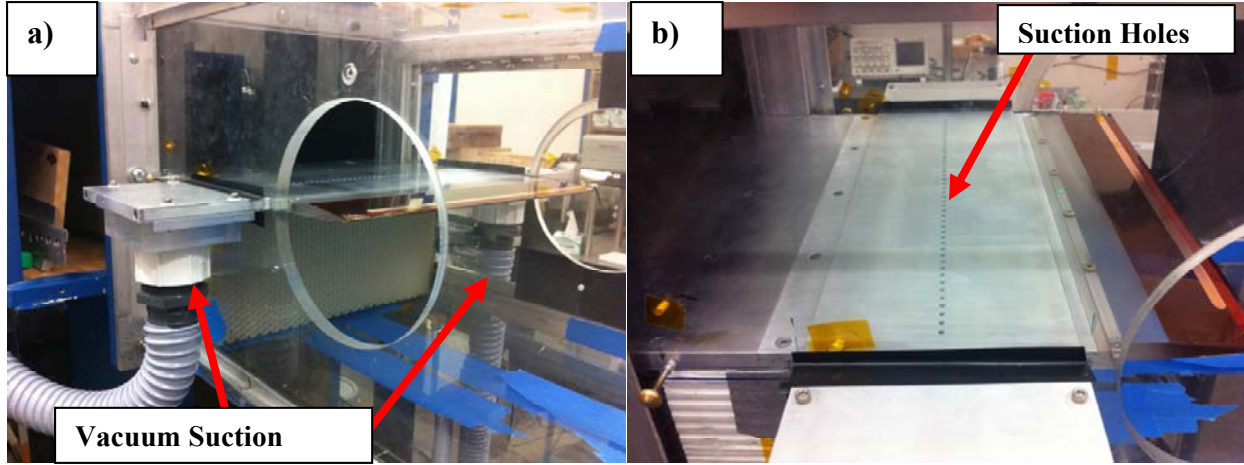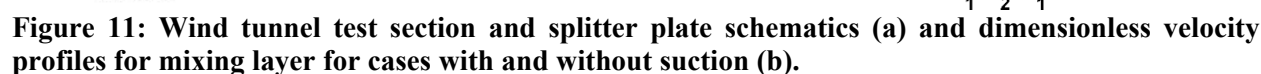
11

Figure 10: Wind tunnel test section and suction splitter plate (flow from left to right).

Downstream of the droop is a suction chamber, which is employed to reduce the boundary layer thickness on the top and/or bottom surface of the splitter plate. The suction chamber is constructed of a hollow aluminum housing with cross-sectional area of $0.9in^2$ and 45 suction holes at mirrored locations on the top and bottom surface. All suction holes are approximately 5.8in upstream of the trailing edge. The suction hole diameter is varied over the course of the experiments, but is initially 0.0625in on both the top and bottom surfaces. The suction chamber itself accounts for 4.6in of the overall streamwise length of the splitter plate, and extends 4in out of each sidewall of the test section through machined slots (Figure 10). Each end of the suction chamber outside of the test section contains a 1.5in diameter circular opening and aluminum adapter mounted to the bottom surface which is designed to accept a PVC fitting and vacuum hose. Two 3 Stage, 530W Lamb Ametek vacuum motors are used to apply suction to either side of the suction chamber. Various suction configurations are tested by blocking entirely and/or varying the size of suction holes, as well as employing only one of the two vacuum motors. Uniform suction characteristics were confirmed by measuring both boundary and mixing layer profiles downstream which showed collapse indicating 2D behavior.

The splitter plate is attached to the side wall of the tunnel using dowel pins and extends 1ft into the test section length. A 0.375in wide foam strip is used to maintain a seal between the high and low-speed side of the splitter plate where necessary. A head loss device in the form of a polyurethane filter and honeycomb is used to generate the velocity difference between the two streams. The filter has thickness of 0.25in and is cut to fill the space under the splitter plate. A screen is used for further velocity reduction and flow conditioning on the low-speed side of the splitter plate. Two flow configurations are examined. In high-speed tests, the velocity ratio is $r=U_1/U_2 \approx 0.28$ with high-speed side having $U_2 \approx 11.9m/s$. Reynolds number based on the initial momentum thickness is calculated as 1270. In the low-speed case, the velocity ratio is $r \approx 0.24$ with $U_2 \approx 6.1m/s$ and $Re_{\theta o} \approx 840$. A schematic of the facility as well as downstream mixing layer profiles are shown in Figure 11. The profiles include cases with and without boundary layer suction. The velocity profiles and normal coordinate have been non-dimensionalized in the traditional manner using the high (U_2) and low (U_1) speed streams, location of the average of the high and low speed streams, $y_{0.5}$, and the momentum thickness of the shear layer, θ, at each downstream location where:

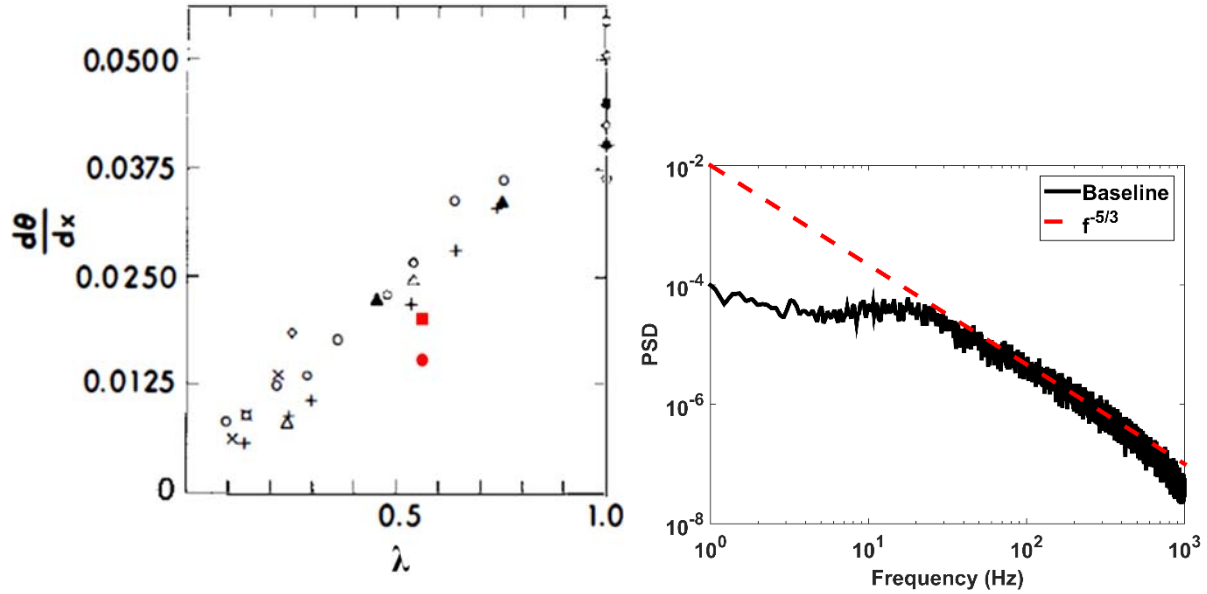$$\theta = \int_{-\infty}^{\infty} \frac{U - U_1}{U_2 - U_1}\left(1 - \frac{U - U_1}{U_2 - U_1}\right)dy$$

Figure 11: Wind tunnel test section and splitter plate schematics (a) and dimensionless velocity profiles for mixing layer for cases with and without suction (b).

The data collapse nicely in both cases using this definition ensuring that the baseline behavior of the mixing layer experiment (with and without suction) is obeying conventional wisdom. Some evidence of mean flow distortion due to the proximity of the head loss device can be seen on the low speed side. Further characterization of the baseline mixing layer behavior is provided in Figure 12. Figure 12a shows the momentum thickness growth rate compared to past literature. The boundary layer suction case is indicated by a square and without is shown a circle. The growth rate is somewhat smaller than given in the literature, but this is improved by suction. This suggests the mixing layer employed here may retain some developing characteristics, especially for cases without suction. It will later be shown that the Reynolds shear stress is not quite self-similar suggesting fully developed turbulence has not been reached (Birch and Eggers 1972). The shear stress behavior is also improved by suction in agreement with Figure 12a. A velocity spectrum at the center of the mixing layer (x=450mm) is shown in Figure 12b. The turbulent nature of the flow is clear since a well-developed inertial subrange exists over nearly 2 frequency decades. One also notes a broad peak in the range of 10-30Hz which will later be shown as a fruitful range for maximizing mixing layer growth in the test section. The boundary and mixing layer conditions generated by the various combinations of suction and velocity variation are detailed in Section VI.A.

Figure 12: a) Mixing layer spreading rate *dθ/dx* versus velocity parameter $\lambda = (U_2 - U_1)/(U_2 + U_1)$. Current facility with (square) and without (circle) boundary layer suction shown in red. Other points from past literature (Ho and Huerre 1984). b) Velocity spectrum in the center of the mixing layer at x=450mm.

B. Backward Facing Step Facility

A small blow-down wind tunnel was constructed for BFS experiments. The facility consists of an axial fan, honeycomb, multiple screens, and a settling length that terminates into a 13.8:1 rectangular nozzle contraction. The contraction curvature has been designed using a 5th order polynomial with zero first and second derivatives at the inlet/outlet as well as continuous first and second derivatives throughout (Brassard and Ferchichi 2005). The inlet radius is larger than the outlet radius to satisfy conventional wisdom (Mehta and Bradshaw 1979). The contours are CNC machined out of a sandwich construction of medium density fiber board. The wind tunnel produces a freestream velocity of approximately 30.5m/s with variation less than 0.25% in the inviscid region. The acrylic test section is initially 2in x 4in and a backward facing step (BFS) of height, H = 0.325in, is installed in the test section floor approximately 4in downstream of the nozzle exit. The BFS with DBD actuator installed is shown in Figure 13. The streamwise length of the test section is 36in and exhausts to atmosphere. A reattaching shear layer is formed due to separation of the natural test section boundary layer at the step. The expansion ratio of the step is 1.08 and the aspect ratio is 6.15:1. This satisfies general criteria for negligible pressure gradient, but does not satisfy criteria for negligible 3D effects (> 10:1 in horizontal) (Chandrsuda and Bradshaw 1981). The BFS height was chosen for convenience and also to facilitate ease of plasma actuator installation. Thus, a trade-off was required for horizontal aspect ratio and it is likely that the reattaching shear layer exhibits 3D effects near the tunnel sidewalls. However, all measurements are acquired on the tunnel centerline with primary focus given to the evolution of the mixing layer near the step corner which should approximate 2D conditions. The boundary layer separating from the step has thickness, $\delta \approx 1.3$mm, momentum thickness $\theta_0 \approx 0.15$mm and shape factor of approximately 1.9. The Reynolds number based on step height, Re_H, is approximately 17,000 and Re_{θ_o} is approximately 300. Additional details of the incoming boundary layer are provided in Section VI.B.
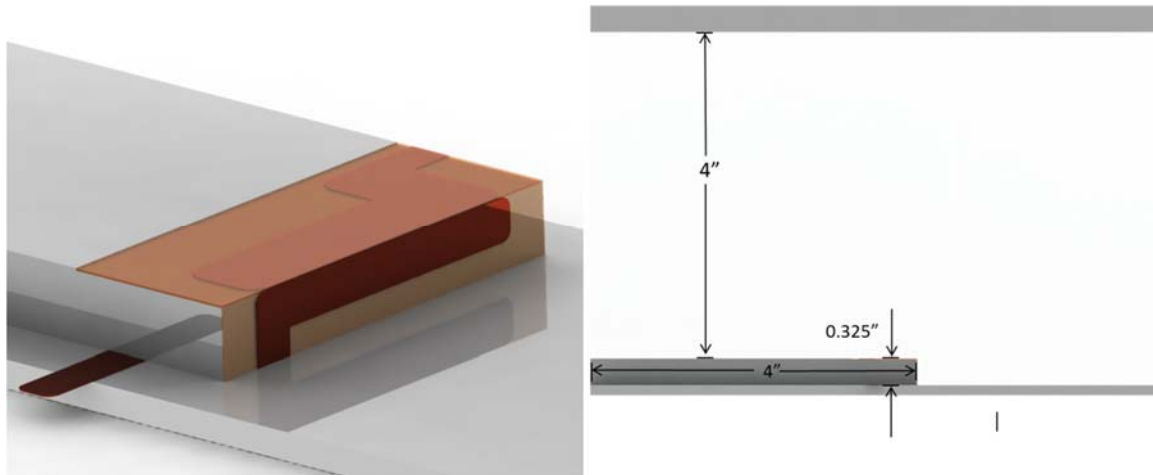
14

Figure 13: Schematic of BFS with actuator installed along with test section dimensions.

C. Electrical Hardware and Diagnostics

Actuators for each facility have slightly different features dues to installation constraints which are detailed in subsequent sections. In general, DBD plasma actuators used in this work are composed of two copper tape electrodes separated by Kapton tape dielectric arranged in an asymmetric fashion (Figure 14). A slight overlap between the electrodes is used to encourage uniform plasma generation. Actuators are flush-mounted via a small recess in all cases.
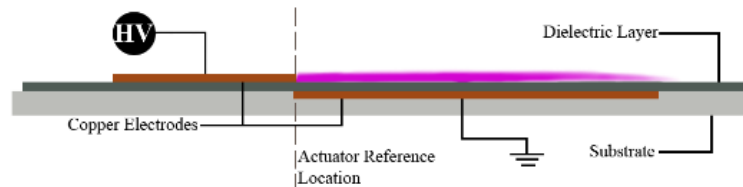

Figure 14: Asymmetric DBD plasma actuators schematic

High voltage nanosecond pulses are produced using a power supply designed and built by the Ohio State University (OSU) Nonequilibirum Thermodynamics Laboratory (NETL). The pulser is magnetic compression type and is a clone of the device used in previous work on this topic (Rethmel et al. 2011; Takashima et al. 2011; Little et al. 2012). It is capable of both positive and negative polarity outputs with bandwidth of 5 kHz. Pulse voltage is controlled by 5 kW dc power supply with output voltage 0-700 Vdc. Input signals are generated by a Tektronix AF6310 function generator. A Tektronix P6015A high voltage probe and shunt current probe are used in conjunction with a Tektronix TDS 2024C oscilloscope for electrical measurements. Representative current and voltage waveforms for ns-DBD plasma are provided in Figure 15a. Time traces like Figure 15a are used for offline calculation of instantaneous pulse power and pulse energy where the latter is calculated by integrating the product of voltage and current. Accurate calculation of these values requires correcting for the slight phase delay between the current and voltage probe signals. This delay is calculated to be 2ns through consideration of the difference in probe cable length. This is validated by noting the occurrence of current extrema near the peak of the voltage derivative. The location of the current extrema relative to the peak of the voltage derivative varies by as much as 1ns, which corresponds to a 3% change in energy. The accuracy of power and energy measurements is thus estimated at 5% based on the root sum square of 3% accuracy on the voltage probe, 2% accuracy of the current probe, and 3% due to an uncertainty of 1ns for phase delay. Other factors (measurement location, impedance matching, etc.) are not considered here, but will be quantified in the future. Note that ns-DBDs produce two distinct discharge cycles indicated by two current extrema (one negative and one positive) in

15

Figure 15a. If these events occur faster than the local acoustic time scale, it is assumed that both contribute to gas heating. This motivates the use of gross energy or the integrated absolute value of the voltage-current product. Details on these calculations can be found in Dawson and Little (2014). Pulse energy, which has been found to be the most representative parameter for ns-DBD amplitude (Little et al. 2012), is on the order of 1 mJ/cm in all cases. The characteristic signature of rapid localized heating by nanosecond pulse plasma is compression wave shown in Figure 15b. The cylindrical wave emanates from the actuator reference location (see Figure 14) while the quasi-planar wave originates from the head of plasma layer as its spreads onto the dielectric surface. Both single pulse and burst modulation are employed as described below.
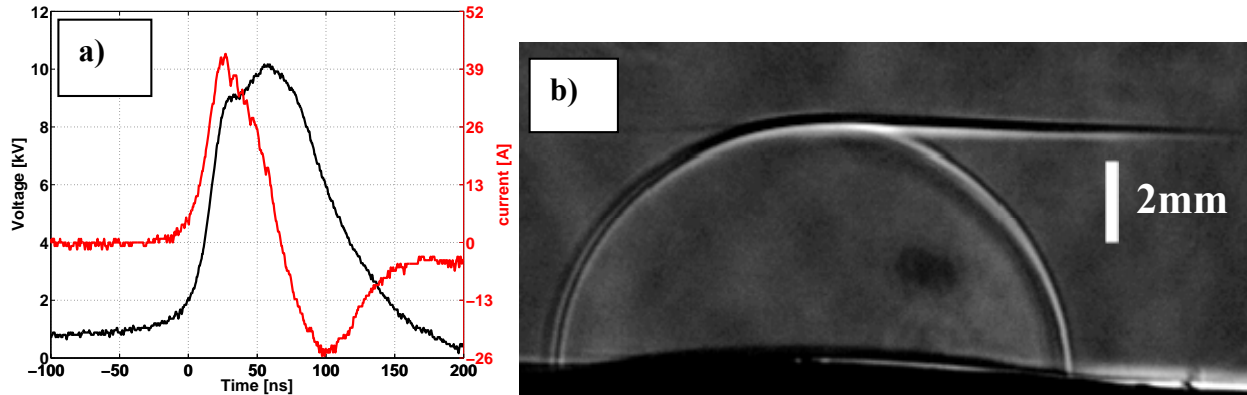

Figure 15: Sample voltage and current waveforms for positive polarity pulses (a) and characteristic discharge induced compression wave (b). Schlieren image is acquired 15μs after the pulse.

Ac-DBD plasma actuators are employed as a sanity check in the mixing layer. The ac-DBD plasma actuator uses a function generator, amplifier and step-up transformer with a turn ratio of 1:357. Maximum voltage output of the circuit is 25 kVrms with power limited to 1250 Watts. Voltage applied to the DBD load is typically 10-15 kVpp. The ac driving frequency (3 kHz) is chosen to match previous work with a similar actuator construction (Little and Samimy 2010; Dawson and Little 2013) and the transformer resonance frequency is adjusted for maximum efficiency. This construction produces near-wall velocities of approximately 3m/s in quiescent air. Lower frequency modulation is used to excite the mixing layer at the Strouhal number of interest, $St = f\theta/\overline{U} \approx 0.032$, where the value of θ is chosen depending on the location preferred for study. The effects of different low frequency modulation waveforms on mixing layer control efficacy was examined. Results showed the greatest control authority using a 50% duty cycle burst modulation waveform (Ely and Little 2013a) and this was retained for the majority of the study. A similar method is used for ns-DBD forcing where the aforementioned ac wave is replaced by nanosecond pulses. Examples of the two waveforms are shown in Figure 16. Note that pulse widths for ns-DBD waveforms are exaggerated for clarity. The maximum time-averaged velocity of the burst-modulated ac-DBD induced wall jet is 1-1.5m/s which is in good agreement with previous studies (Little and Samimy 2010). Past studies using ns-DBD devices have shown the velocities induced by burst modulation are approximately an order of magnitude lower than that of ac-DBD plasma (Little et al. 2012). Time-averaged results from tests in quiescent air confirm this with the maximum velocity for ns-DBD burst modulation being approximately 0.2-0.3 m/s. Induced velocities for single frequency (e.g. 30 Hz) ns-DBD forcing are even lower and not outside the uncertainty of the measurement.
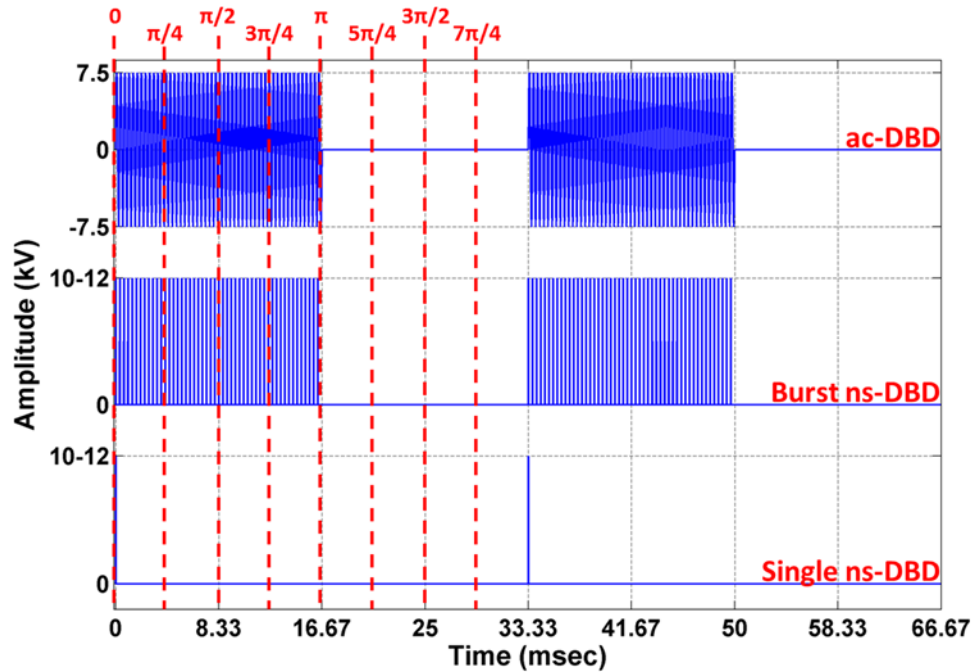
16

Figure 16: Sample time traces for 30 Hz modulated waveforms for 15kVpp ac-DBD forcing and burst/single frequency ns-DBD forcing. Red dashed lines are reference lines for phase-averaged results described later.

D. Flow Diagnostics

Pressure measurements are acquired using a MKS Baratron high accuracy differential sensor head and signal conditioner. The sensor head has a full scale pressure range of 10 Torr and an accuracy of 0.08% of reading. Data are sampled using a National Instruments PCI-6143 board and LabView. A pitot-static probe (0.375in diameter) is used for acquiring mixing layer profiles and a boundary layer probe (United Sensors BR-.025-12-C-11-.125 having a flattened tip with 0.076mm opening) is used to characterize the incoming behavior on the splitter plate and BFS. The probes are mounted on one of two motorized traverses with minimum step size of 0.001in or less. The RMS error in pressure measurements is smaller than the symbol size in all presented velocity profiles. Constant temperature anemometry is employed to further define the features and state of the boundary and shear layers. A Dantec M-unit with 55P14 probe is sampled at 20 kHz for 200,000 samples resulting in frequency resolution of 5 Hz. A 10 kHz analog low pass filter is employed in the experiment.

Schlieren imaging in the mixing layer is performed using two 254 mm (10 in) f/10 spherical mirrors in a modified Z-type arrangement where a flat mirror was used just before the knife edge to properly align the image and camera. An ImiTech Han Series CCD camera (IMB03145FT, pixel resolution of 1392x1040) is used to acquire images. A Lightspeed Technologies HPLS-36-7500 drives a 532 nm LED with pulse width of 500ns. A 1 mm by 5 mm source slit is placed directly after the LED. The knife edge is oriented horizontally thus the intensity is proportional to the density gradient in the vertical direction and the second derivative in the horizontal direction. The LED and camera are externally triggered by the same function generator that is used to run both the ns-DBD pulser and ac-DBD circuit. A LabView program is used to control delay between the input signal to the ns-pulser/ac-circuit and imaging signal to allow for phase locked images. This delay can also be adjusted to allow the propagation of the pressure wave to be viewed. Average phase-locked schlieren images are created using 50 instantaneous samples at various time delays and phases.

A LaVision PIV system operating DaVis 8.3 is used to obtain spatially resolved velocity data. Imager sCMOS cameras equipped with 50mm focal length lenses (F/1.4), 2x teleconvertors (where applicable) and narrow linewidth 532nm filters are used to capture data. A Quantel Evergreen dual-head PIV laser is used

17

to illuminate submicron seed particles (PeaSoup Smoke Machines) introduced into the entire laboratory to provide homogeneous seeding in the open-loop tunnels. For each image pair, subregions are cross-correlated using decreasing window (64^2-32^2 pixel^2 for mixing layer and 32^2-16^2 pixel^2 for BFS) multi-pass processing with 50% overlap. The resulting velocity fields are post-processed to remove vectors with peak ratio less than 1.5 and correlation coefficient below 0.5. Removed vectors are replaced by an interpolation procedure using neighboring vectors. A 3 x 3 Gaussian smoothing filter and polynomial filter are also applied to the calculated velocity field. The spatial resolution of PIV data is better than 1.7 mm for mixing layer tests and 0.25mm for the BFS. Accuracy of instantaneous velocity in both the mixing layer and BFS is estimated at < 5% of mean freestream value using subpixel accuracy of 0.1 pixels and negligible timing errors. The uncertainties in measurements of mean velocity are calculated by 95% confidence intervals using the maximum standard deviation in the mixing/shear layer and average velocity of the high and low speed (or the freestream only in the case of BFS). This results in a relative error of < 2% for ensemble average images. Thus, the RMS error for PIV measurements is estimated as < 5% of freestream in both facilities. Phase-averaged images are generated based on at least 100 samples separated by four equidistant phases (0, $\pi/2$, π and $3\pi/2$) of a given forcing period. In the mixing layer case, the forcing period is based on the low frequency modulation waveform. For all flow control experiments, data is acquired by first establishing a baseline case and then energizing the plasma actuator using a high voltage ns waveform.

VI.   Results

A. Mixing Layer

Additional baseline behavior in the mixing layer is presented in Figure 17. The momentum thickness increases linearly with downstream distance for cases with and without suction which implies the shear layer also grows linearly as expected. In this case, boundary layer suction is only employed on the high-speed side. The plotted data for each case is a combination of two different tests, one near the actuator and one in the downstream mixing layer. The mixing layer grows more rapidly in the case where suction is applied and this provides a better match to the literature (Figure 12a). The increased growth is caused by the stronger gradient due to the smaller boundary thickness on the high speed side. This gradient can be seen in Figure 17b at x = 50mm and the figure also includes some downstream profiles to show the increase in the mixing layer growth. Note that the vertical coordinate for each profile has been subtracted by the vertical location of the average velocity for the respective profile. The profile x = 50mm was chosen to avoid effects of the wake which persist up to x = 30mm for both with and without suction cases. Note that all baseline measurements have been conducted with a passive actuator flush-mounted on the splitter plate trailing edge.
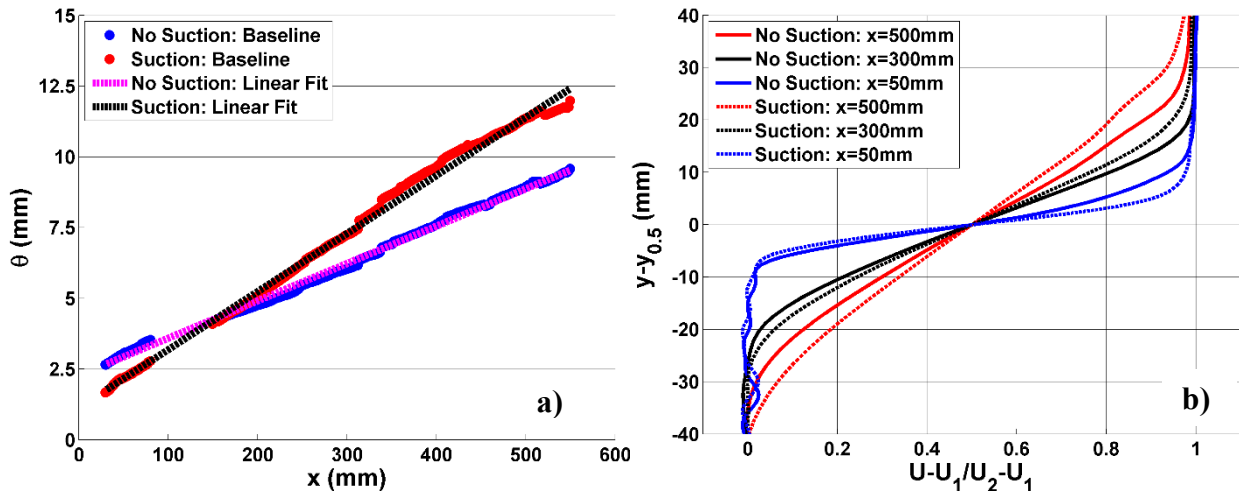

Figure 17: Momentum thicknesses (a) and velocity profiles (b) for the unforced mixing layer.

18

Actuator placement was chosen using various ac-DBD and ns-DBD waveforms as well as different actuator locations relative to the splitter plate trailing edge (Ely and Little 2013a). From these tests (which did not originally include suction), the optimal forcing location was found to be on the high speed side of the splitter plate nearest to the trailing edge as the momentum thickness increased in this case by about 30% compared to similar forcing on the low speed side. The forcing frequency used in these tests was 30 Hz which approximates the most amplified frequency at x=450 mm corresponding to a Strouhal number of approximately $St = f\theta/\overline{U} \approx 0.032$. A schematic of the actuator location along with a picture of the discharge is shown in Figure 18. Results showed that ac-DBD plasma has a substantial effect on the mixing layer mean flow by increasing the momentum thickness by 2-3 times the baseline thickness. Sinusoidal and various duty cycle burst modulating waveforms were also tested with ac-DBD forcing. The greatest increase in momentum thickness was seen using a 50% duty cycle burst modulation waveform. Surprisingly, ns-DBD forcing had no measurable effect on the mixing layer mean flow (Ely and Little 2013a). This included both burst and single frequency forcing.
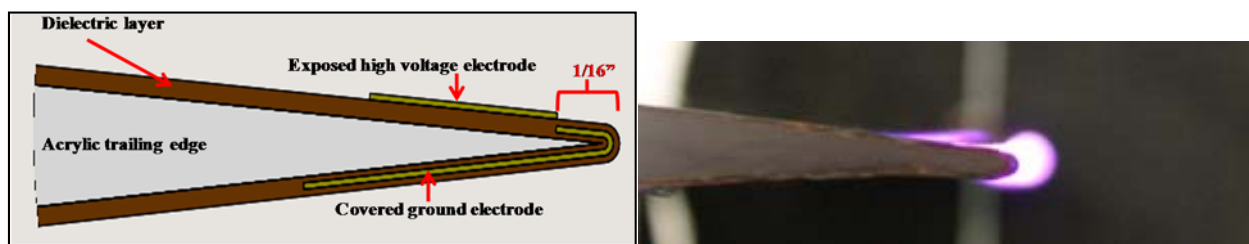

Figure 18: Schematic for actuator configuration on high speed side of splitter plate with 1/16in reference location and photograph of the energized plasma actuator.

Although no effects were seen in the mixing layer mean flow with ns-DBD forcing, phase-averaged PIV data showed the presence of a slight oscillation when burst modulation was employed. This motivated the use of suction to reduce the incoming boundary layer thickness from the onset. It is assumed that the initial conditions, specifically the boundary layer thickness, resulting wake and shear layer profile, will have a strong effect on the efficacy of pulsed heating for exciting the natural instability. Figure 19 shows the influence of suction on control authority in both ac- and ns-DBD control. The discontinuities in these curves are a result of image degradation caused by imperfections in the test section walls. Note the different scales for momentum thickness for the two plots. Two low frequency modulation cases (30 Hz and 60 Hz) are employed corresponding to St=0.032 at x=450mm and 150mm respectively for the no suction case (see Figure 16). The low frequency case (30 Hz) is used to produce maximum growth over the full extent of the test section. The higher frequency case (60 Hz) locates the region of neutral stability near the center of the test section. The modest effect of boundary layer suction on the ac-DBD performance is clear in Figure 19a. Despite the stronger velocity gradient in the mixing layer, only a slight increase in momentum thickness is observed for 30 Hz. It should be noted that with suction the predicted optimal frequency reduces to approximately 20 Hz, but 30 Hz was retained for simplicity. This may partially explain the reduced growth, but it is also likely that the maximum achievable growth may be limited by the test section height for this forcing case. The suction effects can be more readily seen at 60 Hz ac-DBD forcing as a region of saturation is clear near 300mm. The saturation of the 60 Hz ac-DBD forcing case without suction is not as apparent. In this high frequency case, the variation in baseline momentum thickness at 150mm is minor such that use of 60 Hz for both cases is not likely the cause of the difference in performance. Rather, it is believed that the amplitude of the perturbation relative to the initial conditions (i.e. momentum thickness) is larger such that a more recognizable region II is observed. The forced mixing layer downstream (x>300mm) then continues to grow linearly, consistent with region III in the literature (Oster and Wygnanski 1982; Weisbrot and Wygnanski 1988; Greenblatt and Wygnanski 2000). As before, the thermal perturbations introduced by ns-DBD forcing shows no measurable change in the absence of suction (Figure 19b). However, when suction is introduced, burst modulation of the ns-DBD produces a slight *decrease* in momentum thickness for large downstream distance.
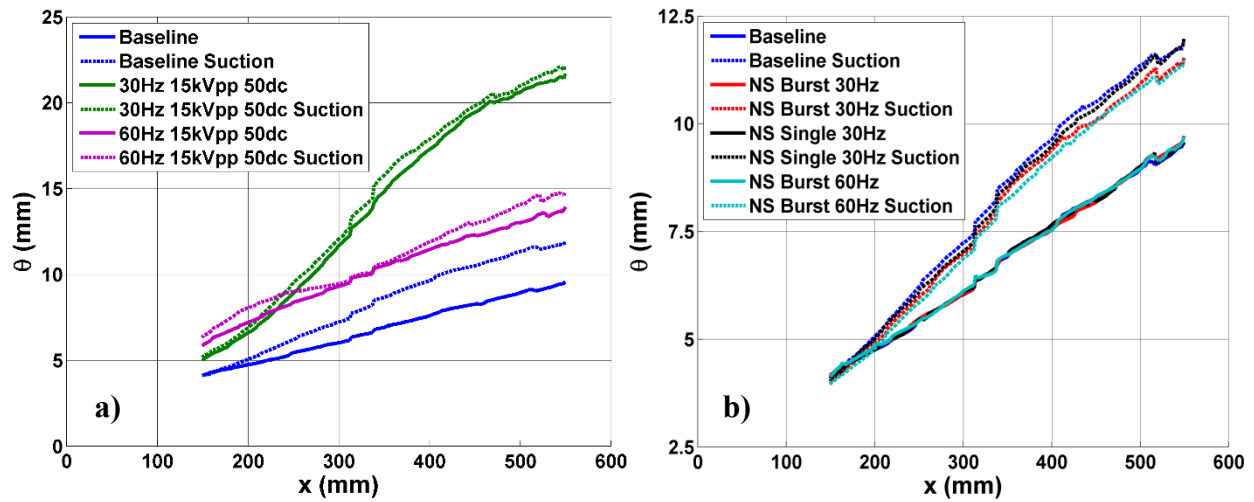
19

Figure 19: Momentum thickness as a function of distance from the splitter plate for cases with and without boundary layer suction on the high speed side of splitter plate for ac-DBD forcing (a) and ns-DBD forcing (b).

Phase-averaged PIV is used to provide insight into the dynamics in the forced mixing layer. Eight equally spaced phases are taken to view flow phenomena (see Figure 16). An example is shown in Figure 20 for ac-DBD forcing at 30 Hz and 60 Hz with and without suction. The baseline vorticity field, which is indistinguishable from the ns-DBD forcing, is also shown. Note that the diagonal lines are by-products of test section window imperfections that become highlighted by the laser sheet. Vertical lines near the center of the images are caused by image stitching between the two cameras. One can also see the vorticity from the honeycomb head loss device on the low speed side has not fully dissipated. Regardless, large coherent structures are observed for both frequencies and dominate the spanwise vorticity as expected. All images are for the same phase of the forcing period. For the case of 60 Hz forcing, the vorticity field shows the rollup of the mixing layer into discrete vortices at a downstream distance of x=300-350mm. It appears that a similar phenomenon is beginning to occur for 30Hz forcing just outside the test section. Both of these results are consistent with the mean flow and expected dynamics for these frequencies. Only slight changes in the vortex structure are observed when suction is applied. There is modest increase in vortex size which leads to the slight increase in momentum thickness seen in Figure 19. There is also a decrease in the strength of the braid region due to the accelerated spatial growth. Suction affects the location of the primary vortex structures by shifting them slightly downstream for a given phase. This is most apparent for the vortex located near x = 300mm in the 60 Hz forcing case (Figure 20e). This structure appears to be almost a discrete vortex, more so than the case without suction. Thus, the discrete vortex structure has developed more quickly than the case without suction which is consistent with the momentum thickness data and expected growth with from theory as *St* is slightly greater than 0.03 at x=225mm. The phase averaged vorticity data shows characteristics that are qualitatively similar to established literature (Oster and Wygnanski 1982; Ho and Huerre 1984; Weisbrot and Wygnanski 1988). However, one notes that the majority of studies examine mixing layers excited by sinusoidal signals. In this case, the perturbation provided by an ac-DBD plasma discharge is more similar to a pulsed wall jet.
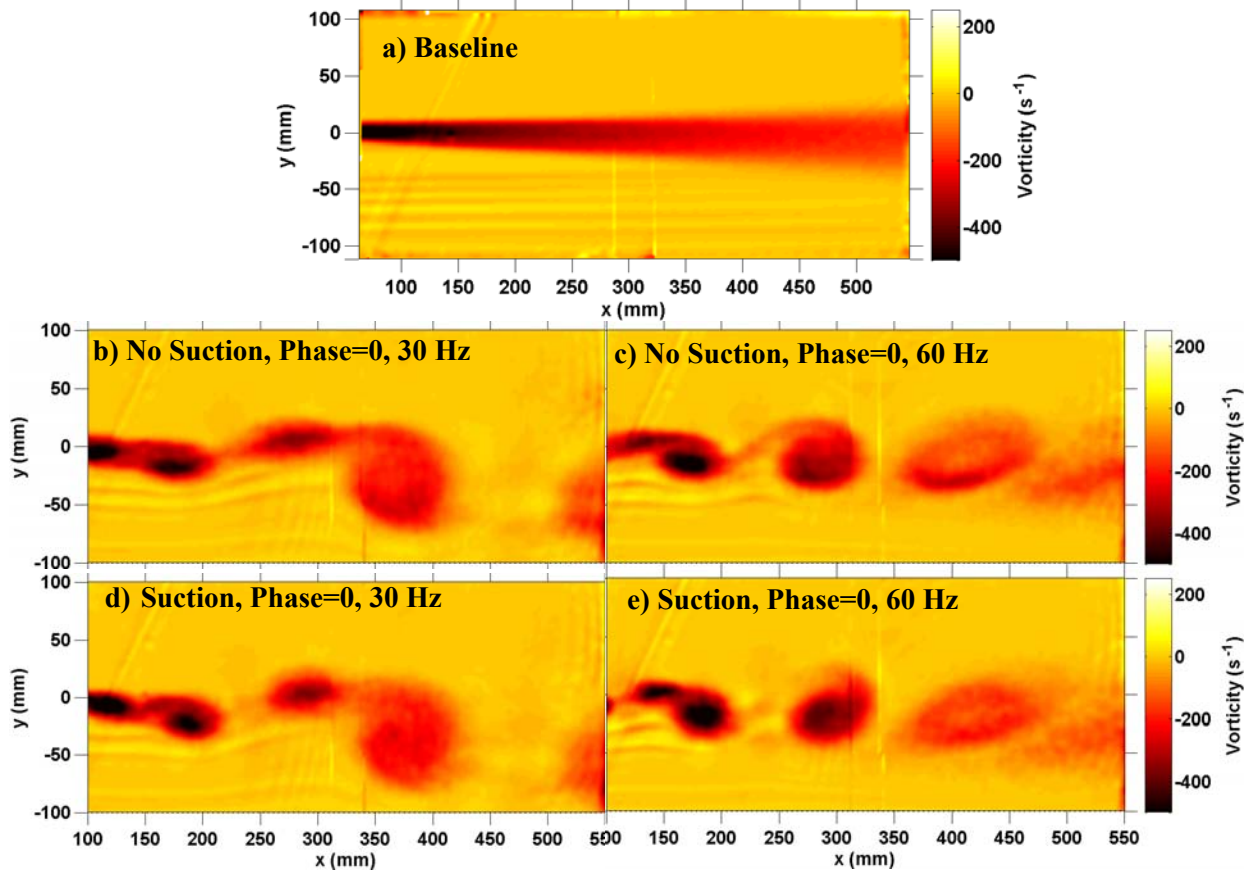
20

Figure 20: Phase-averaged PIV data for baseline and 15kVpp ac-DBD forcing.

Turbulence characteristics are provided to gain further insight into the validity of the experiment and the curious ns-DBD behavior (lack of control authority). Specifically, the Reynolds shear stress is investigated since it provides information on the development of various regions in the excited mixing layer. Briefly, the linear growth of momentum thickness in region I of an excited mixing layer should eventually saturate and stop growing in region II where the instability waves rollup into discrete vortices (Oster and Wygnanski 1982). This is observed in Figure 19 and Figure 20 near the end of the test section (30 Hz) and near x=300mm (60 Hz). Another observation for transition to region II deals with the development of the Reynolds shear stress. If the Reynolds shear stress decreases and develops negative regions, the mixing layer growth has either slowed or stopped completely and the turbulence now transfers energy to the mean flow. This negative production of turbulent kinetic energy can occur across the complete lateral extent and such behavior was observed for ac-DBD forcing consistent with literature (Ely and Little 2013b). This provides additional assurance that, despite some developmental features, the ac-DBD plasma excited mixing layer (and the facility behavior in general) is consistent with literature and theory.

Reynolds shear stress for burst modulated ns-DBD forcing is shown in Figure 21. The lack of a complete collapse of *Re* shear stress profiles indicates that the mixing layer has not become fully self-preserving with respect to turbulence quantities as mentioned in Section V.A. Trends can still be viewed in the data although this self-preserving state has not been completely reached. Without suction, the profiles for both the unforced and forced mixing layer show no changes outside of the measurement repeatability. When suction is applied, it can be seen that ns-DBD forcing produces a *decrease* in the peak of the shear stress as opposed to an increase seen for ac-DBD forcing and excited mixing layers in general. This is seen for both 30 Hz and 60 Hz ns-DBD forcing where the effect of the latter is more pronounced. These results are in agreement with mean flow behavior and show ns-DBD plasma decreases the turbulent nature of the mixing layer.
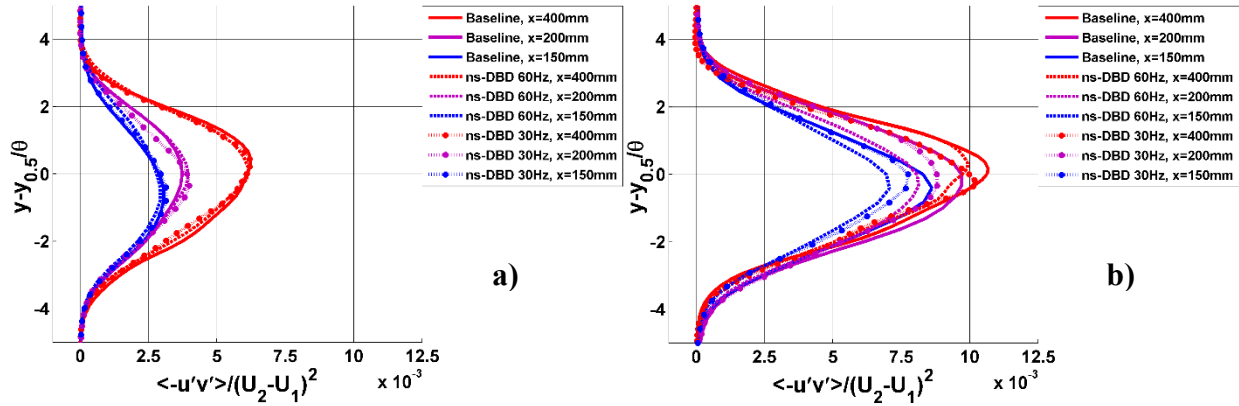
21

Figure 21: Reynolds shear stress at various downstream locations with 30 Hz and 60 Hz burst modulated ns-DBD forcing for both without (a) and with (b) boundary layer suction on the high speed side.

The existence of a slight decrease in momentum thickness suggests the mixing layer is slightly stabilized by ns-DBD burst mode forcing. This was confirmed through examination of the Reynolds shear stress and the lack of any clear excitation of spanwise vorticity. However, a very slight oscillation in spanwise vorticity fields could be observed in movies of the ns-DBD burst-mode excited case (Ely and Little 2013b). In order to better view these oscillations, the mean flow for each case was subtracted from the phase-averaged images in order to show only fluctuations in velocity. The y-velocity fluctuations for each forcing case, with and without suction, are shown in Figure 22. The y-velocity fluctuations for ac-DBD forcing are also given for reference. Note the contour scale used for ns-DBD forcing is an order of magnitude lower than for ac-DBD. Phase $3\pi/4$ and phase $7\pi/4$ are shown for 30 Hz forcing and 60 Hz forcing, respectively. For single pulse ns-DBD actuation, the velocity fluctuations appear to be random with boundary layer suction producing a slightly greater fluctuation intensity (Figure 22a,b). For the momentum perturbations provided by the ac-DBD plasma (Figure 22c,d,g,h), the effect is clear where the pairing of a positive and negative velocity region represents a clockwise vortex structure. The growth and decay of these velocity fluctuations are consistent with data shown previously for ac-DBD plasma (Figure 20). When burst modulation is used for ns-DBD plasma (Figure 22e,f,i,j), there is also a formation of paired positive and negative vertical velocity fluctuations, although amplitudes are an order of magnitude lower in comparison to ac-DBD forcing. This suggests that the shear layer instability is being excited but only slightly. The structure locations match very well with those for ac-DBD forcing confirming that the instability is being triggered with similar temporal features. Suction seems to slightly increase the magnitude of the velocity fluctuations and decrease the coherent nature of these velocity pairs. It is observed that the ns-DBD is producing an oscillation in the flow, but it is approximately one order of magnitude weaker than the ac-DBD case. This is an unexpected result as coherent oscillations in this frequency range are expected to increase the momentum thickness. In the suction case specifically, the opposite effect is observed in that the momentum thickness and *Re* shear stress values actually *decrease* indicating a slight stabilization of the flow.
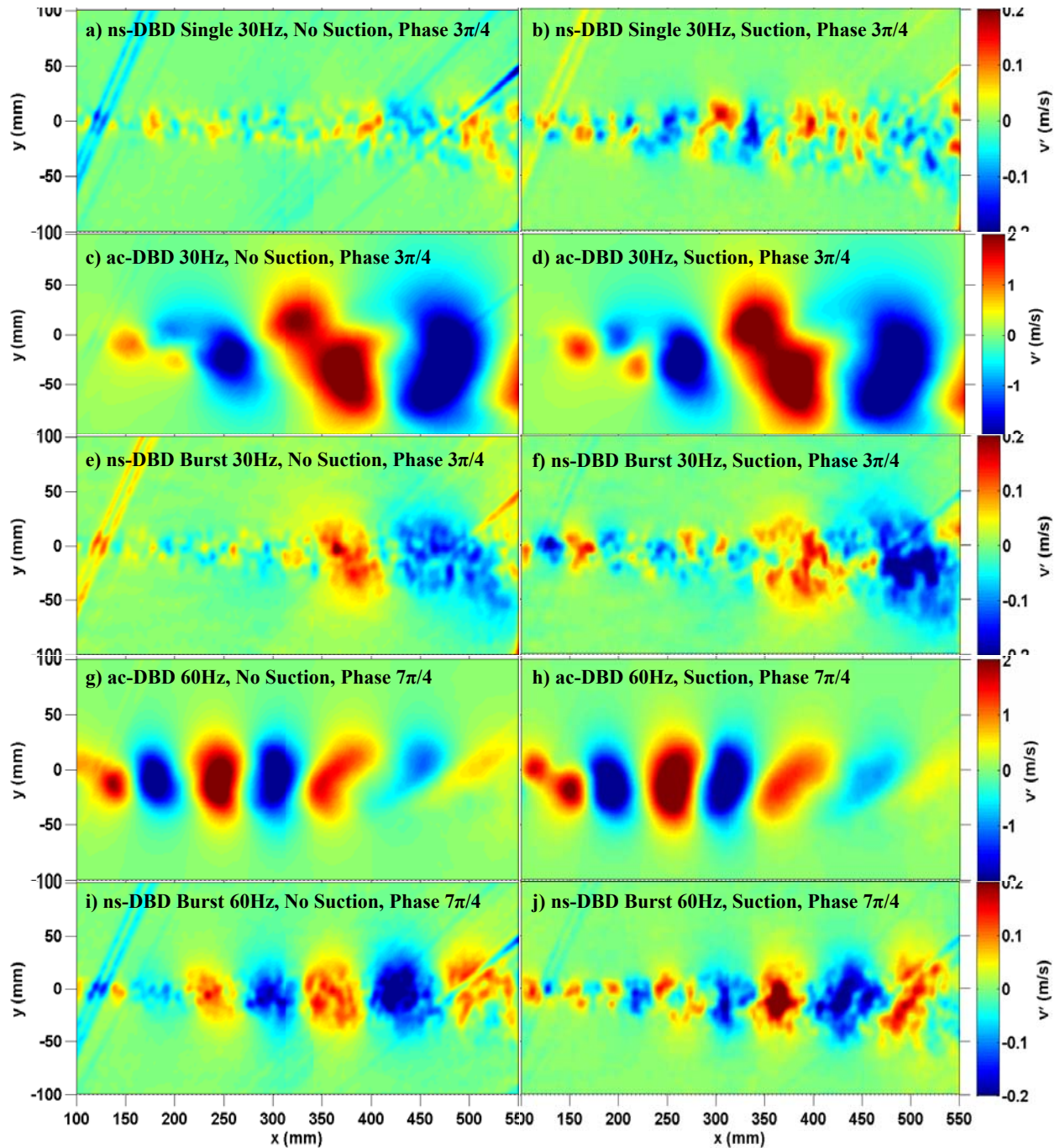
22

Figure 22: Phase-averaged y-velocity fluctuations without suction and with suction for 15kVpp ac-DBD, single pulse ns-DBD, and burst modulation ns-DBD forcing.

PIV and schlieren data are acquired near the actuator to obtain more insight into the physical mechanisms associated with ns-DBD perturbations. Similar data is also shown for ac-DBD as a comparison case. As discussed previously, the ac-DBD plasma control mechanism is widely accepted to stem from near surface momentum addition. This is used to excite the shear layer instability in the mixing layer studied here. The ns-DBD plasma control mechanism is believed to be primarily thermal (sometimes called thermoacoustic) and the same shear layer instabilities are targeted. It should be noted that ac-DBDs possess some thermal effects that have been seen in both experiments and computations (Likhanskii et al. 2008;

23

Opaits et al. 2008), but these have been deemed negligible (Enloe et al. 2004; Jukes et al. 2006; Sung et al. 2006). Similarly, ns-DBDs produce some momentum, but the scale of the velocities is approximately an order of magnitude lower in quiescent conditions and likely negligible at most practical flow speeds (Roupassov et al. 2009; Little et al. 2012). Sample phase-averaged images for both ac and ns-DBD perturbations in the mixing layer without suction at phase = π are shown in Figure 23. These images are all baseline-subtracted. There is a small time delay between the schlieren and PIV images such that the pressure wave has already propagated out of the field of view in the PIV case. From these images, the fundamental difference between each type of actuation is apparent. Ac-DBD forcing produces a pocket of heat that resides on the lower side of the splitter plate trailing edge, but does not extend far downstream (Figure 23a). This is in qualitative agreement with schlieren images of Opaits et al. (2008). This pocket of heat sheds downstream and dissipates quickly when the plasma is off leaving only small amplitude residual heat near the splitter plate trailing edge. On the other hand, ns-DBD forcing provides a comparatively stronger heating effect that extends further downstream. This heated area is seen to grow and decay with the modulated frequency of 30 Hz but never fully dissipates presumably due to the wake existence. The amplitude and size of the residual heated area is larger in the case of ns-DBD forcing. Pressure waves are also seen as a result of the rapid localized heating in Figure 23b. In addition to the strong primary pressure wave that moves downstream, a weaker pressure wave on the upstream side of the high voltage electrode is visible. This is caused by a small secondary discharge similar to those observed in high-speed imaging by Roupassov et al. (Roupassov et al. 2009). Reflected flat pressure waves from previous ns-DBD plasma discharges can be seen at the top and bottom of Figure 23b. Ac-DBD forcing produces a large velocity perturbation as expected (Figure 23c). The velocity magnitudes (above the baseline) are in the expected range of values based on quiescent air tests (~1 m/s). The small region of negative velocity on the bottom of the splitter plate likely stems from some of the induced flow wrapping around the trailing edge, but the majority is seen to be directed downstream. Positive momentum production is negligible in the case of burst ns-DBD forcing and instead there is a slight decrease in velocity on the high speed side in comparison to the baseline (Figure 23d). This reduction in velocity is seen both with and without suction for ns-DBD forcing. The cause of the reduced velocity will be discussed further, but these results confirm the negligible aspects of ns-DBD momentum addition at least for the flow conditions studied here and more widely in the literature.
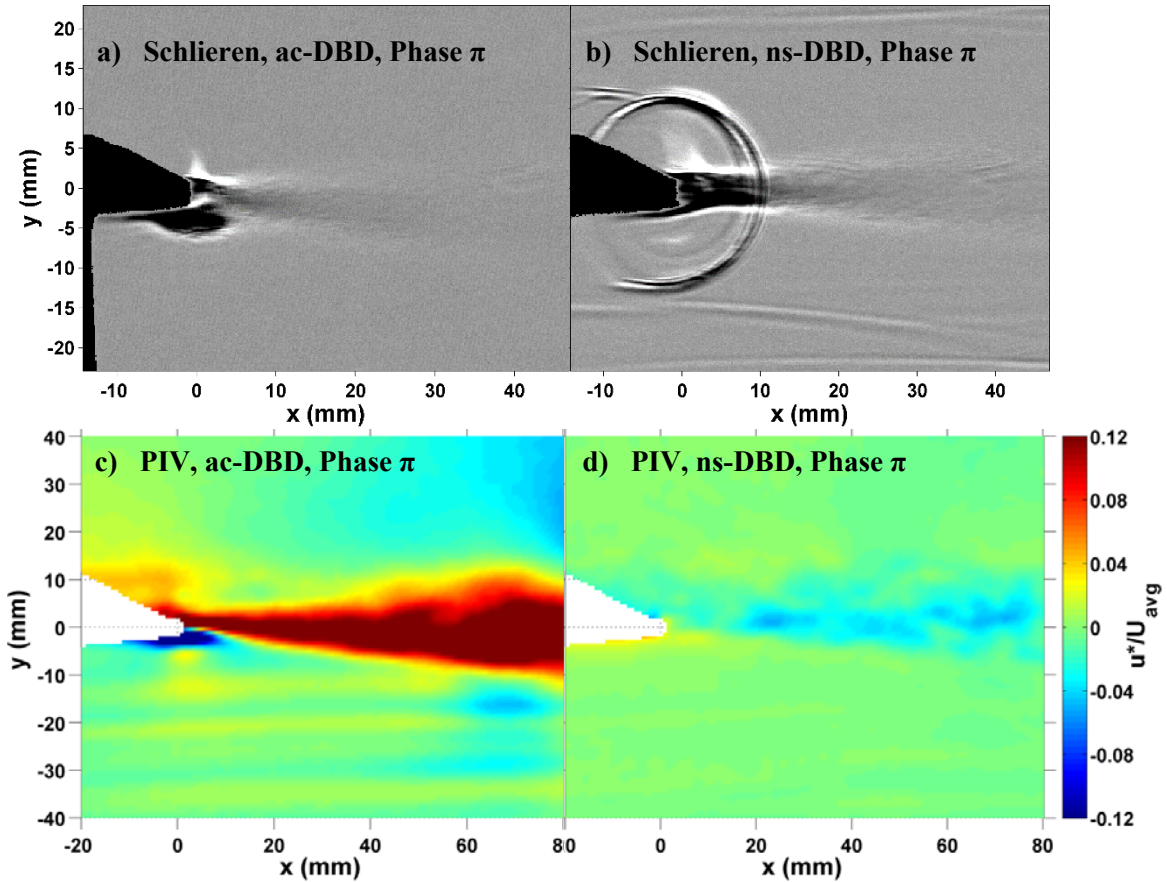
24

Figure 23: Phased-averaged near actuator Schlieren and PIV for 15kVpp ac-DBD and burst modulated ns-DBD forcing. All cases are for 30 Hz forcing without boundary layer suction.

To better quantify the differences between ac and ns-DBD forcing, baseline subtracted velocity and schlieren intensity profiles are plotted at a downstream distance of x = 7mm from the splitter plate trailing edge (Figure 24). Note that these profiles are taken at a time delay of 1μs in order to avoid contamination of the profiles by the pressure wave. Figure 24 shows the effect of boundary layer suction for both forcing cases as well. Data for single pulse ns-DBD forcing is not shown as the schlieren intensity and velocity production were negligible. In the schlieren profiles (Figure 24a), the difference in the intensity for ac-DBD and ns-DBD forcing is substantial with the latter being 3-4 times greater. The effect of boundary layer suction for ns-DBD plasma is also apparent as there is an increase of the positive peaks and a slight decrease in the negative peaks. This shows that more heat propagates downstream when suction is applied due to a reduction in the ratio between boundary layer thickness (which eventually becomes a wake) and heated region. Also note the slightly smaller spread in the lateral direction of the intensity profiles when suction is applied which is consistent with the smaller size of the initial mixing layer. There is a slight increase in the positive peak of the schlieren intensity for ac-DBD forcing with suction but this increase is small especially when compared to ns-DBD. Further downstream, the schlieren intensity for ac-DBD forcing dissipates and becomes negligible while the intensity, representative of the heating effects, for ns-DBD forcing remains measurable. The propagation of heated gas has been observed in boundary layer transition studies with ns-DBDs (Michelis et al. 2013). Changes in the baseline subtracted velocity profile are also seen when suction is applied (Figure 24a). For ac-DBD forcing, an additional increase of about 0.5 m/s is seen in the positive peak. As discussed previously, a negative velocity difference is produced on the high speed side when the mixing layer is perturbed by ns-DBD forcing. The thickness of this low velocity region is similar to the incoming boundary layer thickness (thinner with suction and thicker without). The velocity also decreases further with suction, suggesting the effect is connected to the initial conditions. A negative velocity

25

difference is seen in the case of ac-DBD plasma in the lower region of the trailing edge. This is likely due to part of the induced velocity being directed upstream on the lower surface.

In summary, measurements near the actuator show that the ac-DBD primarily generates momentum with a small heated region that only exists near the splitter plate trailing edge. The heating effect for ns-DBD forcing is much stronger and extends further downstream while momentum production is negligible as expected. Pressure waves produced by ns-DBD forcing do not appear to be important in the development of the mixing layer. It should be noted that the burst frequency employed is not high enough to produce a cumulative heating effect that results in a stronger individual pressure wave. Rather, each pulse produces a single pressure wave which results in the reflective pattern in Figure 24b. These results along with the absence of a measureable effect for single pulse ns-DBD forcing suggest that the pressure wave does not contribute to flow control at least in this particular case.
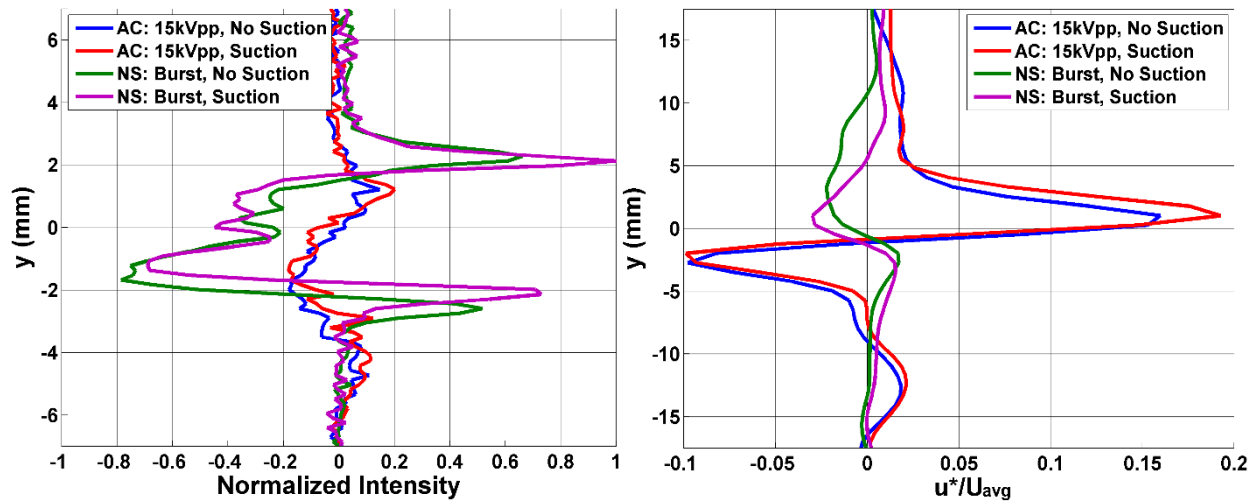

Figure 24: Schlieren intensity (a) and velocity (b) profiles for cases with and without suction at x = 7mm. Note all cases are for 30Hz modulation frequency and u* indicates that the baseline velocity has been subtracted.

The reduced velocity in the burst-modulated ns-DBD case, presumably due to heating effects, is observed throughout the mixing layer downstream and shown in Figure 25. Note that the images in the figure are baseline subtracted and different scales are used to bring out features between the two forcing frequencies. A dashed line is added to show where the y-location where mean flow velocity, U, equals to the average velocity, U_{avg}, thus separating the high and low speed sides of the mixing layer. When boundary layer suction is applied, the reduced velocity exists primarily on the low speed side of the downstream mixing layer. Without suction, it essentially bisects the high and low speed sides, but at a smaller magnitude. This further supports the decrease in momentum thickness in the ns-DBD forced suction cases.
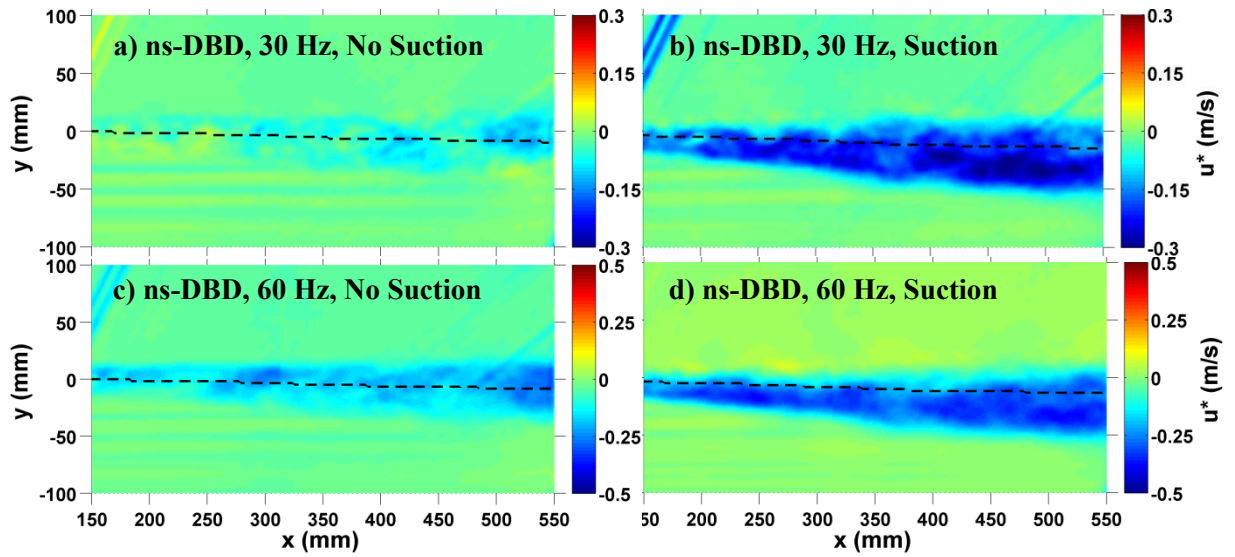
26

Figure 25: Baseline-subtracted streamwise velocity contours for burst-modulated ns-DBD forcing at 30 Hz and 60 Hz, with and without boundary layer suction. Note different velocity scales. Dashed line represents location where U=U$_{avg}$.

It should be noted that although different velocity scales are used for 30 Hz and 60 Hz in Figure 25, the actual difference between the magnitudes of the reduced velocity seen when boundary layer suction is employed is only about 0.05 m/s, about 0.7% of the average velocity between the two streams. The relative error of these measurements is roughly 1.0% of the average freestream velocity, so the difference between the magnitudes with and without suction does not fall outside the uncertainty of these measurement. Regardless, the observations are repeatable for different experiments and measurement techniques. Thus, it appears that the negative velocity difference is not some artifact of the PIV processing but rather a physical response of the flow to the ns-DBD perturbation. This response is to slightly reduce the growth of the mixing layer which results in the behavior observed in Figure 25. This, along with other results discussed previously, confirms that the mixing layer is somewhat stabilized by ns-DBD forcing in the mean even if weak fluctuations are produced at some strongly amplified frequencies.

The initial results of boundary layer suction (along with general literature) suggest that thinner boundary/shear layers are more amenable to thermoacoustic excitation for aerodynamic flow control. This motivated the use of additional boundary layer suction in the mixing layer. Suction was added to the low speed side in an effort to further reduce the initial momentum thickness. The resulting boundary and mixing layer parameters are shown in Table 1. All boundary layer characteristics are acquired on the high-speed side at the trailing edge. In both velocity cases, the natural boundary layer on the high-speed side is turbulent with shape factor in the range 1.4-1.5. Suction has a significant effect on the boundary layer characteristics and is able to reduce the natural thickness substantially. Referring to the shape factor, the boundary layer remains turbulent or highly transitional in all cases. Suction has an obvious influence on the boundary layer and subsequent initial mixing layer momentum thickness. The latter deserves special comment. The wake region persists to ~ 30mm downstream of the splitter plate. Thus, the actual initial momentum thickness is somewhat difficult to define. A decision was made to approximate the initial mixing layer momentum thickness by linearly extrapolating the data to x = 0mm based on 2-3 downstream measurements. This is justified considering that linear growth of unexcited mixing layers is well established and previously verified in this facility both with and without suction (see Figure 17). As the true shear layer profile is realized around x ≈ 30mm, these values are an underestimate and should be only used as an approximation. The same comment applies to Reynolds numbers in Table 1. Even with this underestimate, the initial momentum thickness is presumed to be substantially greater than those found in successful ns-DBD control studies (e.g. airfoil leading edge). Note that a lower speed case (U$_2$=6.1m/s with r=0.24) is also surveyed.

27

Table 1: Boundary layer and mixing layer characteristics.

Suction case	δ [mm]	δ^* [mm]	θ_{BL} [mm]	δ^*/θ_{BL}	θ_0 [mm]	$Re_{\theta o}$
r=0.28, U_2 = 11.9 m/s						
No Suction	12.8	2.4	1.7	1.4	2.1	1270
Case 1	9.9	0.9	0.8	1.2	1.0	605
Case 2	9.5	0.9	0.7	1.3	1.0	605
Case 3	2.2	0.7	0.4	2.0	0.9	545
Case 4	2.3	0.7	0.3	1.9	1.2	725
r=0.24, U_2 = 6.1 m/s						
No Suction	14.5	2.8	1.8	1.5	2.6	840
Case 1	6.3	1.1	0.5	2.1	2.2	710
Case 2	6.4	1.2	0.5	2.1	2.2	710
Case 3	2.5	0.7	0.4	1.6	0.9	290
Case 4	2.8	0.8	0.4	1.8	0.9	290

For completeness a variety of DBD actuator arrangements were tested on this new suction configuration. Various actuator configurations are described in Table 2. The dimensions of the high voltage electrode (HVE) are held constant while the ground electrode (GE) is varied in one configuration (Actuator 4). Note that the actuator reference location is the interface of the exposed and covered electrode (Figure 14). This is also the expected region of strongest gas heating. Thus, it is desirable to place this location nearest the most receptive region of the flow in question. In the mixing layer, this is at or very near the splitter plate trailing edge. The DBD geometry somewhat complicates this conventional wisdom since the HVE generates a slight geometric discontinuity due to its thickness (0.09mm). Consequently, ns-DBDs are often installed with the discharge directed upstream to avoid disturbing the incoming boundary layer ahead of the plasma. Since the ns-DBD flow control mechanism is primarily thermal, or least symmetric if associated with a quasi-cylindrical shock front, it is generally assumed that directional dependence is minimal. Table 2 and Figure 26 detail the variations that have been examined here. Both the discharge location and possible disturbance of the incoming boundary layer have been considered in this test matrix. Note that the origin of the coordinate system is placed at the splitter plate trailing edge. The DBD actuator is installed on the high-speed side of the splitter plate trailing edge in all cases. The spanwise length of the overlapping interface for all actuators is 254mm. Representative electrical traces for the 2nd generation suction splitter plate tests are shown in Figure 27. The most notable parameter is the pulse energy which is approximately 0.65 mJ/cm.

Table 2: Actuator configuration and geometries.

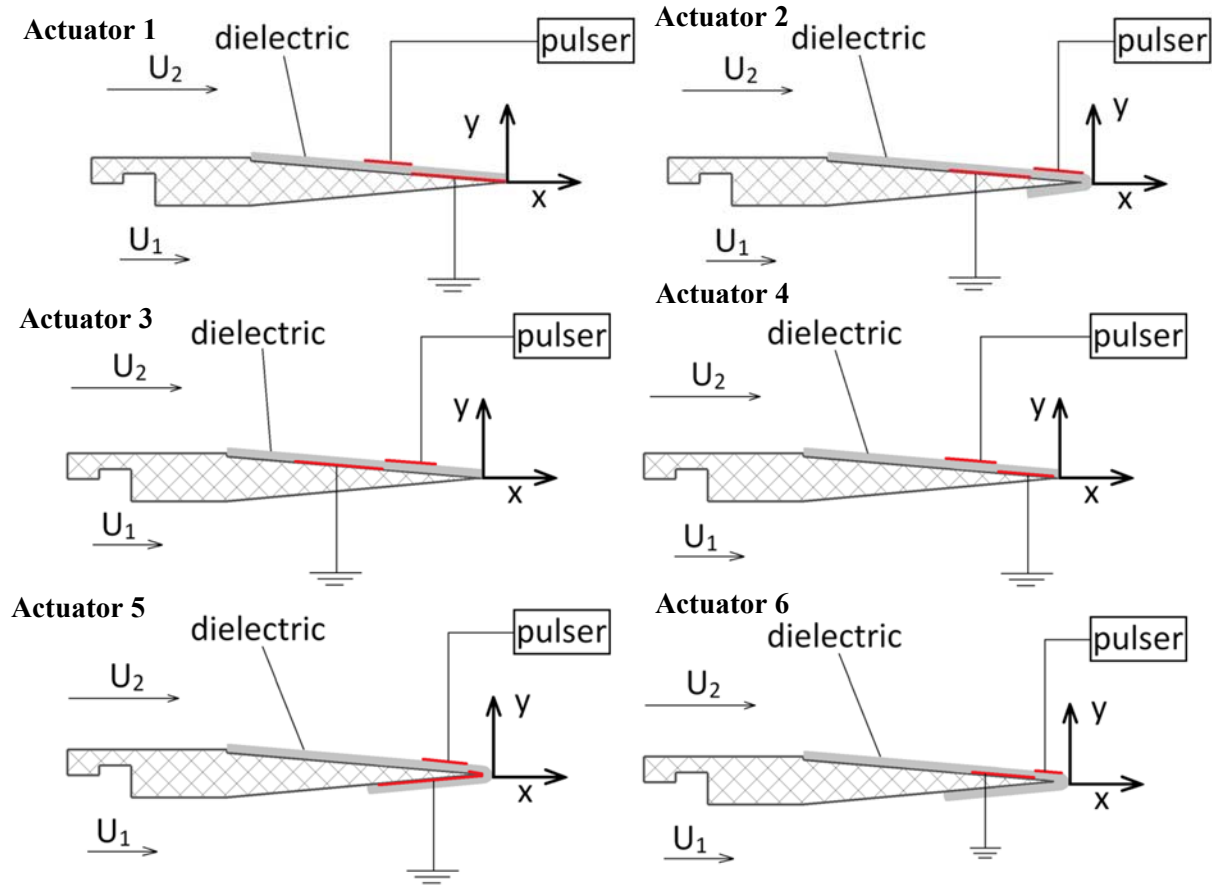| Actuator Configuration	Width HVE [mm]	Width GE [mm]	Actuator reference location, x [mm]	Discharge direction
1	6.35	12.7	-12.7	Downstream
2	6.35	12.7	-7.9	Upstream
3	6.35	12.7	-14.3	Upstream
4	6.35	6.35	-7.9	Downstream
5	6.35	12.7	-1.4	Downstream

Figure 26: Various mixing layer actuator configurations. Note dielectric thickness is exaggerated.
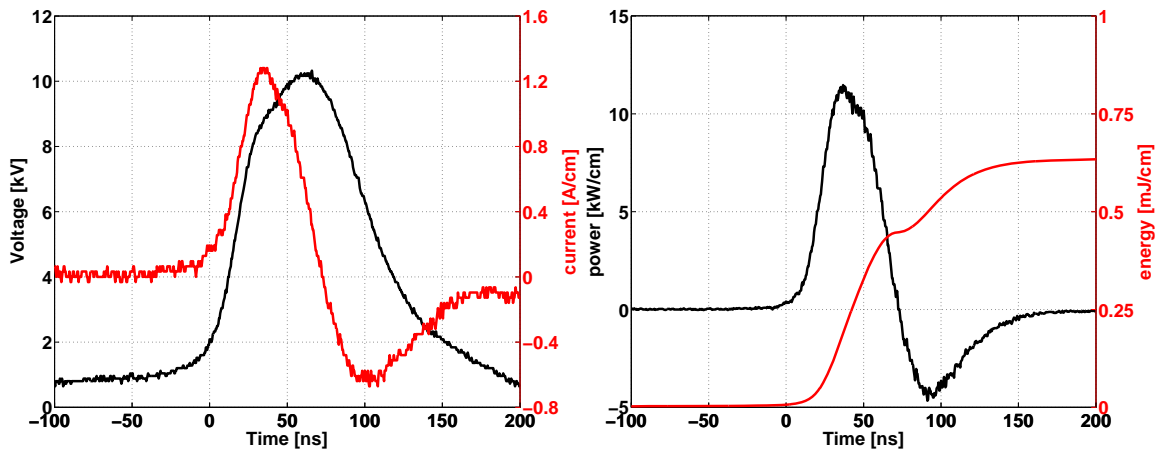

Figure 27: Voltage, current, power and energy traces applied to the DBD load in 2nd generation suction tests.

Measurements with all actuator arrangements are taken with single pulse forcing at a frequency that maintains a Strouhal number near $St_\theta \approx 0.032$, where θ is the momentum thickness of the (unforced) shear layer at the x-location of interest. In essence, the forcing frequency is chosen to maximize mixing layer momentum thickness at the measurement location. This corresponds to the location at which linear growth

of the excited mixing layer begins to saturate just preceding the roll-up of instability waves into discrete vortices. As before, the resulting actuation frequency in the high-speed case is 30Hz. In the lower speed tests, a forcing frequency of 15Hz is employed for simplicity. The choice of these forcing frequencies is only an approximation to the target St_θ as the mixing layer conditions are changed by suction and velocity variation. This approximation was deemed acceptable given the very clear mixing layer response to forcing with ac-DBDs in similar conditions shown previously. *If the ns-DBD exhibits control authority in this mixing layer, it should be clearly visible using these forcing conditions*. The velocity is measured with a pitot-static probe at x = 500mm and primarily at only one y-location (y = -40mm) to gauge the effect of forcing at various conditions with minimal experimental effort. The validity of probing a single location on the low speed side of the mixing layer to test for control authority was previously verified for ac-DBD forcing by (Ely and Little 2013a). Table 1 indicates that the various suction cases have a strong effect on the high speed boundary layer as the thickness is reduced from 12.8mm to 2.2mm in the most extreme case at $U_2 \approx 11.9$m/s. This results in an estimated initial mixing layer momentum thickness that is approximately half of the no suction case. Despite this dramatic change, ns-DBD forcing in the various configurations does not demonstrate control authority. The low-speed tests ($U_2 \approx 6.1$m/s) are performed to determine if suction could further reduce the boundary and initial mixing layer thickness below that of the high speed case. This was not entirely successful, but a reduction is still observed (14.5mm to 2.5mm) with momentum thickness ranging from 2.2-0.9mm. In the interest of completeness, ns-DBD forcing is tested here as well. The use of Actuator 1 with mixing layer case 3 shows some control authority in the low-speed flow (Figure 28). As actuation is applied, the momentum thickness of the mixing layer increases from a baseline value of 13.7mm to 14.4mm (5%) at the streamwise location x = 500mm. Note that the greatest response in the mean velocity profile is observed on the low-speed side. This result is believed to be attributed to the slight momentum production of ns-DBD, being sufficient to influence this low-speed flow. This assumption is supported by the 11.9m/s results which possess similar initial conditions, but do not show control authority.
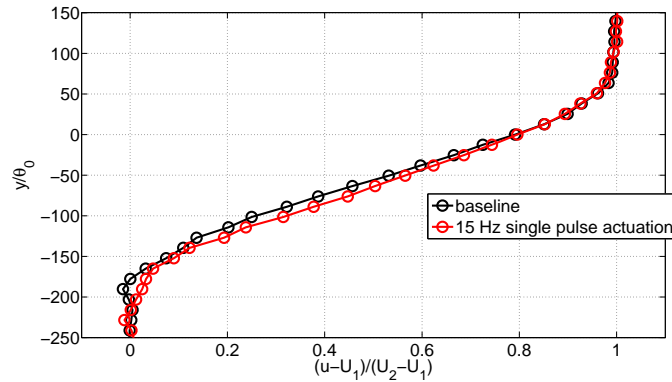

Figure 28: Baseline and ns-DBD controlled velocity profile for Actuator 1 and Case 3 at x = 500mm.

It should be noted that the influence of the splitter plate trailing edge on control authority in the low-speed case is profound and primarily dependent on the thickness of the trailing edge. Namely, if the dielectric material is wrapped around this region, a lack of control authority can result even in the same forcing conditions as Figure 28. In reality, a wake is formed downstream and the control authority observed in Figure 28 is strongly dependent on this. Finally, the characteristics of the low-speed side boundary layer deserve comment. Since this facility uses a head loss device rather than a separate flow supply, the low-speed side has relatively high turbulence and its boundary layer is very much distorted. All these effects (splitter plate trailing edge/wake, distorted low speed boundary layer) are likely influential in the lack of ns-DBD control authority. However, the strong effect of ac-DBD plasma serves to emphasize the fundamentally different physical processes associated with ns-DBD and thermal perturbations in general compared to momentum-based devices.

The mixing layer results presented here are in general agreement with Benard et al. (2014) on a BFS. A similar lack of control authority was also observed in efforts to control turbulent boundary layer separation over the deflected simple flap of a high-lift airfoil (Little 2010). In this high-lift airfoil case, the lack of control authority could not be directly attributed to boundary layer thickness since other complicating factors existed (pressure gradient, curvature, uncertainty of separation location, etc.). This motivated the mixing layer work from the onset. Recently, Correale et al. (2014a) showed ns-DBD efficacy on a BFS undergoing laminar separation. This experiment was conducted to mimic the airfoil leading edge laminar boundary layer separation control situation. In this case, the control mechanism is attributed in part to ns-DBD induced boundary/shear layer transition. Indeed, ns-DBD induced boundary layer transition has been observed on an airfoil leading edge (Little et al. 2012). Depending on the angle of attack and actuation frequency, this active trip scenario could approximate passive boundary layer tripping (high frequency forcing) or produce a train of coherent structures (low frequency forcing) leading to "classical" boundary layer separation control via excitation of the shear layer instability (Greenblatt and Wygnanski 2000). Evidence for both scenarios has been observed in studies on an airfoil leading edge, but the precise nature of the boundary layer is unknown. In summary, ns-DBDs have yet to demonstrate clear excitation of the Kelvin-Helmholtz instability (leading to separation control for example) in definitively turbulent boundary/shear layers under negligible pressure gradient. This has led to suggestions that ns-DBDs are limited to applications in laminar boundary/shear layers. However, consideration of flow control using thermal perturbations in general does not support this conclusion. Control authority using pulsed lasers and arc plasmas has been demonstrated in high-speed flows having turbulent boundary layers and negligible pressure gradient (Lazar et al. 2008; Kearney-Fischer et al. 2009; DeBlauw et al. 2014). Thus, it appears that a key parameter governing ns-DBD control authority and thermal flow control techniques in general is the local boundary/mixing layer thickness or, more accurately, the thickness relative to some length scale associated with the thermal disturbance. Presumably, this unknown length scale should be related to the amplitude of energy deposition. It is also plausible that Re based on some measure of boundary layer thickness is influential. In an effort to support this hypothesis, attention is shifted to examination of a BFS which allows for study of a thinner turbulent shear layer in comparison to the mixing layer facility.

B. Backward Facing Step

It is believed that the initial conditions of the shear layer in question have a strong influence on the efficacy of ns-DBDs and thermal perturbations in general for flow control. The mixing layer study, as well as the general literature, seems to support this hypothesis. However, explicit proof has yet to be shown. The primary objective in using the BFS facility was to generate a thin, turbulent initial boundary/shear layer to shed light on this issue. Boundary layer measurements at the step corner (x = 0mm) indicate that this has been achieved. Due to the relatively large contraction ratio (13.8:1) and a short boundary layer evolution length from the contraction exit (approximately 100mm), the boundary layer disturbance thickness ($\delta \approx$ 1.3mm) and momentum thickness ($\theta_0 \approx$ 0.15mm) are very small compared to the previous mixing layer case. The boundary layer has a shape factor δ^*/θ_0 of approximately 1.9, indicating a turbulent or at least highly transitional profile. This data has been verified using both a boundary layer and hot wire probe. Boundary layer characterization data for the two probes agree within 15%. Discrepancies are attributed to uncertainty associated with equivalent positioning between the two measurements devices which is amplified by the thin boundary layer examined here (δ=1.3mm). Figure 29 shows the boundary layer velocity and turbulence intensity profile. The turbulence intensity increases from approximately 0.4% in the freestream to almost 4% in the boundary layer. Due to its small thickness, the boundary layer can only be resolved to approximately y/δ=0.1. It is perhaps more informative to examine the boundary layer velocity spectrum shown in Figure 30. This provides confidence that the boundary layer state is turbulent or at least highly transitional due to the development of a -5/3 slope across over more than one decade of frequency. A spectrum for the shear layer is also provided in which it is clear that no strong periodic behavior is present in the baseline condition. This ensures that any coherent motion (shown later) is produced by ns-DBD forcing rather than some natural oscillation in the baseline flow.
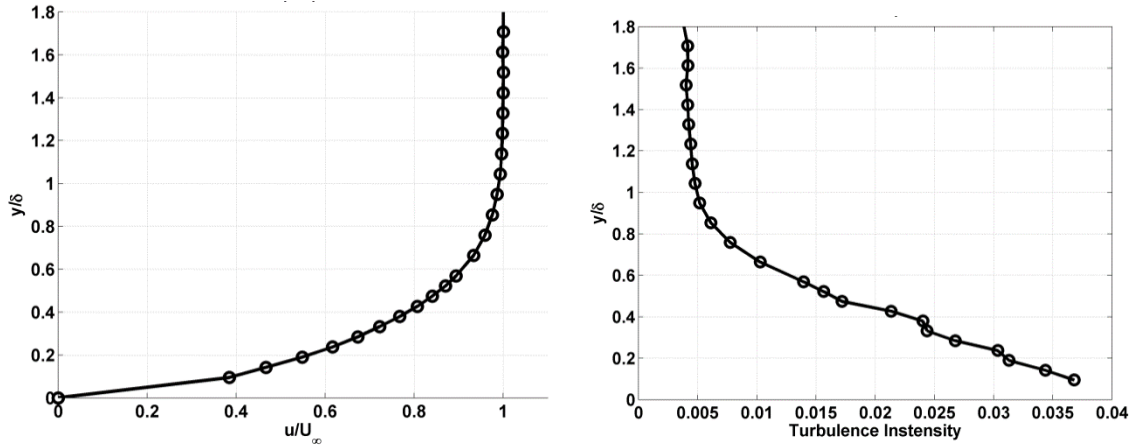
31

Figure 29: Boundary layer velocity profile and turbulence intensity for the BFS facility.
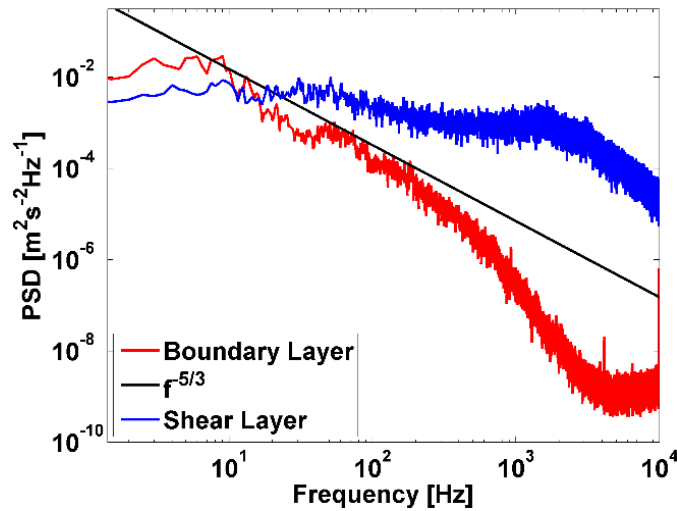

Figure 30: Velocity spectra in the boundary layer at (x/H=0, y/δ=0.2) and shear layer at (x/H=3, y/H=0).

Measurements at different spanwise locations, which are normally made to ensure that no 3D effects exist, have not been performed. However, since the boundary layer thickness on the floor is small, a small boundary layer on the tunnel walls is expected as well. The horizontal aspect ratio of the step (6.15:1) likely causes 3D reattachment effects, but seems to be negligible here as this investigation is focused on the shear layer close to the step. Note that the expansion ratio of the step is quite small (1.08) which ensures a negligible streamwise pressure gradient. Measurements are focused on the region near the step ($x/\theta_o<250$, $x/H<4.5$), where the shear layer instability is dominant, to ensure appropriate comparison with mixing layer results.

Ns-DBD actuators in the BFS facility are constructed of 3 layers of Kapton tape (0.15mm dielectric total) with 6.35mm wide HVE and 6.35mm wide GE. The spanwise length of the actuator is 40mm. A schematic is provided in Figure 31. A small recess is milled into the BFS trailing edge to accommodate DBD actuators with minimal disturbance to the incoming boundary layer. Electrical data for ns-DBD actuators applied to the BFS facility are provided in Figure 31. The peak voltage is approximately 8.6kV and the peak current is approximately 1.1A/cm. Pulse energy, which is the most representative parameter for ns-DBD, is approximately 0.33mJ/cm. This is substantially lower than the value reported in the mixing layer (see Figure 27a). It should be noted that the short actuator length requires much lower dc supply

32

voltage to generate similar per unit length pulse energy. Thus, the following tests do not represent the maximum available ns-DBD pulse amplitude that can be applied to the BFS.
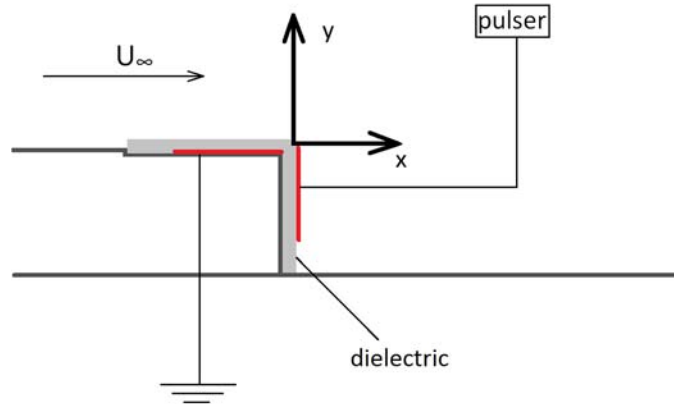

Figure 31: Schematic of ns-DBD installed on BFS. Note dielectric thickness is exaggerated.
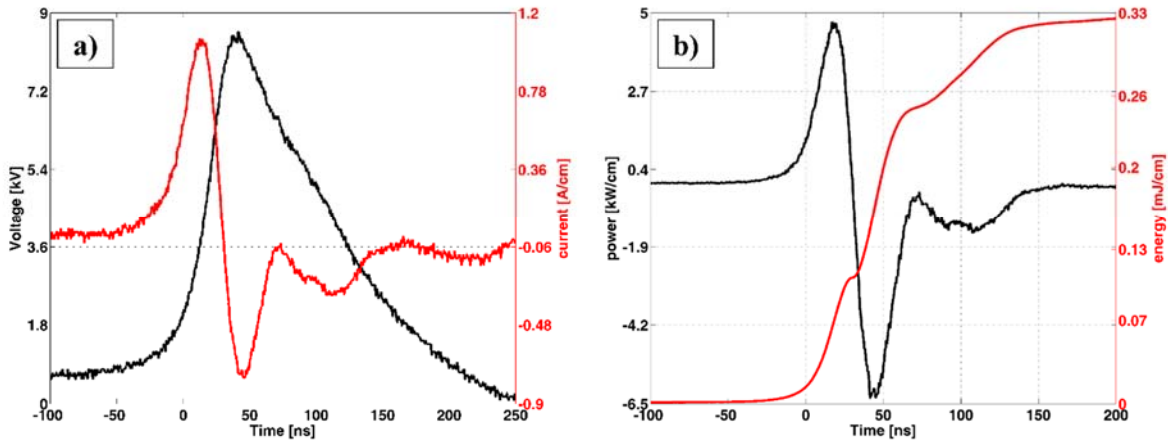

Figure 32: Measured voltage and current waveforms (a) and calculated power and energy values (b) for ns-DBD applied to BFS.

Preliminary measurements of the shear layer are acquired at $x \approx 167\theta_0$ ($x \approx 3H$) with a boundary layer probe. The device is not capable of resolving negative velocity close to the ground floor downstream of the step due to recirculation. Consequently, focus is placed on the low-speed side near the lowest y-location of positive velocity. This location is determined by initially placing the probe in the recirculating flow below the shear layer and iteratively moving the probe out of the reverse flow region by small increments and into the high-gradient region of the shear layer. Once in the shear layer, the velocity abruptly changes sign. This is then the final probe location for these preliminary measurements.

Similar to the mixing layer, these measurements are acquired to gain a first glimpse of ns-DBD control on the BFS with minimal experimental time and effort. Figure 33a shows a baseline shear layer profile and a profile with actuation at $St_{\theta_0} = 0.0146$ at the same location ($x \approx 167\theta_0$). It can be seen that measuring one y-location only is sufficient to prove whether or not a specific actuation has a substantial effect on the shear layer. Impacts of actuation on the velocity profile will be discussed in detail subsequently. The frequency sweep (Figure 33b) is taken at $y \approx -18\theta_0$, marked with an arrow in Figure 33a. It shows the relative change of velocity due to a specific actuation frequency. The range of actuation reaches from 100 to 5000Hz ($St_{\theta_0} = 0.0005 – 0.0243$). Baseline data, which do not correspond to the St_{θ_0} of actuation as it could be assumed

33

from the figure, are acquired in between different frequency measurements and serve as a chronological reference. Three peaks can clearly be identified at $St_{\theta o}$ numbers of 0.0049, 0.0078 and 0.0146, indicating an increase of velocity of $\Delta u/U_\infty \approx 0.116$, 0.140 and 0.151 respectively due to actuation. The two latter indicate the strongest effects that also seem to be apparent over a larger frequency range. It is suspected that $St_{\theta o} = 0.0146$ is near the fundamental frequency and the smaller frequencies are associated with the first and second sub-harmonic.
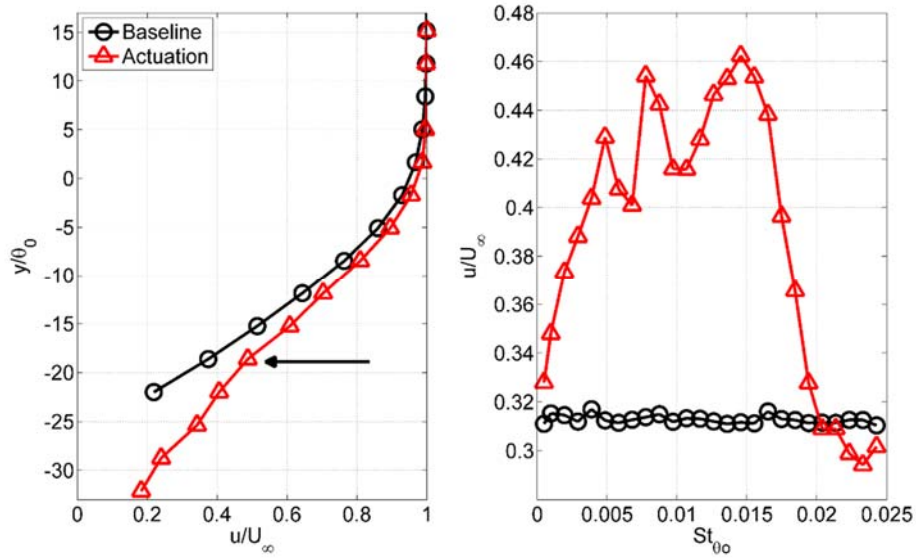

Figure 33: Shear layer profiles for baseline and forcing at 3000 Hz at $x \approx 167\theta_0$ (a) and frequency sweep at $y \approx -18\theta_0$ (b). E=0.33 mJ/cm.

Based on the frequency sweep, a series of PIV measurements is undertaken for the three peaks. Also, the case at a Strouhal number of $St_{\theta o} = 0.0243$ is examined. This is the corresponding frequency of 5000Hz that determines the upper limit of the pulser. Figure 34 shows shear layer profiles at a downstream location of $x \approx 164\theta_0$ for the different actuation frequencies and baseline. The fuller mean velocity profiles on the low-speed side of the shear layer are a direct indicator of control authority. This is, as will later be shown, a result of large-scale structures produced by ns-DBD that entrain freestream momentum into the low-speed region. This should also result in a shorter reattachment distance in comparison to the baseline, but this is not the focus of the current work.
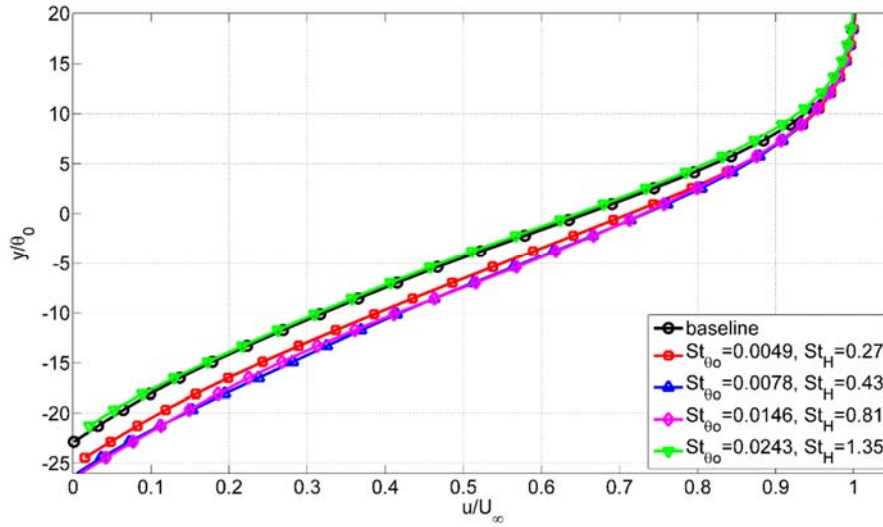
Figure 34: Shear layer profiles at x ≈ 1640₀ with and without forcing. E=0.33 mJ/cm.

As expected from the frequency sweep, the largest effect of actuation on the velocity profile is observed for 1600 and 3000Hz ($St_{\theta o}$ of 0.0078 and 0.0146) and a somewhat smaller effect for actuation at 1000Hz ($St_{\theta o}$ = 0.0049). Actuation at 5000Hz ($St_{\theta o}$ = 0.0243) does not result in a considerable alteration of the velocity profile. In general, the most drastic change in the profile is on the low-speed side which is in agreement with other BFS and mixing layer studies. At this particular measurement location, little change is observed along the high-speed side. Literature using other forcing methods suggests an effect should be observed on the high-speed side as well in some point of the domain (Chun and Sung 1996). It is unclear if this is a result of the forcing mechanism, amplitude or simply due to the available measurement domain. It can also be surmised that the reattachment distance is reduced since the profile is not only spreading but also bending towards the floor.

Integral calculations of the momentum thickness developing downstream of the step are shown in Figure 35. Results of ns-DBD forcing at 1600 and 3000Hz ($St_{\theta o}$ values of 0.0078 and 0.0146) are rather similar and indicate the largest effect of forcing for the varied parameters. The difference between the forcing cases and baseline is greatest at x ≈ 98θ₀, giving a value of $\Delta\theta \approx 0.9\theta_0$ for 3000Hz ($St_{\theta o}$ = 0.0146) forcing, decreasing with increasing downstream distance to values of approximately $0.49\theta_0 < \Delta\theta < 0.66\theta_0$. Actuation influences the shear layer momentum thickness growth especially in the near field ($66\theta_0 < x/\theta_0 < 118\theta_0$). The growth rate relaxes and mirrors the baseline farther downstream. This behavior is different from findings of forced free shear layers since the reattachment characteristics prevent the development of discrete vortices associated with Region II. Both laser reflections and PIV spatial resolution limited interpretation of data very near the step.
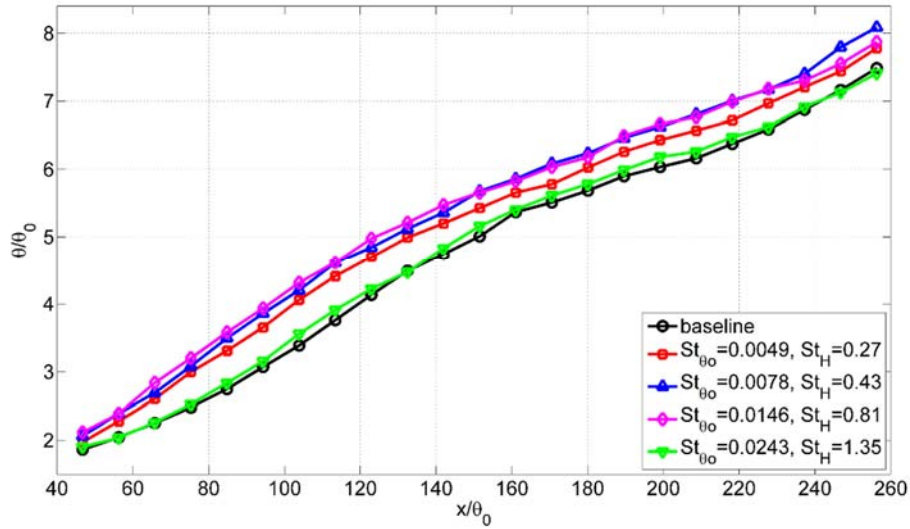
35

Figure 35: Momentum thicknesses as a function of distance from the step. E=0.33 mJ/cm.

Phase-averaged PIV images for the fluctuating v-component of the velocity are shown in Figure 36 for all four forcing frequencies. Organized clockwise rotating structures, excited by ns-DBD pulses at the corresponding frequency, are indicated by a pair of positive and negative spots. These are clearly observed for 1000, 1600 and 3000Hz actuation frequencies ($St_{\theta o}$ = 0.0049, 0.0078 and 0.0146 respectively). A difference between these vortex structures is difficult to see between 1000 and 1600Hz, but there is an obvious change for 3000Hz (Figure 36c). The size of these structures grows with increasing distance from the step as expected and the tendency for organized motions to dissipate appears to move upstream as the forcing frequency increases. For example, the organized nature of the 3000Hz case diminishes substantially by $x \approx 164\theta_0$. One can see from Figure 36c that this effect is much more dramatic for the 3000Hz case than for the 1000 and 1600Hz cases. One may also observe an overall diminishing of the counter-fluctuating v' distributions as compared to the 1000 and 1600Hz cases. Additional analysis is required to quantify these dynamics in more detail. For example, one also expects to observe some level of vortex merging that is not obvious here. As expected from the velocity distributions in the shear layer, no obvious structures can be observed for the 5000Hz ($St_{\theta o}$ = 0.0243) actuation case since it is outside the range of naturally amplified frequencies. This data, along with a lack of coherent motion in the baseline case (see Figure 30), confirms the existence of large-scale structures produced by ns-DBD thermal perturbations. The existence of a turbulent or highly transitional boundary layer separating from the step indicates that ns-DBDs and the thermal mechanism in general is not reliant on initially laminar boundary/shear layer conditions. The organized motions present here are not unlike those observed in airfoil separation control studies (Rethmel et al. 2011; Little et al. 2012).
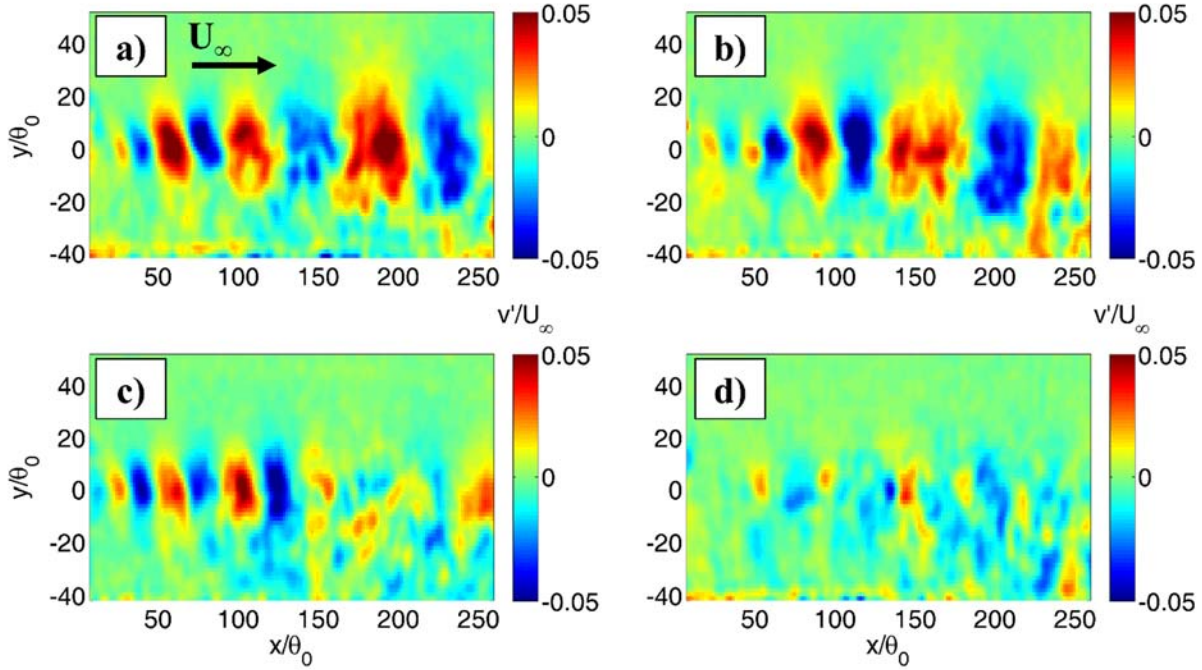
36

Figure 36: Phase-locked v-fluctuations at phase 0 for $St_{\theta o} = 0.0049$ (a), $St_{\theta o} = 0.0078$ (b), $St_{\theta o} = 0.0146$ (c) and $St_{\theta o} = 0.0243$ (d). E=0.33 mJ/cm.

As a final point of analysis, cross-stream distributions of dimensionless turbulent kinetic energy (TKE) and Reynolds shear stress are shown in Figure 37 and Figure 38 at $x = 164\theta_0$. Compared to the 1000, 1600 and 3000Hz ($St_{\theta o} = 0.0049$, 0.0078 and 0.0146 respectively) forcing cases, the baseline profile is characterized by a narrow peak at the step height, which is widened, slightly shifted downward and increased by approximately 40% for the 3000Hz case. Although the momentum thickness between the 1000 and 1600Hz actuation cases differ by about $\Delta\theta \approx 0.26\theta_0$, the TKE distribution is quite similar. It can be seen that all forcing cases result in additional TKE even if this does not produce substantial mixing layer growth in the mean (e.g. 5000Hz forcing). The TKE results generally mirror the mean flow data in that 3000Hz produces the greatest change followed by a group at 1600Hz and 1000Hz and finally by the high frequency case. The Reynolds shear stress behaves similarly. Note that the sign of the shear stress is consistent throughout indicating that the mean flow is feeding energy to the turbulence throughout the entire cross-stream domain. Region II, which is observed in highly excited free shear layers and characterized by a change in the sign of the Reynolds shear stress, is not observed here. This is expected since a clear rollup of instability waves into discrete vortices is prevented by reattachment to and presence of the wall.
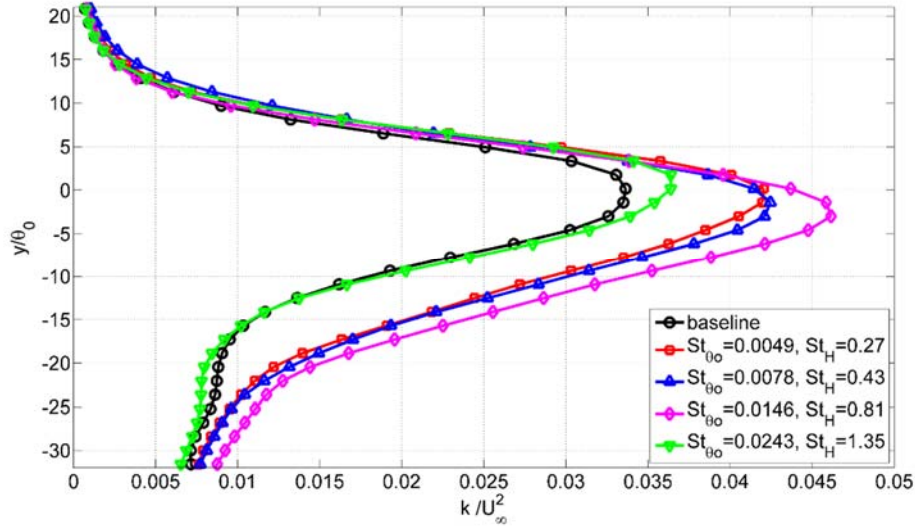
Figure 37: Cross-stream distributions of dimensionless turbulent kinetic energy at x = 164θ_0. E=0.33 mJ/cm.
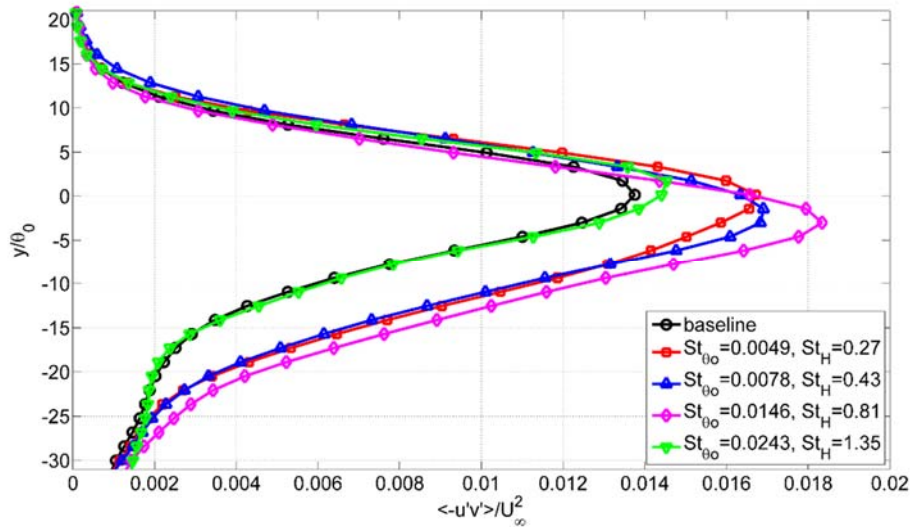

Figure 38: Cross-stream distributions of dimensionless Reynolds shear stress at x = 164θ_0. E=0.33 mJ/cm.

The previous results show that control authority has been established on initially turbulent shear layers using ns-DBD plasma. This suggests that initial shear layer thickness (not state) is the primarily metric by which possible control efficacy should be judged. This points to the possibility of scaling arguments analogous to momentum coefficient for thermoacoustic perturbations which should include some measure of initial boundary/shear layer thickness relative to pulse energy. Additional discussion along these lines will be provided, but the effects of pulse energy are now explored on the BFS. Recall from mixing layer results that a slight stabilization was observed for cases even in the range of most amplified frequencies. This points to a possible competition between the perturbation and heating effects where the latter has been shown to decrease the growth of mixing layers in reacting flows (McMurtry et al. 1986; Hermanson et al. 1987; Hermanson and Dimotakis 1989).

A first glance into the influence of pulse energy on control authority is apparent from frequency sweeps using a pitot probe at one location on the low-speed side of the shear layer, similar to Figure 33. Figure 39

38

shows data for various energy values ranging from 0.11-1.00 mJ/cm. Note that peaks in the frequency sweep correspond to instances of greatest control authority which is connected to increases in mixing of momentum from the high-speed freestream. Two observations are apparent from this data. First, similar peaks are observed over a range of pulse amplitudes indicating the natural dynamics of the BFS shear layer are excited and consistent. Second, the control authority does not monotonically increase with pulse energy. Rather, a preference for moderate energy values around 0.24-0.34 mJ/cm is apparent. Note that values in this amplitude range (0.33 mJ/cm) were employed for the previously discussed BFS data. The effects of pulse energy at a single frequency (1000 Hz or St_θ=0.005) are now considered in detail. The excitation frequency is chosen in order to maximize the lifetime of the DBD. Higher frequencies have shown greater control authority (e.g. 3000 Hz or $St_{\theta o}$ = 0.0146), but at the expense of earlier dielectric failure.
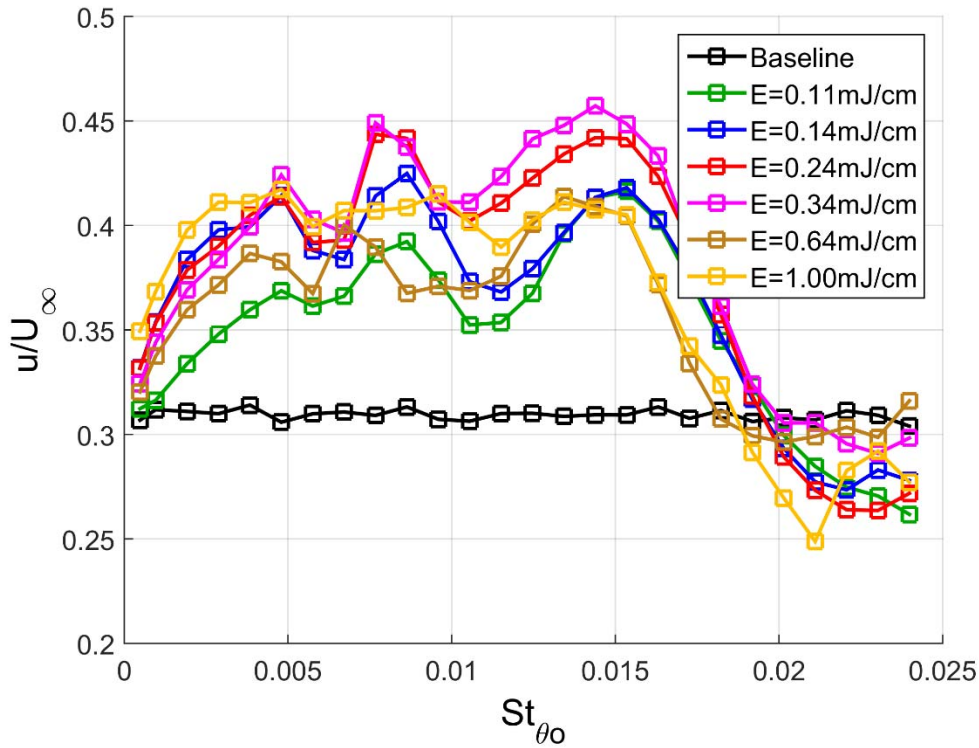

Figure 39: BFS frequency sweeps for various pulse amplitudes

Electrical traces for four pulse amplitudes are shown below in Figure 40 with corresponding details in Table 3. Note that the pulse amplitude is increasing from bottom to top, as can be seen by the trend of rising peak values. Peak current, peak voltage, peak power and gross energy over the time duration of one pulse are summarized in Table 3. As can be noted from the electrical data, the gross energy per pulse increases by at least 150% of the prior value for each DC power supply adjustment. As a reminder, note that instantaneous power is simply the product of instantaneous current and voltage and that gross energy is then computed from the time-integration of the instantaneous power curve over the duration of one pulse. The absolute value of the current / voltage product is used in the integration where the product is otherwise negative (i.e. alternating current / voltage sign near end of pulse), as it assumed that there is still a localized heating effect induced from the discharge regardless the direction of instantaneous net electrical charge transfer (Dawson and Little 2014).
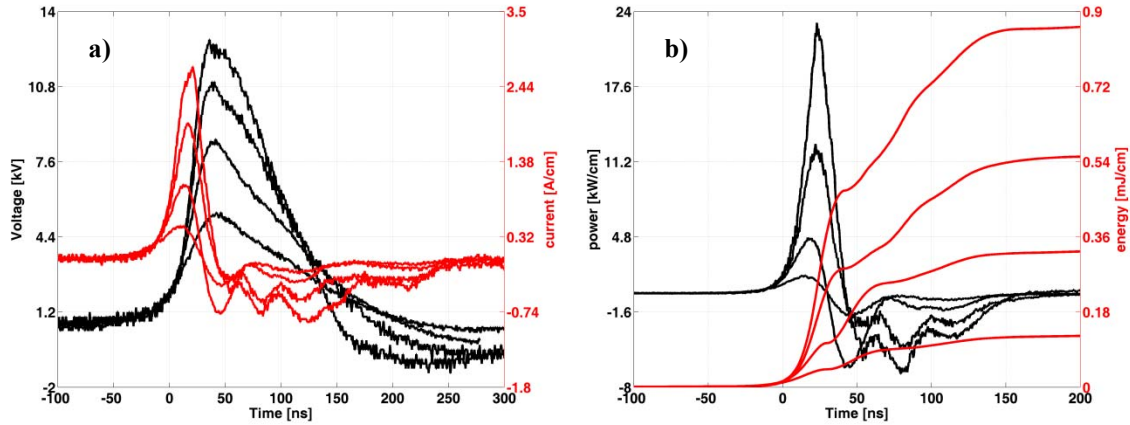
Figure 40: Measured voltage and current waveforms (left) and calculated power and energy values (right) for ns-DBD applied to BFS. Pulse amplitude increasing from top to bottom.

Table 3: Peak voltage, current, power and gross energy values for variable pulse amplitudes. Pulse amplitude increasing from top to bottom.

DC [V]	Peak Voltage [kV]	Peak Current [A/cm]	Peak Power [kW/cm]	Gross Energy [mJ/cm]
400	5.44	0.48	1.54	0.13
500	8.56	1.06	4.74	0.33
600	11.00	1.92	12.73	0.56
670	12.80	2.72	23.04	0.88

Cross-stream distributions of dimensionless mean spanwise vorticity at a streamwise location of $x \approx 50.4\theta_0$ for all four pulse amplitudes as well as a baseline case are shown in Figure 41. Note that the minus sign is withheld for simplicity of visual representation, as the sense of local rotation is actually negative with respect to a right-handed coordinate system. One can observe increases in shear layer growth as compared to baseline by noting reductions in mean vorticity, an indication of shear layer relaxation. Based on Figure 41, a 0.13 mJ/cm pulse amplitude results in a very weak excitation of the shear layer, which is nearly indiscernible from the baseline distribution. This is perhaps expected in light of the electrical characterization shown above for this particular pulse amplitude. A higher pulse amplitude of 0.33mJ/cm results in a substantial reduction of mean vorticity, as the peak value is reduced by approximately 18% of the initial (baseline) value. A similar observation is noted for the 0.56mJ/cm pulse amplitude, despite the sizable increase in pulse amplitude. Interestingly, upon further increase in pulse amplitude to 0.88mJ/cm, a considerable degradation in control authority is witnessed by the (relative) increase in peak vorticity. For this case, the net reduction in peak vorticity is only roughly 13% of the baseline value. It is noted here and throughout, that profile trends are reasonably consistent with that of various adjacent streamwise locations.
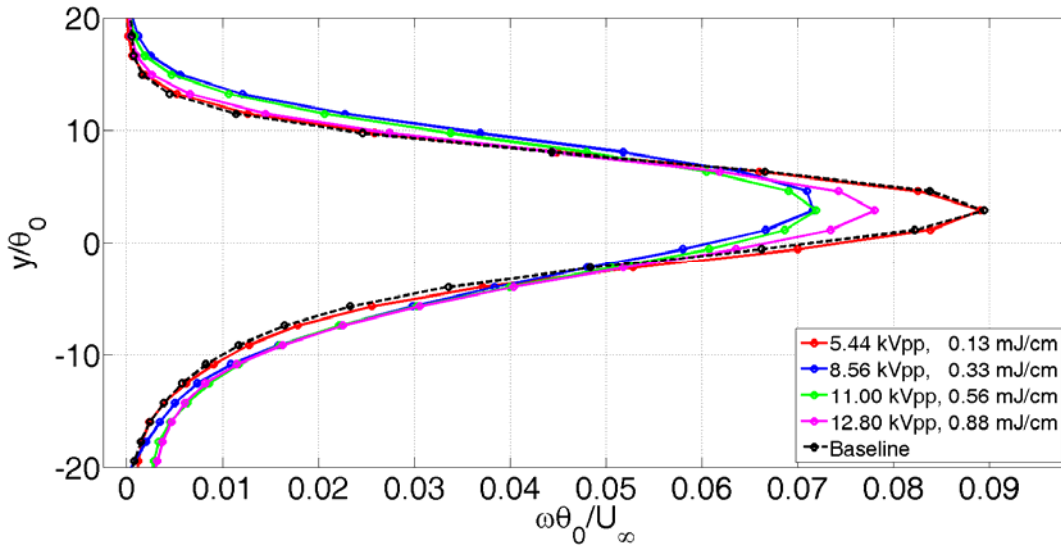
40

Figure 41: Cross-stream distribution of dimensionless mean vorticity at streamwise location $x/\theta_0 \approx$ 50.4. $St_{\theta o} = 0.005$

The momentum thickness in the BFS shear layer is calculated with the bounds of integration limited over the portion of the cross-stream domain for which $u \geq 0$. The purpose of this constraint on the cross-stream domain is to exclude the highly turbulent, reverse flow which is present within the separation bubble below the shear layer itself. The flow in this region is largely influenced by the presence of the wall, as well as by the downstream shear layer reattachment, splitting and subsequent upstream deflection, thus is not quantitatively indicative of the initial shear layer excitation and resulting growth. The momentum thickness as a function of streamwise position (x) is shown in Figure 42. Because the momentum thickness is an integral measure of the local velocity distribution, Figure 42 is more representative of the flow throughout the entire domain of interest. This study is concerned mainly with the initial growth of the excited shear layer, as non-linear effects are likely to ensue downstream clouding interpretation. The presence of and reattachment to the wall also create additional complications that the authors do not wish to presently examine.
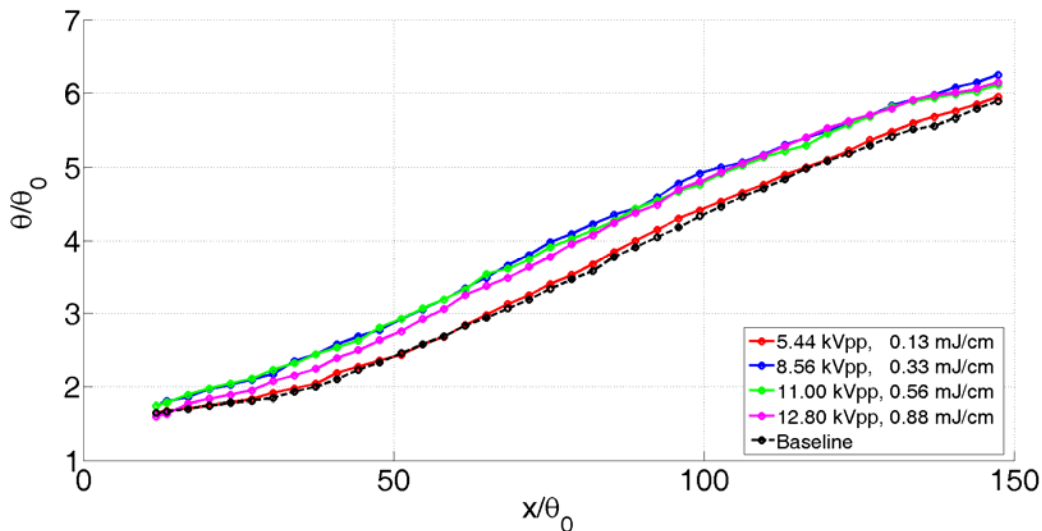

Figure 42: Streamwise dimensionless momentum thickness growth when at $St_{\theta o} = 0.005$ and variable amplitude.

41

From Figure 42, behavior regarding the streamwise growth is obtained for the various pulse amplitudes. It can be immediately noted that the 0.13 mJ/cm amplitude has a very minor effect throughout the entire streamwise domain. Alternatively, one can also notice the pronounced effect the 0.33mJ/cm and 0.56mJ/cm amplitudes both have on the local momentum thickness. It seems of little benefit to closely examine the differences between these two cases, as it appears minor. However, a measurable reduction can be seen for the 0.88mJ/cm amplitude case throughout roughly half of the domain. On average there is roughly a $0.5\theta_0$ increase for the two intermediate amplitudes compared to baseline, whereas there is only an increase of approximately $0.25\theta_0$ compared to baseline for the highest amplitude case within the range of roughly $25\theta_0$ $< x < 75\theta_0$, after which the high amplitude curve merges with that of the two intermediate amplitudes. There is little deviation from baseline behavior for the weakest amplitude (0.13mJ/cm) at any point in the domain. The upstream trends noted are fairly consistent with vorticity distributions at $x \approx 50.4\theta_0$. Namely, the degradation in control authority above a certain amplitude (apparently 0.56mJ/cm in this case). It seems as though the two intermediate amplitudes serve as a limit beyond which considerable control authority is not expected. The attainment of this amplitude threshold was one of the main objectives of this particular test.

An additional quantity of interest is the turbulent kinetic energy. An initially turbulent shear layer tends to accompany a positive turbulence production due to mixing and transition to smaller scales (Vukasinovic et al. 2010). Thus, the development of TKE is indicative of shear layer growth / dynamics. Figure 43 shows the cross-stream distribution of dimensionless TKE at the streamwise location $x \approx 50.4\theta_0$. Again, little effect is observed for the lowest pulse amplitude as compared to baseline, and considerable effects are seen for the two intermediate pulse amplitudes. However, unlike the streamwise vorticity (Figure 41), the overall distribution of TKE for the 0.33mJ/cm pulse appears to be slightly broader than and exhibits a larger peak value in comparison to the higher 0.56mJ/cm amplitude, though the differences are modest at best. The peak values for the 0.33mJ/cm and 0.56mJ/cm are approximately 28% and 21% of the baseline peak value, respectively, whereas that of the 0.88mJ/cm amplitude is only approximately 14% of the baseline peak value. It can also be noticed that the TKE profile for 0.88mJ/cm is slightly asymmetric with respect to the 0.33mJ/cm and 0.56mJ/cm TKE distributions, although this is likely just a consequence of the limited spatial resolution.
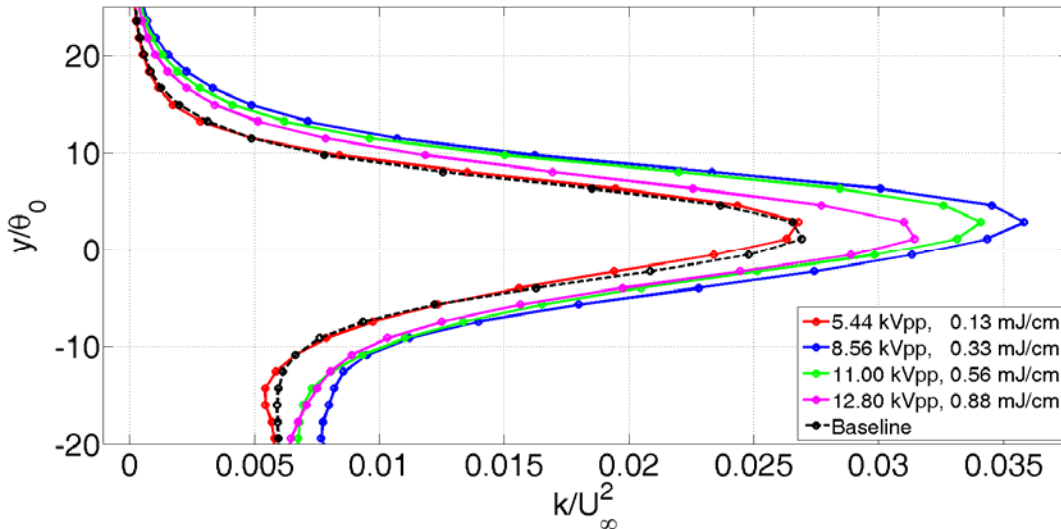

Figure 43: Cross-stream distribution of dimensionless mean turbulent kinetic energy (TKE) profiles at streamwise location $x/\theta_0 \approx 50.4$. $St_{\theta_o} = 0.005$

42

In order to obtain a more representative estimate of ns-DBD actuation on TKE distribution and development, a cross-stream integration was performed at each streamwise location according to the expression:

$$\frac{1}{\theta_0 U_\infty{}^2} \int_y k\, dy$$

where integrations are performed across the entire available domain and are a representative value of the total TKE at a particular location in the shear layer. This cumulative result is summarized in Figure 44 for all four pulse amplitudes. The behavior is strikingly similar to that of previously discussed profiles in several ways. A minimal change is observed on the net TKE distribution across the entire domain for the 0.13mJ/cm amplitude forcing. An appreciable effect is noted for both the 0.33mJ/cm and 0.56mJ/cm amplitudes while a modest change occurs for the 0.88mJ/cm pulse case, at least in the far upstream region (i.e. $x \leq 45\theta_0$). Beyond this point, the TKE integration curve corresponding to the high amplitude (0.88mJ/cm) pulse merges with the 0.56mJ/cm case over approximately $40\theta_0$. However, the highest amplitude pulse (0.88mJ/cm) results in a reduced net distribution of TKE as compared to both the 0.56mJ/cm and 0.33mJ/cm pulse amplitude forcing despite being clearly the 'strongest' perturbation. Finally, and perhaps most notable from this figure in contrast to others, the 0.33mJ/cm amplitude clearly dominates the TKE distribution throughout the entire streamwise domain. This is obviously the case at $x = 50.4\theta_0$ as seen by Figure 43. Considering that this is only the second highest of the four amplitudes employed, this points towards an optimal relationship for the overall excitation of dynamical behavior between this particular pulse amplitude, actuator geometry and the given initial shear layer conditions.
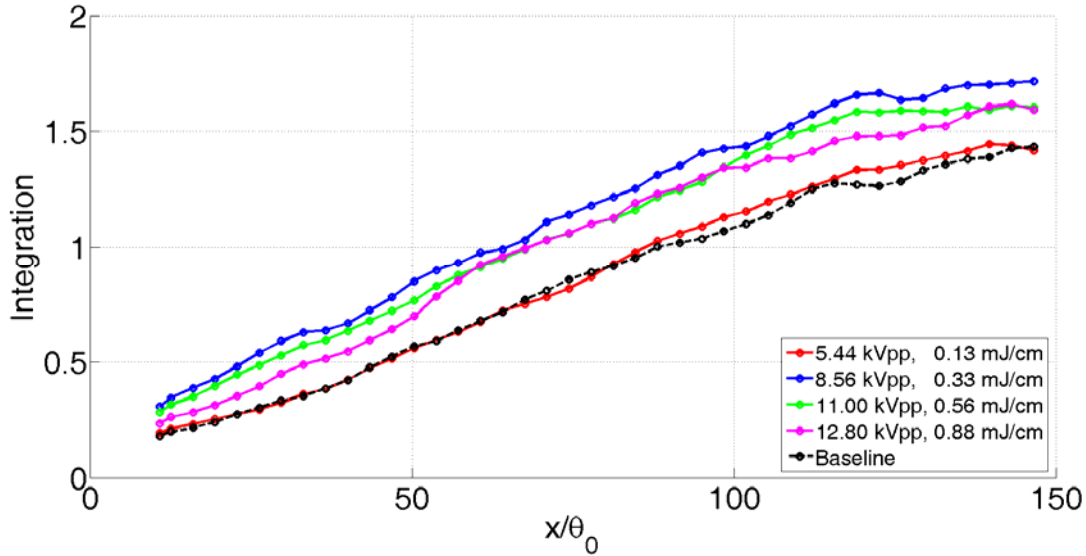

Figure 44: TKE cross-stream integration vs streamwise position. $St_{\theta_o} = 0.005$

For completeness, Figure 45 shows the cross-stream distribution of Reynolds shear stress for each pulse amplitude at a common streamwise location of $x \approx 50.4\theta_0$. Reynolds shear stress distributions for each pulse amplitude exhibit qualitatively similar behavior as the TKE profiles, including the slightly asymmetric distribution for the highest pulse amplitude (0.88mJ/cm). The sign of the shear stress is notably consistent throughout, indicating a transfer of energy from the mean flow to turbulent fluctuations in the entire cross-stream domain as expected.
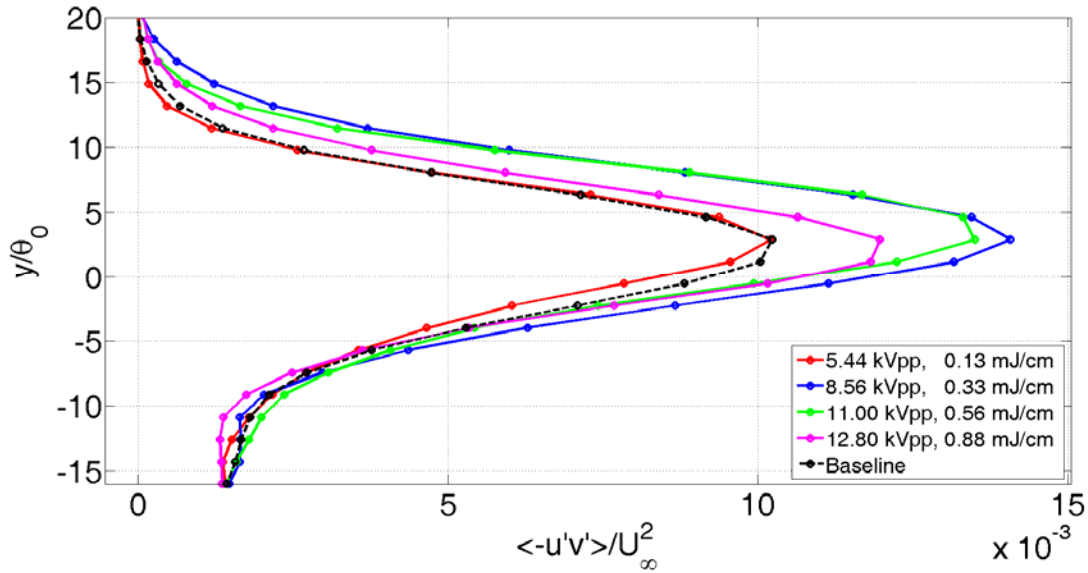
43

Figure 45: Cross-stream distributions of dimensionless Reynolds shear stress at streamwise location $x/\theta_0 \approx 50.4$. $St_{\theta o} = 0.005$

Finally, Figure 46 shows phase-averaged v-fluctuations. The presence of adjacent positive/negative regions in Figure 46 indicate the presence of discrete vortex structures which are a result of roll-up of the ns-DBD induced instability wave. These vortex structures convect downstream within the shear layer. No obvious signs of vortex merging are observed likely due to the influence of the wall. Figure 46 provides a qualitative idea of the extent of which coherent dynamics are excited within the shear layer as opposed to the mean flow and turbulence modifications in prior figures. The pulse amplitude is increasing from (a) – (d) in Figure 46. Little, if any coherent dynamics can be observed for the 0.13mJ/cm pulse amplitude (Figure 46a), whereas a coherent vortex train is seen to persist across the entire streamwise domain for the 0.33mJ/cm case (Figure 46b). These vortices are reasonably consistent in size and organized nature. The 0.56mJ/cm pulse amplitude (Figure 46c) seems to produce coherent vortices which grow in size until approximately $x \approx 100 \, \theta_0$, after which they appear to begin to dissipate. Little evidence of any remaining coherence can be seen beyond $x \geq 150\theta_0$. The high amplitude 0.88mJ/cm pulse appears to result in more coherent dynamics than the 0.13mJ/cm case, but still less than the 0.33mJ/cm and 0.56mJ/cm cases, which is perhaps expected. It appears that coherent vortices can somewhat persist across the entire domain for this amplitude, unlike the 0.56mJ/cm case. However, there is either a rapid dissipation of some of these vortices as evidenced by Figure 46d within the approximate range $60\theta_0 < x < 160\theta_0$, or the disturbance simply does not excite the instability wave such that it produces a consistent vortex train. Either one is a testament to the lack of coherent dynamics excited by ns-DBD discharges in comparison with the two more favorable pulse amplitudes (Figure 46 b & c). Other phases have been acquired and their behavior is similar to that presented here.
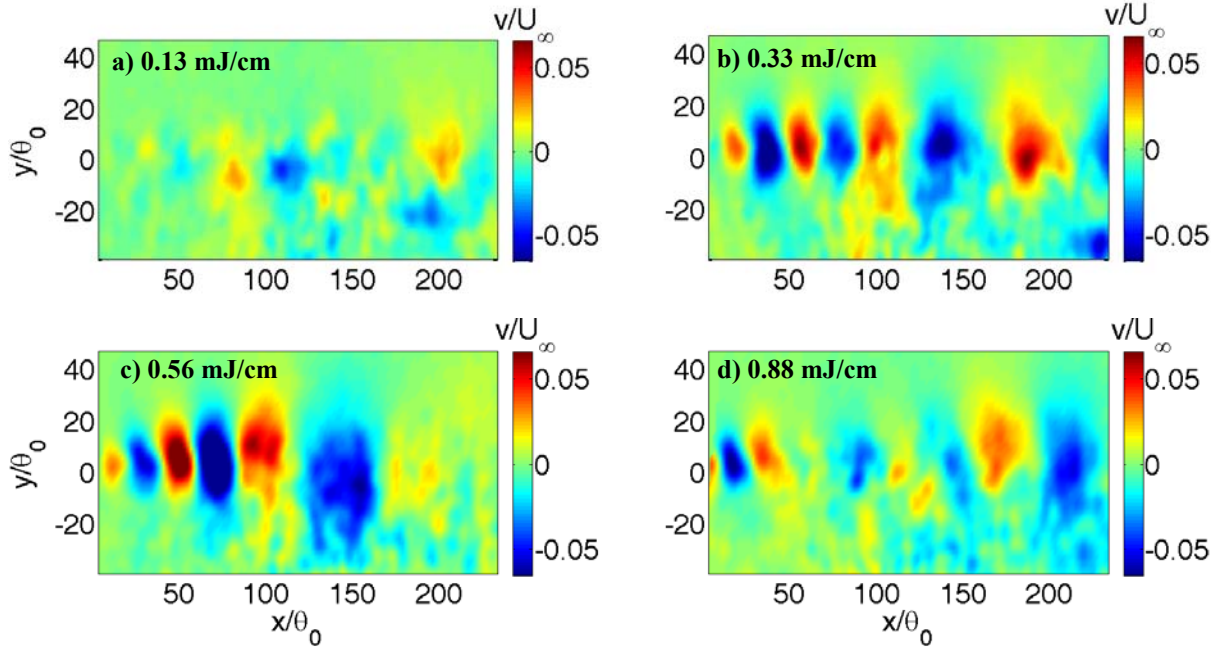
Figure 46: Phase-averaged normal velocity fluctuations. $St_{\theta o} = 0.005$

As a final measure of amplitude characterization, long exposure images of the ns-DBD plasma discharge are shown in Figure 47 at 1000 Hz. The pulse amplitude is increasing from top to bottom such that the reader may consistently see in Table 3. As can be seen by the relative intensities of the plasma discharges, there are some notable differences in characteristics. For example, the 0.13mJ/cm (lowest amplitude) seems to generate relatively weak plasma as shown by the lowest intensity and longest exposure time. The plasma consists of small scale, non-uniformly spaced, discrete filamentary structures which are not unlike those observed in ac-DBDs (Gibalov and Pietsch 2000; Corke et al. 2010). There is a noticeable improvement in spanwise uniformity of the plasma when the gross energy is increased to 0.33mJ/cm. One can also detect the onset of larger-scale filamentary structures. Upon increasing the amplitude further (Table 3c), there is a development of these large-scale discrete plasma filaments, as well as the overall glowing of the discharge. These visual characteristics seem to be in reasonable accordance with the characterization shown in Figure 40 and Table 3. At this time, it is an open question as to whether the reduced BFS control authority at high energy is a result of thermal stabilization (similar to the mixing layer results discussed previously) or a consequence of increased three-dimensionality of the plasma. Additional schlieren imaging is required to answer this question, but the former seems plausible given its occurrence in two different flow systems.
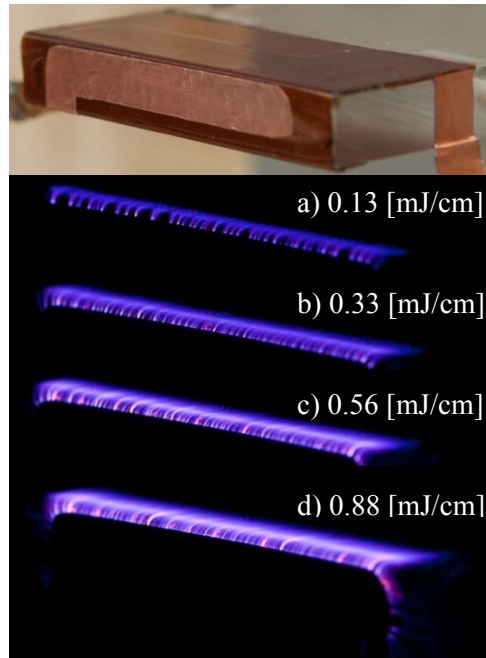
45

Figure 47: Long exposure plasma images at variable pulse amplitudes, with increasing pulse amplitude from top to bottom. Discharge shown for 1000 Hz pulsing frequency.

C. Femtosecond Laser Energy Deposition on the BFS

Preliminary studies of femtosecond (fs) laser energy deposition have been performed on the BFS in collaboration with PM&AM Research, LLC. The fs laser is used to excite the BFS shear layer just downstream of the step. The nature of fs lasers is such that self-focusing results in ionization. This allows exploration of off-body energy deposition. For example, one may deposit energy at various locations along the boundary or shear layer profile to examine its influence on control authority. In this preliminary work, only one location very near the step corner is examined. The total pressure in the shear layer is acquired using a boundary layer probe and 10 Torr MKS Baratron pressure transducer. A motorized single axis traverse is employed to generate shear layer profiles. Two access holes are drilled in the tunnel sidewalls to provide a path for laser beam. The holes were covered with 1mil Kapton tape and the laser was allowed to burn its own path to prevent contamination of the experiment by the holes. In general, the use of a blow down facility is beneficial here since test section pressure exceeds atmosphere.

Only certain discrete frequencies can be employed due to nature of the fs laser. In this work, measurements are acquired at 1kHz and 5 kHz for lens focal lengths of 30cm and 50cm respectively. The frequency and focal length combinations resulted in a spanwise plasma distribution of roughly 2cm and 3.5cm respectively. The laser was positioned at close as possible to the step corner and centered along the test section span (Figure 48).
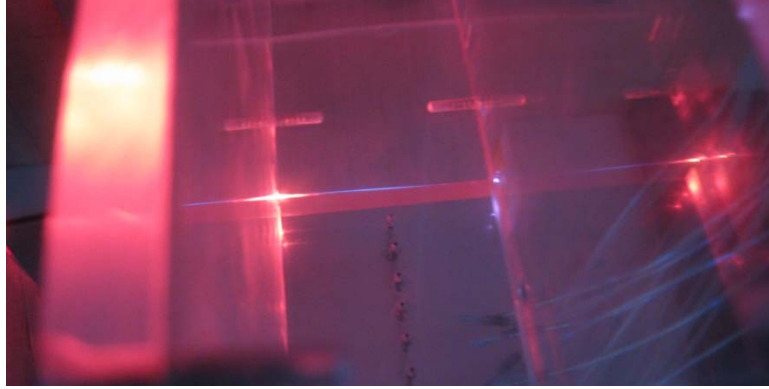
Figure 48: Location of laser energy deposition for 1kHz and 30cm focal length. Spanwise length of the ionized region is approximately 2cm.

The effect of fs laser energy deposition on the shear layer velocity profile at $x/\theta_o=167$ ($x/H=3$) is shown in Figure 49. The measurement uncertainty is smaller than the symbol size. The profiles do not extend to the wind tunnel floor since a recirculating flow is present in this region thus nullifying the probe results here. The effect of frequency is clear especially near the low speed side. Forcing at $St_\theta=0.024$ produces a stabilization of the shear layer in that mixing between the high and low speed sides decreases. Forcing at $St_\theta=0.005$ produces an increase the growth of the shear layer as now more momentum is present on the low speed side due to freestream entrainment, presumably due to the formation of large-scale structures. The findings are generally consistent with other methods for exciting (or suppressing) shear layer growth although the exact physical mechanism, especially in the high frequency case, is not clear. The slight stabilization at high frequency is consistent with ns-DBD plasma results, but the overall flow control effect is modest in comparison to studies with other types of actuation in the literature. Regardless, the preliminary data shown here is evidence of potential and should be explored in the future.
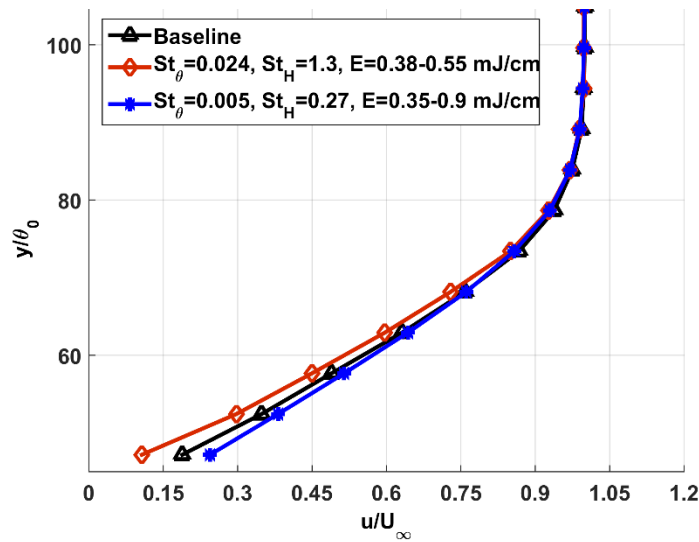

Figure 49: Shear layer velocity profiles at $x/\theta_o=167$ ($x/H=3$) with and without fs laser energy deposition.

A complicating factor in this preliminary study is the uncertainty associated with the amplitude of the laser perturbation. It is quite simple to measure the energy that goes into the discharge using a laser power meter before and after the ionized region. However, the distribution of plasma is not uniform nor does it span the entire test section (e.g. Figure 48). Because of the length uncertainty, a range of energies is reported in the legend of Figure 49. The range is calculated using the measured energy along with the *observed* and

47

assumed full span plasma length. For example, the St_θ=0.024 case uses a spanwise length of 3.5cm (observed) to 5cm (full-span) to estimate the energy per unit length. It should also be noted that the amplitude of forcing plays a large role in the shear layer response. Variation of forcing amplitude can change the shear layer response (excite or suppress) even at a fixed frequency as seen in ns-DBD plasma BFS results. Regardless, the preliminary experiments reported here indicate that femtosecond laser energy deposition has potential for excitation or suppression of shear layer growth. Practical implications of a mature technology are widespread since shear flows are present throughout aerodynamics and off body excitation could be useful in some situations. The true utility of lasers for active control of shear flows lies in their ability to vary the location of energy deposition relative to the boundary/shear layer profile. This has not been evaluated in the research community and supporting theoretical calculations would be beneficial both in practice and as a model for thermal perturbations in general.

D. The Mixing Layer Revisited
Nd:YAG Laser Energy Deposition

Additional exploration of laser energy deposition for control of turbulent shear flows has been performed on the original mixing layer facility. These preliminary experiments (and a portion of the proposed work in general) were motivated by Nd:YAG laser energy deposition for exciting supersonic cavity flows (Lazar et al. 2008) under the general hypothesis that both laser and ns-DBD plasma mechanisms are primarily thermal in nature. During the course of this investigation, it was found that ablation of the metal substrate was crucial for realizing control authority. Aluminum was employed as the splitter plate material in all cases. A first check of the amplitude of laser energy deposition was performed using schlieren imaging in quiescent air. A 350 mJ (max) Nd:YAG laser was focused by a 200mm spherical lens and formed into a line by a -12.7mm cylindrical lens. The length of the resulting laser ablation line was approximately 12.7cm. The compression waves produced by the laser line were compared to compression waves from ns-DBD plasma having length of 6.8cm and maximum possible amplitude (1.4 mJ/cm). The wave strength measurement was chosen since it is not clear how much energy is deposited as heat for either laser or ns-DBD plasma excitation. Note that the literature shows are large uncertainty on how much electrical energy is actually coupled to the flow as heat for ns-DBD plasmas (typically 30-70%). The ablation process (in terms of energy coupling as heat) is even less understood. Consequently, a comparison based solely on energy is not useful at this stage.

The compression wave strength comparison was performed on an identical optical assembly. Schlieren imaging is inherently qualitative, but this arrangement ensures that a relative comparison between the laser and plasma can be performed. The salient features of laser energy deposition are shown in Figure 50a. Both a compression wave and localized hot spot (radius of ~1mm) are visible. Note that the schlieren axis is slightly misaligned in the provided image hence the wave appears thicker in some regions. The schlieren image in Figure 50a shares similar features as the ns-DBD plasma induced waves of Figure 6a. However, a marked difference is the presence of a clear hot spot in Figure 50a which is not captured in the ns-DBD case presumably because it is very small. The size of the hot spot may be crucial for characterizing the control authority of thermal perturbations.

A relative comparison between laser and plasma compression waves is shown in Figure 50b. Phase-locked images of the wave strength are acquired at different time delays after discharge initiation noted by the abscissa of Figure 50b. The wave strength (defined as the intensity difference between the compression and expansion waves (Dawson and Little 2013) has been normalized by the maximum observed for the ns-DBD plasma case. The laser-induced wave strength at short delay can exceed four times that of the ns-DBD case. The laser wave strength becomes substantially weaker as the wave moves away from the discharge, but in all cases is at least a factor of two greater than the plasma case. In fact, this value is even greater considering that the plasma actuator employed in the mixing layer is substantially weaker in energy (0.65 mJ/cm). The strength of the plasma-induced compression wave is linearly related to the measured electrical energy (Dawson and Little 2014). Based on this, we can extrapolate the electrical energy required to produce a similar wave strength for ns-DBD. Doing so for the highest normalized laser wave strength

suggests it is equivalent to an ns-DBD pulse of ~6mJ/cm which is well-beyond the pulse generator capability.
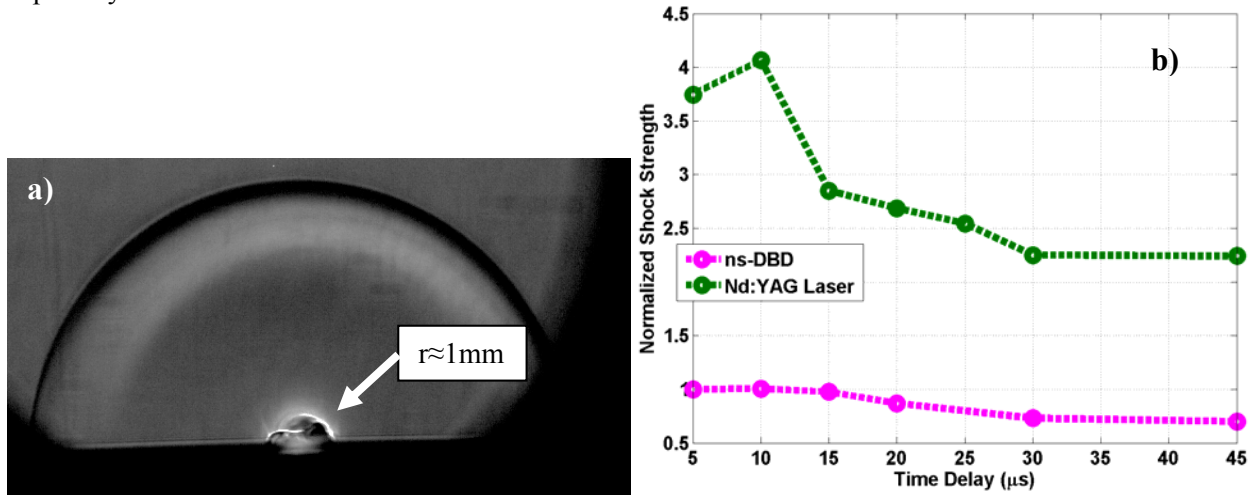

Figure 50: Schlieren image of Nd:YAG laser line incident on an aluminum plate showing low density region and compression wave (a) along with compression wave strength comparison between ns-DBD and Nd:YAG (b).

The efficacy of laser energy deposition for mixing layer excitation is tested in the same configuration as described in Section V.A (high-speed condition with no suction). A schematic of the experiment is shown in Figure 51. The optical setup is the same as the bench-top case. This results in an approximately 12.7cm ablation line which is centered along the splitter plate span on the high-speed side near the trailing edge. The laser energy is not sufficient to extend this line over the full-span of the facility thus a true comparison to the previous 2D ac and ns-DBD forcing is not possible. For consistency, the ns-DBD was tested at a similar line length and did not produce mixing layer growth as expected. The laser repetition rate (10 Hz) is not an impediment to control efficacy in this flow. The frequency of excitation for maximum growth at the end of the test section is 30 Hz (see Section VI.A). An excitation frequency of 10 Hz corresponds to maximum growth further downstream, but it should produce a measureable effect at the end of the test section if substantial control authority is achieved. A pitot-static probe is located at x=450mm and used to test the mixing layer response on the low-speed side (y=-25mm) as in previous exploratory tests.
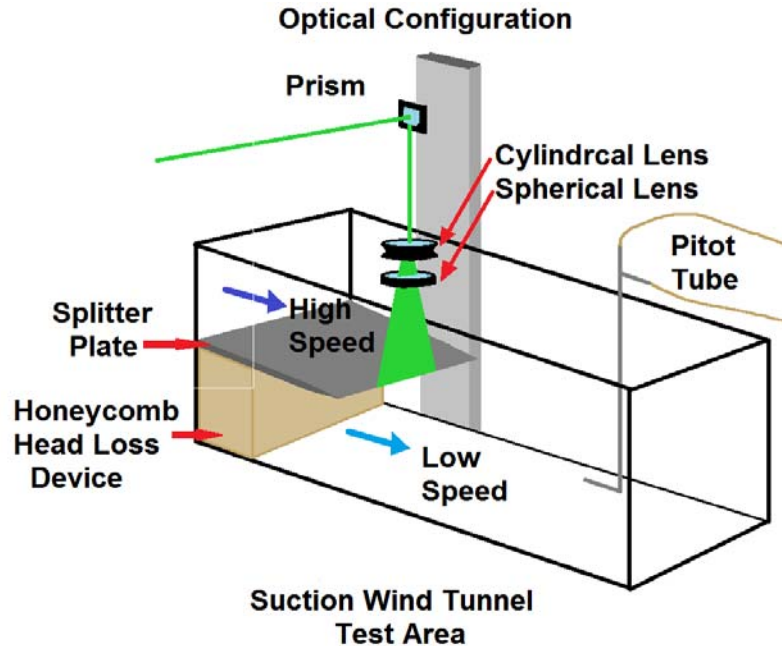
49

Figure 51: Schematic of Nd:YAG laser energy deposition for mixing layer excitation.

Figure 52 shows the response of the mixing layer to Nd:YAG laser energy deposition. The time trace in Figure 52a shows a baseline value in the first 10 seconds after which the laser energy deposition is initiated. Two incident laser locations are provided: 2mm and 10mm upstream of the trailing edge. The 2mm location shows the expected increase in dynamic pressure which is consistent with increased mixing between the high and low-speed streams. The perturbation at 10mm does not differ from the baseline behavior highlighting the localized effects of even such a strong thermal disturbance. Note that the 2mm location is close to the optimal shown in the ac-DBD forcing case. Velocity spectra in the mixing layer (Figure 52b) confirm that the flow is responding to the 10Hz laser disturbance as would be expected if control authority is achieved. Harmonics of the forcing frequency are also observed which are linked to an impulse-like response. The results shown here indicate that the low-speed mixing layer can be excited by energy deposition provided sufficient amplitude is provided. The required pulse energy to do so with ns-DBD plasma actuators is estimated at 6 mJ/cm. Again, this value is outside the capability of the existing pulse generator for this wind tunnel facility.
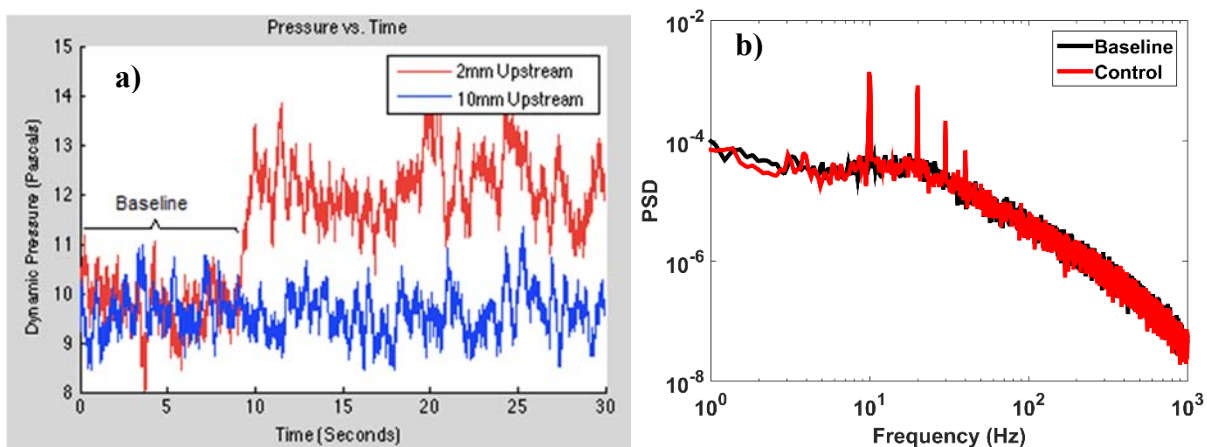

Figure 52: Response of mixing layer to Nd:YAG laser energy deposition at 10 Hz (St=0.01). Measurements are acquired 450 mm downstream of the splitter plate trailing edge at y=-0.25mm.

50

Clearly, Nd:YAG laser energy deposition is not a convenient way to excite low-speed mixing layers, but it does provide insight into scaling of thermal perturbations for control of turbulent shear flows. It is readily apparent that traditional amplitude measures (e.g. C_μ) must be re-cast for flow control using thermal perturbations to include some measure of energy relative to local boundary or shear layer thickness. At this stage, it is clear that thermal perturbations are better suited for control of high speed flows in which the boundary/shear layer in question is thin (~1mm) even if the exact scaling parameters are still unclear. It seems natural to focus future efforts on such scaling arguments and the fundamental mechanisms that result in excitation of such flows. More specific ideas for future work are provided in Section VIII.

Ns-DBD Plasma

The AFOSR Young Investigator Grant provided equipment funding for a higher energy and frequency pulse generator. The delivery period as well as initial characterization efforts were somewhat time-consuming thus only a short description of results is reported here. A more detailed presentation of this ongoing work is provided in Singh and Little (2016). The new pulse generator (Transient Plasma Systems, Inc) achieves more than double the pulse energy and triple the operation frequency compared to our existing unit. In the mixing layer facility, pulse energies of up to 2.5 mJ/cm with high frequency bursts of up to 9 kHz have been explored. Results indicate that single frequency operation at 2.5 mJ/cm and 30 Hz (corresponding to St=0.032 at the extent of the test section) is still insufficient to excite the turbulent mixing layer studied here. This is perhaps not surprising considering that Nd:YAG laser energy deposition suggests that 6 mJ/cm is sufficient if not absolutely necessary when forcing at St=0.01. More importantly, we now observe that control authority is achieved using burst mode forcing with a high carrier frequency (9 kHz) modulated at 30 Hz (St=0.032). It is even more interesting to note that this occurs for pulse energies of only 0.6 mJ/cm. Note that this forcing technique did not demonstrate an impulse-like behavior in contrast to the laser energy deposition case (Singh and Little 2016). Clearly, cumulative energy deposition or a convective behavior is playing a role and this should be considered in the future.
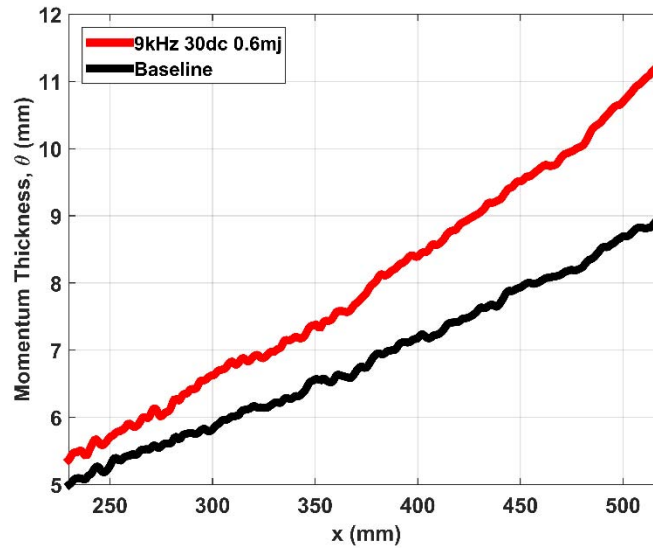

Figure 53: Mixing layer momentum thickness for baseline and ns-DBD forcing at 9kHz carrier frequency modulated at 30 Hz for 30% duty cycle. Pulse energy is 0.6 mJ/cm.

VII. Summary and Conclusions

The mechanisms responsible for high amplitude characteristics of thermal perturbations for aerodynamic flow control have been investigated experimentally. Two turbulent shear flows (mixing layer and backward-facing step) were examined using both plasma and laser-based thermal disturbances. Ac-

51

DBD plasma actuators were also employed to ground the work against a more well-known flow control actuation mechanism (momentum).

A turbulent mixing layer was created in a low-speed open return wind tunnel by adding a splitter plate and head loss device to the test section. Despite its somewhat unconventional nature, the baseline behavior of the mixing layer was in good agreement with established literature especially in cases where boundary layer suction was employed upstream of the splitter plate trailing edge. Hot wire anemometry near the end of the test section indicated a broad peak in the range of 10-30 Hz. When coupled with momentum thickness at the same location, this equated to St_θ near 0.032 (or the most amplified wave from linear stability theory) as expected (Ho and Huerre 1984). Momentum-based forcing using ac-DBD plasma at the splitter plate trailing edge confirmed this result as mixing layer momentum thickness was maximized using 30 Hz actuation at the location in question. PIV measurements showed that the structure of the excited mixing layer was in reasonable agreement with literature (including regions of negative turbulence production) although some discrepancies were observed that may be connected to the forcing nature or waveform. This is a subject of ongoing investigation with Dr. U. Kaul of NASA Ames. Similar results were also observed for forcing at 60 Hz which located the region of neutral stability approximately halfway down the test section. In this case, all three regions (I, II, III) of mixing layer growth as laid out in Oster and Wygnanski (1982) were observed. Variation of forcing amplitude allowed exploration of nonlinear behavior associated with the roll-up Kelvin-Helmholtz instability waves into discrete spanwise vortices. This was clearly observed for forcing at 60 Hz, but the test section length did not quite permit it at 30 Hz. While interesting from a fundamental perspective, exploration of the forced mixing layer in regions II and III is not the focus of this work. Instead, we chose from the onset to focus on the actuation mechanism that results in the initial growth of the mixing layer in region I as it is most applicable to AFC. All in all, baseline and forcing with ac-DBD plasma (momentum) confirmed that the behavior of our somewhat unconventional mixing layer is in agreement with established literature. It should be noted that the efficacy of ac-DBD plasma for controlling this turbulent mixing layer was largely expected based on the velocity production of the device (~1 m/s) and the maximum speed of the facility (~12m/s)

Ns-DBD plasma actuators were applied to the mixing layer to investigate the mechanisms associated with their efficacy (and thermal perturbations in general) for controlling turbulent shear flows. Despite numerous attempts, no clear excitation of the turbulent mixing layer was observed for this seemingly high amplitude actuation technique. These observations, along with further consideration of the literature, suggest the initial thickness of the turbulent shear layer is a strong driver for establishing possible control authority with thermal perturbations. Boundary layer suction was employed in an attempt to reduce the relatively large initial shear layer thickness ($\theta_o \approx 1$ mm) to a level more commensurate with successful demonstrations in the literature ($\theta_o \approx 0.1$ mm). Some limited evidence for control authority was observed with suction, but did not clearly exceed the measurement uncertainty presumably because the initial shear layer was still somewhat thick ($\theta_o > 0.1$ mm). This motivated a transition to the study of turbulent shear layers downstream of a backward-facing step with focus on the region well-upstream of flow reattachment.

A small blow-down wind tunnel was designed and constructed to produce a relatively thin turbulent initial shear layer downstream of a backward facing step. The freestream velocity, wind tunnel contraction ratio and short boundary layer development length resulted in an initial momentum thickness of $\theta_o \approx 0.15$mm along with a well-developed inertial subrange over nearly two decades of frequency. Thermal disturbances from ns-DBD plasma actuators located at the step corner resulted in control authority using relatively low amplitude pulses (0.33 mJ/cm/pulse). Effective actuation frequencies were in the range expected from literature ($0.005 < St_\theta < 0.015$) and this was reinforced by hot wire measurements of the baseline shear layer showing a broad peak in this region of the spectrum. This relatively simple experiment confirmed the efficacy of thermal disturbances for controlling turbulent shear layers in zero pressure gradient and reinforced our hypothesis on the importance of initial shear layer thickness. Increasing pulse energy while holding frequency constant resulted in a saturation and eventual degradation in control authority. This may be attributed to non-uniformities in the discharge at high energy (i.e. non-uniform spanwise heating), but it was not obvious from digital photographs or schlieren imaging. A more interesting scientific possibility is that too much heat addition could produce a stabilizing effect and this has been observed in reacting shear

52

layers with heat release in the downstream mixing region. However, in the ns-DBD plasma case, heat addition is added at the mixing layer origin which necessitates further study. The possible competition between thermal mechanisms (excitation vs. stabilization) should be explored as it could offer even greater possibilities for control that would have fundamental and practical relevance. Preliminary results on the use of femtosecond laser pulses for AFC showed similar trends as the ns-DBD plasma actuator supporting this notion. It would be very useful to further investigate possibilities for forcing off-body using laser filament technology. It should be noted that similar trends (excitation and stabilization) were reported in the ns-DBD mixing layer case, but bordered on the measurement uncertainty.

The BFS control authority at relatively low pulse energy re-affirmed our belief that the required energy deposition should scale with some measure of the local shear layer thickness. With this in mind, we returned to the mixing layer facility armed with a pulsed Nd:YAG laser as well as a higher energy and frequency pulse generator. The laser was formed into a sheet and fired onto the splitter plate trailing edge to approximate the disturbance produced by a strong ns-DBD pulse. Based on benchtop characterization, the laser disturbance approximated that of an ns-DBD plasma actuator operating at 6 mJ/cm/pulse which is beyond our current power supply capability. Regardless, it gave some insight into possible scaling arguments as the localized hot spot produced by laser ablation has a radius on the same order of magnitude as the initial mixing layer momentum thickness. The laser was limited to 10 Hz (or St≈0.01 at the test section extent), but excited the mixing layer resulting in downstream growth and a frequency spectrum consisting of the fundamental frequency and higher harmonics indicating an impulse-like response. A new pulse generator operating at St=0.03 increased the available pulse energy to 2.5 mJ/cm, but did not produce mixing layer control authority. This was not totally unexpected given benchtop characterization and Nd:YAG laser results. However, burst modulation at St=0.03 with high burst frequency (9kHz) finally resulted in the expected mixing layer control authority. In this case, the structure of the controlled flow was void of the impulse-like behavior from laser energy deposition. Thus, it appears some convective behavior may be playing a role similar to that observed by Correale et al. (2014b). Both the Nd:YAG laser and higher energy/frequency pulser results were acquired *after* the end of the award period and their analysis/interpretation is ongoing. However, it is now clear that the turbulent mixing layer in question can be excited by strong single frequency thermal disturbances (e.g. Nd:YAG laser) as well as collective heating from many lower energy disturbances in burst mode (e.g. ns-DBD). The latter also suggests the localized compression wave is not a mechanism for flow control at these conditions. It should also be noted that substantial momentum production from ns-DBDs near the splitter plate trailing edge has not been observed ruling out this mechanism as expected. A formal publication of these results is in preparation.

In summary, the following conclusions regarding thermal mechanisms for control of low-speed turbulent shear layers are offered.

1. A localized thermal effect (density or viscosity perturbation) provides the control mechanism. The compression wave and weak momentum addition do not play a significant role.

2. The required energy deposition is related to an as yet to be determined measure of the initial shear layer thickness.

3. High levels of energy deposition may result in stabilization of the flow suggesting a competing mechanism is at play.

4. Energy deposition can be employed as single frequency forcing or alternatively using a collective heating from many pulses in burst operation.

5. The flow response can resemble an impulse-like behavior (high energy single frequency) or a more standard convective behavior (high frequency burst at lower pulse energy).

6. The initial shear layer state (laminar/turbulent) does not determine possible control authority. However, laminar flows likely require weaker thermal disturbances for excitation.

7. The thermal effect is very local and actuator location must be chosen wisely to ensure control authority.

8. Freestream velocity is of secondary importance to initial shear layer thickness in the range surveyed.

9. Thermal perturbations are best suited for the control of thin shear layers and well-defined geometries.

10. Laser energy deposition (both on and off-body) is a useful model for offering further understanding of thermal mechanisms for aerodynamic flow control.

VIII.   Future Work

Our research indicates that future work along the following lines is required. A follow-up proposal is forthcoming.

- The role of density vs. viscosity perturbation should be established through collaboration with computational and theoretical studies.
- An amplitude coefficient analogous to the widely employed C_μ for momentum-based actuators should be pursued through systematic variation of the initial shear layer thickness and energy deposition.
- The competing mechanisms (excitation vs. stabilization) should be explored with consideration of previous research in water and reacting gas flows with heat release.
- The capability of energy deposition for generating an impulse response across a variety of turbulent shear flows may yield promising insight for fundamental studies as well as modelling and control efforts.
- The possibility of off-body pulsed energy deposition (e.g. fs laser filaments) should be explored in a collaborative experimental/computational/theoretical fashion.

IX.   Publications and Students

To date, the research project supported 1 conference abstract, 6 conference papers and 1 journal article along with 3 M.S. theses. One additional conference paper and two additional journal articles are in preparation. A list of the current publications is provided below.

Conference Abstracts
1. R. Ely and J. Little, "Mixing Layer Excitation by Dielectric Barrier Discharge Plasma Actuators," 65th American Physical Society, Division of Fluid Dynamics Meeting, San Diego, CA, November 18, 2012; *Bulletin of the American Physical Society*, Vol. 57, No. 17.

Conference Papers
1. R. Ely and J. Little, "Mixing Layer Excitation by Dielectric Barrier Discharge Plasma Actuators," AIAA 2013-1012, AIAA Aerospace Sciences Meeting 2013.
2. R. Ely and J. Little, "The mixing layer perturbed by a dielectric barrier discharge," AIAA 2013-2753, AIAA Fluid Dynamics Conference 2013.
3. R. Lehmann, D. Akins, and J. Little, "Effects of Ns-DBD Plasma Actuators on Turbulent Shear Layers," AIAA 2014-2220, AIAA Flow Control Conference 2014.
4. D. Akins, A. Singh, and J. Little, "Effects of Pulse Energy on Shear Layer Control Using Pulse Plasma Discharges," AIAA 2015-3344, AIAA Aerospace Sciences Meeting 2015.
5. J. Little and U. Kaul, "Mixing Layer: Numerical and Experimental Control Strategies," AIAA 2015-3343, AIAA Aerospace Sciences Meeting 2015.
6. J. Chabot, E. Caraballo, and J. Little, "Reduced Order Modeling of a Dielectric Barrier Discharge Controlled Mixing Layer Using Minimum Basis Rotations," AIAA 2015-2940, AIAA Aerospace Sciences Meeting 2015.
7. Singh, A. and Little, J., "Active Control of a Turbulent Mixing Layer using Pulsed Laser and Pulsed Plasma," AIAA 2016-0455, AIAA SciTech 2016.

Journal Articles
1. R. Lehmann, D. Akins, and J. Little, "Effects of Ns-DBD Plasma Actuators on Turbulent Shear Layers," *AIAA Journal* (accepted June 2015).

MS Theses
1. Ely, R., "Response of a Low-speed Incompressible Turbulent Mixing Layer to Perturbations form Dielectric Barrier Discharge Plasma Actuation," MS Thesis, Aerospace and Mechanical Engineering, University of Arizona, 2013.
2. Lehmann, R., "Effects of Ns-DBD Plasma Actuators on Turbulent Shear Layers," MS Thesis, TU Berlin, 2014.
3. Akins, D., "Control of the Turbulent Shear Layer Downstream of a Backward Facing Step using Nanosecond Pulse Driven Surface Plasma Discharges: Effects of Pulse Energy," MS Thesis, Aerospace and Mechanical Engineering, University of Arizona, 2015.

X.   Acknowledgements

XI.   References

Adelgren R, Elliott G, Crawford J, Carter C, Donbaar J, Grosjean D (2005) Axisymmetric Jet Shear-Layer Excitation by Laser Energy and Electric Arc Discharge. AIAA Journal 43[4]:776-791

Aradag S, Yan H, Knight D (2004) Energy Deposition in Supersonic Cavity Flow. AIAA Paper 2004-0514

Ashcraft T, Decker K, Little J (2016) Control of Boundary Layer Separation and the Wake of an Airfoil using ns-DBD Plasma Actuators. AIAA Paper 2016-0839

Benard N, Sujar-Garrido P, Bayoda K, Bonnet J, Moreau E (2014) Pulsed dielectric barrier discharge for manipulation of turbulent flow downstream a backward-facing-step. AIAA Paper 2014-1127

Birch S, Eggers J (1972) A Critical Review of the Experimental Data for Developed Free Turbulent Shear Layers. Volume 1 - Conference Proceedings NASA SP-321

Brassard D, Ferchichi M (2005) Transformation of a Polynomial for a Contraction Wall Profile. Journal of Fluids Engineering 127[1]:183-185 DOI 10.1115/1.1852492

Cattafesta L, Sheplak M (2011) Actuators for Active Flow Control. Annual Review of Fluid Mechanics 43:247-272

Cattafesta L, Song Q, Williams D, Rowley C, Alvi F (2008) Active Control of Flow-Induced Cavity Oscillations. Progress in Aerospace Sciences 44:479-502

Chandrsuda C, Bradshaw P (1981) Turbulence structure of a reattaching mixing layer. Journal of Fluid Mechanics 110:171-194

Chun K, Sung H (1996) Control of Turbulent Separated Flow over a Backward-facing Step by Local Forcing. Experiments in Fluids 21:417-426

Corke TC, Enloe C, Wilkinson SP (2010) Dielectric Barrier Discharge Plasma Actuators for Flow Control. Annual Review of Fluid Mechanics 42:505-529

Correale G, Michelis T, Kotsonis M (2014a) NS-DBD plasma actuation on a backward facing step. AIAA paper 2014-0325

Correale G, Michelis T, Ragni D, Kotsonis M, Scarano F (2014b) Nanosecond-pulsed plasma actuation in quiescent air and laminar boundary layer. Journal of Physics D: Applied Physics 47[10]:105201

Dawson R, Little J (2013) Characterization of nanosecond pulse driven dielectric barrier discharge plasma actuators for aerodynamic flow control. Journal of Applied Physics 113[10]:103302-103310

Dawson RA, Little J (2014) Effects of pulse polarity on nanosecond pulse driven dielectric barrier discharge plasma actuators. Journal of Applied Physics 115[4]:043306 DOI doi:http://dx.doi.org/10.1063/1.4863175

DeBlauw B, Elliott G, Dutton C (2014) Active Control of Supersonic Base Flows with Electric Arc Plasma Actuators. AIAA Journal 52[7]:1502-1517 DOI 10.2514/1.j052585

Driver D, Seegmiller H, Marvin J (1987) Time-Dependent Behavior of a Reattaching Shear Layer. AIAA Journal 25[7]

Eaton JK, Johnston JP (1981) A Review of Research on Subsonic Turbulent Flow Reattachment. AIAA Journal 19[9]:1093-1100 DOI 10.2514/3.60048

Ely R, Little J (2013a) Mixing Layer Excitation by Dielectric Barrier Discharge Plasma Actuators. AIAA Paper 2013-1012

Ely R, Little J (2013b) The Mixing Layer Perturbed by Dielectric Barrier Discharge. AIAA Paper 2013-2753

Enloe C, McLaughlin T, VanDyken R, Kachner K, Jumper E, Corke T, Post M, Haddad O (2004) Mechanisms and Responses of a Single Dielectric Barrier Plasma Actuator: Geometric Effects. AIAA Journal 42[3]:595-604

Fiedler H, Fernholz H (1990) On Management and Control of Turbulent Shear Flows. Progress in Aerospace Sciences 27[4]:305-387

Gaitonde D, Sahin M, Shaler K, Glaz B, Dinavahi S (2013) High-Fidelity Simulations of NS-DBD-based Control of a Stalled NACA 0015 Airfoil. AIAA Paper 2013-1118

Gaitonde D, Samimy M (2011) Coherent structures in plasma-actuator controlled supersonic jets: Axisymmetric and mixed azimuthal modes. Physics of Fluids 23[095104]

Gaitonde DV (2012) Analysis of the Near Field in a Plasma-Actuator-Controlled Supersonic Jet. Journal of Propulsion and Power 28[2]:281-292 DOI 10.2514/1.57742

Gibalov VI, Pietsch GJ (2000) The development of dielectric barrier discharges in gas gaps and on surfaces. Journal of Physics D-Applied Physics 33[20]:2618-2636 DOI Doi 10.1088/0022-3727/33/20/315

Greenblatt D, Wygnanski I (2000) The Control of Flow Separation by Periodic Excitation. Progress in Aerospace Sciences 36:487-545

Hasan MAZ (1992) The flow over a backward-facing step under controlled perturbation: laminar separation. Journal of Fluid Mechanics 238:73-96

Hermanson JC, Dimotakis PE (1989) Effects of Heat Release in a Turbulent, Reacting Shear Layer. Journal of Fluid Mechanics 199:333-375

Hermanson JC, Mungal MG, Dimotakis PE (1987) Heat Release Effects on Shear-Layer Growth and Entrainment. AIAA Journal 25[4]:578-583

Ho C-M, Huerre P (1984) Perturbed free shear layers. Annual Review of Fluid Mechanics 16:365-424

Huerre P, Monkewitz P (1985) Absolute and Convective Instabilities in Free Shear Layers. Journal of Fluid Mechanics 159:151-168

Jukes TN, Choi K-S, Johnson GA, Scott SJ (2006) Characterization of Surface Plasma-Induced Wall Flows Through Velocity and Temperature Measurements. AIAA Journal 44[4]:764-771

Kapiris PG, Mathioulakis DS (2014) Experimental study of vortical structures in a periodically perturbed flow over a backward-facing step. International Journal of Heat and Fluid Flow 47[0]:101-112 DOI http://dx.doi.org/10.1016/j.ijheatfluidflow.2014.03.004

Kearney-Fischer M, Kim J-H, Samimy M (2009) Control of a high Reynolds number Mach 0.9 heated jet using plasma actuators. Physics of Fluids 21:095101

Lazar E, Elliot G, Glumac N (2008) Control of the Shear Layer Above a Supersonic Cavity Using Energy Deposition. AIAA Journal 46[12]:2987-2997

Likhanskii A, Shneider M, Macheret S, Miles R (2008) Modeling of Dielectric Barrier Discharge Plasma Actuator in Air. Journal of Applied Physics 103[053305]:1-13

Little J (2010) High-Lift Airfoil Separation Control with Dielectric Barrier Discharge Plasma Actuators. Dissertation, The Ohio State University

Little J, Samimy M (2010) High-Lift Airfoil Separation Control with Dielectric Barrier Discharge Plasma Actuation. AIAA Journal 48[12]:2884-2898

Little J, Takashima K, Nishihara M, Adamovich I, Samimy M (2012) Separation Control with Nanosecond-Pulse-Driven Dielectric Barrier Discharge Plasma Actuators. AIAA Journal 50[2]:350-365

McMurtry P, Jou W, Riley J, Metcalfe R (1986) Direct Numerical Simulations of a Reacting Mixing Layer with Chemical Heat Release. AIAA Journal 24[6]:962-970

Mehta R, Bradshaw P (1979) Design Rules for Small Low Speed Wind Tunnels. The Aeronautical Journal of the Royal Aeronautical Society 718:8

Michalke A (1965) On Spatially Growing Disturbances in an Inviscid Shear Layer. Journal of Fluid Mechanics 23[3]:521-544

Michelis T, Correale G, Popov IB, Kotsonis M, Ragni D, Hulshoff SJ, Veldhuis LLM (2013) Disturbance introduced into a laminar Bounday Layer by a NS-DBD plasma actuator. AIAA Paper 2013-0752

Opaits D, Likhanskii A, Neretti G, Zaidi S, Shneider M, Miles R, Macheret S (2008) Experimental Investigation of Dielectric Barrier Discharge Plasma Actuators driven by Repetitive High-Voltage Nanosecond Pulses with DC or Low Frequency Sinusoidal Bias. Journal of Applied Physics 104[043304]:1-15

Oster D, Wygnanski I (1982) The forced mixing layer between parallel streams. Journal of Fluid Mechanics 123:91-130

Rethmel C, Little J, Takashima K, Sinha A, Adamovich I, Samimy M (2011) Flow Separation Control using Nanosecond Pulse Driven DBD Plasma Actuators. International Journal of Flow Control 3[4]:213-232

Reynolds WC, Parekh DE, Juvet PJD, Lee MJD (2003) Bifurcating and Blooming Jets. Annual Review of Fluid Mechanics 35:295-315

Roupassov D, Nikipelov A, Nudnova M, Starikovskii A (2009) Flow Separation Control by Plasma Actuator with Nanosecond Pulsed-Periodic Discharge. AIAA Journal 47[1]:168-185

Samimy M, Kim J, Kearney-Fischer M, Sinha A (2010) Acoustic and Flow Fields of an Excited High Reynolds Number Axisymmetric Supersonic Jet. Journal of Fluid Mechanics 656:507-529

Samimy M, Kim JH, Kastner J, Adamovich I, Utkin Y (2007) Active Control of High-Speed and High-Reynolds-Number Jets Using Plasma Actuators. Journal of Fluid Mechanics 578:305-330

Seifert A, Tilmann C (2009) Fixed Wing Airfoil Applications. In: Fundamentals and Applications of Modern Flow Control. eds Joslin, R and Miller, D). Vol. 231, pp. 231-257, Reston, VA: AIAA

Simpson RL (1989) Turbulent Boundary Layer Separation. Annual Review of Fluid Mechanics 21:205-234

Singh A, Little J (2016) Active Control of a Turbulent Mixing Layer using Pulsed Laser and Pulsed Plasma. AIAA Paper 2016-0455

Sung Y, Kim W, Mungal M, Cappelli M (2006) Aerodynamic Modification of Flow over Bluff Objects by Plasma Actuation. Experiments in Fluids Vol. 41:479-486

Takashima K, Zuzeek Y, Lempert W, Adamovich I (2011) Characterization of a Surface Dielectric Barrier Discharge Plasma Sustained by Repetitive Nanosecond Pulses. Plasma Sources Science and Technology 20[055009]

Unfer T, Boeuf J (2009) Modelling of a Nanosecond Surface Discharge Actuator. Journal of Physics D: Applied Physics 42[194017]:12

Vukasinovic B, Rusak Z, Glezer A (2010) Dissipative Small-Scale Actuation of a Turbulent Shear Layer. Journal of Fluid Mechanics 656:51-81

Wee D, Yi T, Annaswamy A, Ghoniem AF (2004) Self-sustained oscillations and vortex shedding in backward-facing step flows: Simulation and linear instability analysis. Physics of Fluids (1994-present) 16[9]:3361-3373 DOI doi:http://dx.doi.org/10.1063/1.1773091

Weisbrot I, Wygnanski I (1988) On Coherent Structures in a Highly Excited Mixing Layer. Journal of Fluid Mechanics 195:137-159

Whalen E, Lacy D, Lin J, Andino M, Washburn A, Graff E, Wygnanski I (2015) Performance Enhancement of a Full-Scale Vertical Tail Model Equipped with Active Flow Control. AIAA Paper 2015-0784

Wygnanski IJ, Petersen RA (1987) Coherent motion in excited free shear flows. AIAA Journal 25[2]:201-213 DOI 10.2514/3.9610

1.

1. Report Type

Final Report

Primary Contact E-mail
Contact email if there is a problem with the report.

jesselittle@email.arizona.edu

Primary Contact Phone Number
Contact phone number if there is a problem with the report

5206268677

Organization / Institution name

University of Arizona

Grant/Contract Title
The full title of the funded effort.

(YIP 12)-Thermal Mechanisms for High Amplitude Aerodynamic Flow Control

Grant/Contract Number
AFOSR assigned control number. It must begin with "FA9550" or "F49620" or "FA2386".

FA9550-12-1-0044

Principal Investigator Name
The full name of the principal investigator on the grant or contract.

Jesse Little

Program Manager
The AFOSR Program Manager currently assigned to the award

Ivett Leyva (previously Douglas Smith)

Reporting Period Start Date

05/01/2012

Reporting Period End Date

04/30/2015

Abstract

The potential of thermal perturbations (i.e. energy deposition) and subsequent compression wave generation as a mechanism for high amplitude, high bandwidth actuation has been demonstrated, but the fundamental physics of how this influences the flow field remain poorly understood. There is a vital difference in the flow receptivity to these perturbations in comparison to more traditional zero net mass flux momentum-based devices. The aim of this study is to establish knowledge of the fundamental mechanisms underpinning the success of energy deposition for active flow control. This report summarizes efforts over a three year period under the AFOSR Young Investigator Program which seek to first study the phenomena at low speeds. The basic nature of this problem requires examination of a canonical flow system and turbulent shear layers are employed due to their ubiquitous nature in active flow control. The effects of localized thermal perturbations, delivered by electrical discharges and pulsed lasers, on these flows are studied experimentally with strong consideration of the rapidly developing literature and established theory. Our most important finding is that the required energy deposition is related to an as yet to be determined measure of the initial shear layer thickness. The initial shear layer state and freestream velocity are of secondary importance in the flow regimes surveyed. This suggests that amplitude scaling ideas for thermal perturbations are fundamentally different from those accepted for momentum-based devices. It also provides guidance for moving forward with such a definition. This definition has not yet been established,

but is a primary focus of suggested future work. The thermal disturbances may be provided by single frequency forcing or alternatively using a collective heating from many pulses in burst operation. The response of the controlled flow can resemble an impulse-like behavior (high energy single frequency forcing) or a more standard convective nature (high frequency burst at lower pulse energies). These differing responses offer new avenues for exploration. In both cases, high levels of energy deposition can result in stabilization of the flow suggesting a competing mechanism is at play. Such a scenario has been observed in reacting flows with heat release, but has received no attention with respect to active flow control. In summary, the foundations of thermal mechanisms for active flow control have been established at low speeds. Future efforts now require progression to higher speeds flows with thinner turbulent shear layers.

Distribution Statement

This is block 12 on the SF298 form.

Distribution A - Approved for Public Release

Explanation for Distribution Statement

If this is not approved for public release, please provide a short explanation. E.g., contains proprietary information.

SF298 Form

Please attach your SF298 form. A blank SF298 can be found here. Please do not password protect or secure the PDF The maximum file size for an SF298 is 50MB.

SF298-Final Report.pdf

Upload the Report Document. File must be a PDF. Please do not password protect or secure the PDF . The maximum file size for the Report Document is 50MB.

Little_AFOSR_Final_Report.pdf

Upload a Report Document, if any. The maximum file size for the Report Document is 50MB.

Archival Publications (published) during reporting period:

R. Lehmann, D. Akins, and J. Little, "Effects of Ns-DBD Plasma Actuators on Turbulent Shear Layers," AIAA Journal (published online in December 2015.

Changes in research objectives (if any):

None

Change in AFOSR Program Manager, if any:

Original PM Douglas Smith moved on after the end of award period. Acting PM Ivett Leyva will receive the Final Report.

Extensions granted or milestones slipped, if any:

An NCE was not requested, but I should have done so. The Final Report is substantially delayed due in large part to a student health issue.

AFOSR LRIR Number

LRIR Title

Reporting Period

Laboratory Task Manager

Program Officer

Research Objectives

Technical Summary

Funding Summary by Cost Category (by FY, $K)

	Starting FY	FY+1	FY+2
Salary			
Equipment/Facilities			
Supplies			
Total			

Report Document

Report Document - Text Analysis

Report Document - Text Analysis

Appendix Documents

2. Thank You

E-mail user

Apr 14, 2016 15:02:51 Success: Email Sent to: jesselittle@email.arizona.edu